

ABSTRACT

Title of dissertation: PHONON MODELING IN NANO- AND MICRO- SCALE CRYSTALLINE SYSTEM

Francis G. VanGessel
Doctor of Philosophy, 2018

Dissertation directed by: Professor Peter W. Chung
Department of Mechanical Engineering

Submicrometer phonon systems are becoming increasingly relevant in modern day technology. Phonon mechanisms are notably relevant in a number of solid-state devices including lasers, LEDs, transistors, and thermoelectrics. Proliferation of these devices has been driven by advancements in silicon-on-insulator technology. These advancements have allowed for the manufacture of devices with complex nanostructures and dimensions deep in the sub-microscale regime. However, accompanying improvements in the manufacture and design of novel crystalline systems is the requirement for accurate computational approaches for phonon modeling in nanostructured, anisotropic, and complex materials. The phonon Boltzmann transport equation is uniquely well suited to modeling energy transfer at the nano- and micro- meter length scales and is therefore an excellent candidate for this simulation task. However, current Boltzmann modeling approaches utilize a range of assumptions and simplifications that restrict their validity to isotropic, nominally one or two dimensional, or compositionally simple systems.

In this dissertation we present an original finite volume-based methodology for the solution of the three dimensional full Brillouin zone phonon Boltzmann transport equation. This methodology allows for separate real and reciprocal space discretization. By taking a sampling of vibrational modes throughout the first Brillouin zone our methodology captures three unique sources of phonon anisotropy. We investigate the effect of phonon anisotropy in a fin field effect transistor, calculating the effect that incorporating various sources of anisotropy has on the resultant temperature fields.

In a second study, we consider phonon flow through silicon nanowires with a modified boundary geometry. The three-dimensional flow fields are calculated and thermal transport *below* the Casimir limit is observed. Reduction in thermal conductivity is a result of maximizing the phonon backscatter that occurs in our phononic system. The backscatter serves to create regions of highly misaligned

phonon flux. In addition, our silicon nanowire geometry has properties analogous with a high-pass phonon filter.

In the final study we apply our Boltzmann transport methodology to the simulation of phonon transport in the energetic material, RDX. We study phonon transport in the vicinity of a material hotspot, the location at which chemistry initiates in the material. By applying Boltzmann modeling, applied for the first time to this material, we gain valuable insights into the interplay between thermal transport and phonon modes linked with initiation.

PHONON MODELING IN NANO- AND
MICRO- SCALE CRYSTALLINE SYSTEMS

by

Francis G. VanGessel

Dissertation submitted to the Faculty of the Graduate School of the
University of Maryland, College Park in partial fulfillment
of the requirements for the degree of
Doctor of Philosophy
2018

Advisory Committee:

Professor Peter W. Chung, Chair/Advisor

Professor Neil Goldsman, Dean's Representative

Professor Bao Yang

Professor Abhijit Dasgupta

Professor Yifei Mo

© Copyright by
Francis G. VanGessel
2018

Acknowledgments

The path to attaining my Ph.D. has been long, difficult, and incredibly rewarding. This accomplishment is one that I could not have achieved without the support of a network of friends, family, and mentors. Here I would like to thank a few select individuals who were instrumental in my success.

First, my advisor Dr. Peter Chung has been an incredible mentor, helping me grow and mature as a researcher. Leading by example, he has inspired and challenged me to continually improve myself and I leave University of Maryland feeling confident in my skills and abilities. His availability and willingness to discuss theoretical questions, provide feedback on manuscripts, suggest research directions, and critique presentations has been an amazing resource during my time as a graduate student. Simply put I could not have asked for a better advisor.

In addition, I found the Mechanical Engineering Department a wonderful place to grow and learn as an engineer. The faculty are generous with their time, both in answering questions and providing helpful feedback as committee members. In addition my lab mates Jie, Gaurav, Rose, and Eunjeong were excellent partners for discussing concepts, as well as commiserating about the difficulties of life as a graduate student. I am glad I chose the University of Maryland and am grateful for the friendships I made with such wonderful people.

My family has been an incredible source of support and love over these past five years. I cannot express how amazing my parents, Mark and Kate, have been in providing me with everything I needed to succeed. They instilled in me the

importance of higher education as well as made it clear that whatever path I chose they would support me wholeheartedly (although, as two professors themselves, I am sure they are happy I chose the Ph.D. route even if the exact area was slightly off). Carl, Claudia, and Gladis are equally amazing and supportive, spending time with them always seemed to remove the stress associated with finishing my Ph.D. Last, Laura Leigh Cooper has been incredible in her encouragement and support over these past five years and I am lucky to have her in my life. All of you are amazing and I love you all!

Furthermore, I gratefully acknowledge the funding provided through the graduate fellowship from the Center for Engineering Concepts Development. In addition, portions of this work were also supported, in part, by the Army Research Office under Award W911NF-14-1-0330. Finally, the Army Research Laboratory generously provided me space during the development of the finite volume BTE code.

Table of Contents

Dedication	ii
Acknowledgements	ii
List of Abbreviations	xii
1 Introduction	1
1.1 Challenges Associated with Phonon Modeling	3
1.2 Research Outline	7
2 Phonon Theory and Simulation	11
2.1 Phonon Theory	12
2.1.1 1D System	12
2.1.2 Real Materials	22
2.1.3 Phonon Scattering	25
2.2 Phonon Boltzmann Transport Modeling	28
2.2.1 Phonon Boltzmann Transport Equation	28
2.2.2 Numerical Methods	32
3 Methodology for Solution of Full Brillouin Zone Three Dimensional Phonon BTE	45
3.1 History of BTE Methodology Developments	46
3.2 Problem Definition	51
3.2.1 Material Domain	51
3.2.2 Born von-Karman Boundary Conditions	53
3.2.3 Phonon Boltzmann Transport Equation	56
3.3 Methodology	58
3.3.1 Discretization	60
3.3.2 Specific Heat	64
3.3.3 Boundary Conditions	66
3.3.4 Determination of Phonon Properties	71
3.4 Verification	77
4 Effect of Phonon Anisotropy in FinFET Device	86
4.1 FinFET Device Simulation	87

4.2	Conclusion	103
5	Phonon backscatter, trapping, and misalignment effects on microscale thermal conductance below the Casimir limit	104
5.1	Controlling Phonons in Nano- and Micro- structures	106
5.2	Methodology	110
5.2.1	Model Geometry	110
5.2.2	Modeling Approach	113
5.3	Results & Discussion	117
5.3.1	Backscatter in smooth NW: limiting case 1	117
5.3.2	Backscatter in smooth and rough NW: limiting case 2	119
5.3.3	Smooth vs. rough NW: flux misalignment	128
5.3.4	Finite length nanodevice	131
5.3.5	Verification of NW Simulations	135
5.4	Conclusion	136
6	A Phonon Boltzmann Study of Microscale Thermal Transport in α-RDX Cook-Off	138
6.1	Phonons in Energetic Materials	139
6.2	Methods	141
6.2.1	α RDX Thermal Properties	142
6.2.2	Full Band Phonon Relaxation Times	143
6.2.3	Phonon Boltzmann Transport Modeling in α RDX	146
6.2.4	N-N Bond Stretch Metric	148
6.3	Results	149
6.3.1	Full Brillouin Zone Analysis of RDX	149
6.3.2	Full-Band Relaxation Times of RDX	154
6.3.3	Phonon BTE Simulation of RDX Hotspot	158
6.3.4	Verification of Hotspot Simulation	163
6.4	Conclusion	164
7	Conclusion	166
7.1	Summary and Contributions	167
7.2	Future Research Directions	172
	Bibliography	176

List of Tables

2.1	Comparison of the three types of phonon BTE numerical solution techniques, each of which emphasizes a certain component of the BTE model: real space, reciprocal space, or scattering. The primary differences between these types are the complexity of the spatial domains to which they are applied, how they represent the Brillouin zone (isotropic, anisotropic, or explicit calculation of mode to mode coupling), and how phonon-phonon scattering is modeled.	33
3.1	Gray phonon properties	79
4.1	Interatomic potential constants	90
4.2	Functional form of the phonon scattering rates from [1] for both Umklapp, τ_U^{-1} , and normal, τ_N^{-1} , scattering rates.	90
4.3	Parameter values for phonon scattering rates in Table 4.2 given by [1]	90
4.4	Maximum temperature rise in each simulation over 300K.	97
4.5	Average phonon properties used in the IBZ BTE simulation of the FinFET.	99
4.6	Radiosity of IBZ, FBZ, and FBZ τ along the principal direction, all values are in units of 10^{11} W/m ²	102
5.1	Ray-tracing statistics for phonon flux reduction, MFP and, backscattering in infinite chamber-offset NW.	119
6.1	Percent of energy residing in large stretching modes, δ	160
6.2	Percentage of flux transported by acoustic and optical modes along principal directions.	161

List of Figures

Chapter 1

- 1.1 Length scales of applicability of the LD, MD, BTE, and DFT methods. In this figure λ represents the phonon wavelength while Λ represents the phonon mean free path. 2
- 1.2 Examples of microscale systems that may be regarded as (a) one, (b) two, or (c) three dimensional. Cross-plane heat transport in a thin film (a) is a nominally one dimensional system. Heat flow in a planar MOSFET (b) can be modeled as a two dimensional system. Current generation transistors such as a FinFET (c) have thermal profiles which vary in all three dimensions. 5
- 1.3 Comparison of a full Brillouin zone representation (a) versus the simplified isotropic dispersion representation (b). The constant frequency contours of the $k_z = 0$ plane in the isotropic Brillouin zone are circular sections. The gray approximation is not shown as it collapses the BZ to point where dispersion has no meaning, i.e. ω is a constant independent of wavevector \mathbf{k} 7

- 2.1 A 1D crystalline system consisting of atoms of mass m . Each mass is connected to its nearest neighbor via a linear spring. The spacing between nearest neighbors is a . The outline of the unit cell of the crystal is indicated by the dashed line. 12

Chapter 2

- 2.2 Plots of a six atom section, along with corresponding mode shapes, of the one-dimensional crystalline system. The continuous curves corresponding to $u(x, k) = C_0 e^{ikx}$ for $k = \pi/10a$ and $k = \pi/10a + 2\pi n/a$ ($n = 1, 2, 3, 4$) are shown in blue and red respectively. At the points r_l^0 (filled black circles) the displacements corresponding to $k = \pi/10a$ and $k = \pi/10a + 2\pi n/a$ (open black circles) are identical and therefore the atomic motion corresponding to the wavevectors outside the Brillouin zone is indistinguishable from wavevector, k , within the Brillouin zone. 15
- 2.3 Phonon frequencies for 1D chain. The black dots correspond to the phonon modes visualized in Fig. 2.4 16

2.4	Phonon mode shapes for 5 different wavevectors. The equilibrium positions of the atoms are denoted by open red circles. The displacements of the atoms from equilibrium are indicated by blue arrows. The black lines are a visual aid to make the sinusoidal shape of the phonon mode more apparent.	17
2.5	Phonon group velocities for 1D chain.	18
2.6	The specific heat as a function of wavevector at three distinct temperature regimes.	20
2.7	The thermal conductivity as a function of wavevector at three distinct temperature regimes.	21
2.8	Dispersion surfaces of the first three branches (TA, TO, LA) of silicon in the $k_z = 0$ plane. The projected constant frequency contours indicate microscale dispersion anisotropy. The blue lines form an outline of the irreducible wedge of the first Brillouin zone.	24

Chapter 2

Chapter 3

3.1	The three types (finite lattice, microscale, and macroscopic) of phonon anisotropy. Associated with each type of anisotropy is the source, characteristic system length scale, as well as quantifying metric. The source of the phonon anisotropy indicates the underlying cause. The characteristic system length scale indicates the system dimensions for which the anisotropy produces non-negligible effects on phonon flow. The quantifying metric indicates the method for quantifying the degree, and directionality, of the anisotropy (either thermal conductivity, κ , calculated via the phonon gas model as defined in eq. 6.1, or phonon radiosity defined in eq. 4.3).	48
3.2	Problem domain Ω with boundary Γ	51
3.3	A crystal lattice with lattice points as blue dots, primitive lattice vectors $\{\mathbf{a}_1, \mathbf{a}_2, \mathbf{a}_3\}$, and three-atom basis $\{\mathbf{b}_1, \mathbf{b}_2, \mathbf{b}_3\}$	52
3.4	The BTE is solved for the complete set of phonon modes $(\dots, \gamma, \kappa, \tau, \mu, \dots)$ as determined by Born von-Karman boundary conditions. The domain on which each mode resides is discretized and solved on copies of the same spatial grid. The advection properties of each mode are determined from the group velocity (red arrows). The coupling between phonon modes occurs through the RTA which models phonon-phonon scattering by relaxing each mode to an equilibrium thermal bath corresponding to the total system energy (red rectangle). Energy is transferred to and from each mode when the mode deviates from the equilibrium Bose-Einstein statistical distribution. The coupling strength of each mode to the thermal bath is determined by the mode relaxation time τ	59

3.5	Domain Ω discretized into control volumes. A single control volume, Ω_i , is depicted along with a surface facet, $\partial\Omega_{i,f}$, and the associated normal vector, $\hat{\mathbf{n}}_{i,f}$. Additionally the boundary control area that Ω_i intersects, Γ_l , is shown along with the associated normal vector $\hat{\mathbf{n}}_l$. . .	61
3.6	Phonon wavepacket undergoing specular reflection	67
3.7	Phonon wavepacket undergoing diffuse reflection in an idealized material with radially symmetric dispersion surfaces.	69
Chapter 3		
3.8	Temperature profile (thick dashed line) of a slab geometry composed of material with gray phonon properties. The Fourier boundary conditions at the boundaries are given by the temperatures T_1 (red) and T_2 (blue).	80
3.9	Spherical Brillouin Zones of (a) 102 kpoints (b) 236 kpoints (c) 408 kpoints (d) 824 kpoints (e) 1444 kpoints (f) 2208 kpoints (g) 9092 kpoints (h) 49426 kpoints. Kpoints are placed on the surface of a sphere so that their distribution is as uniform as possible.	81
3.10	Point wise error in the temperature results for numerical experiment of 1D slabs with varying thickness.	83
3.11	RMS error vs. number of kpoints in Brillouin zone for varying slab thickness.	84
3.12	Root mean square (RMS) error between the Boltzmann method and the exact numerical solution from Eq. 3.45 for variable grid sizes. Slab thickness is $\Lambda/10$	85
Chapter 4		
4.1	FinFET device, the dimensions are given in units of nanometers. . . .	87
4.2	Brillouin zone for idealized Simple Cubic Lattice including high symmetry points (Γ , X , M , and R)	89
Chapter 4		
4.3	Dispersion surfaces in a quadrant of the $k_z = 0$ plane. The constant frequency contours of the longitudinal acoustic branch are projected below the dispersion surfaces.	91
4.4	Three channel geometries simulated in FinFET device. Channels I, II, and III correspond respectively to the low, medium, and high applied gate voltage conditions [2]. Energy is sourced only into control volumes with centroids lying within the source region.	93
4.5	FinFET dimensions for the three fin widths, all dimensions are in units of nanometers.	94
4.6	Temperature profiles obtained from the FinFET numerical experiment. The three different channel regions are labeled by row. All temperatures are reported in units of Kelvin.	96

4.7	Percent difference in the cell centered temperatures of the FBZ and FBZ- τ models (blue) and the FBZ and IBZ models (red) for control volumes in the xz -plane of the FinFET. The xz -plane corresponding to the plots is outlined in red in the inset schematic.	100
Chapter 5		
5.1	Finite section of chamber-offset NW geometry. The red dotted area denotes a single <i>chamber</i>	111
5.2	Ray tracing through a chamber-offset NW. The red ray contributes to the flux through the wire, however the blue ray experiences a backscattering event and therefore does not increase the total flux. . .	114
Chapter 5		
5.3	Relative reduction of flux through chamber-offset wire vs the inverse of the number of chambers for a range of offset heights. The linear model equation is given in Eq. 5.5	120
5.4	Relative reduction of thermal conductance of chamber-offset NW versus offset height. Both a NW with specular (blue) and diffuse sidewalls (red) are considered.	123
5.5	(a) Thermal conductance of chamber-offset NW versus offset height. Both a NW with both specular (blue) and diffuse sidewalls (red) are considered. (b) The thermal conductivity values for the chamber-offset NW vs. offset height. The grey triangles represent the Casimir limit prediction for the thermal conductivity for a straight NW with square cross section of width $W - H$. The specular case for $H = 0$ is neglected as this corresponds to the bulk Si value.	124
5.6	Thermal conductance accumulation for (a) smooth and (b) rough NWs.	125
5.7	Relative contribution to thermal transport from discrete regions of frequency spectrum in (a) smooth and (b) rough NWs.	127
5.8	Plots of the flux misalignment, θ' , for r values (a) $r = 1/5$, (b) $r = 2/5$, (c) $r = 3/5$, and (d) $r = 4/5$. The plane Γ_x is shown as the shaded area in (e).	130
5.9	Flux weighted angle, θ_{fw} , contours for both the specular (b, d) and diffuse (a, c) NWs with r values (a, b) $r = 1/5$ and (c, d) $r = 4/5$. The cross-sections correspond to the NW centerline $\hat{x}\hat{y}$ plane located at $z = W/2$	132
5.10	Two nanodevice geometries (a) v1 and (b) v2.	133
5.11	Plots of the relative conductance reduction (a) and absolute conductance values (b) for geometries v1 (blue) and v2 (red).	134
Chapter 6		
6.1	Physical domain representing a hotspot in RDX. The sphere indicates the hotspot region. Due to the symmetry, the simulation domain reduces to the shaded octant.	147

6.2	Frequency surfaces of first 14 branches in the quadrant of the $k_z = 0$ plane of the BZ.	150
6.3	Stair plot of the group velocity component magnitudes vs. frequency.	151
6.4	Stair plot of specific heat vs. frequency.	151
6.5	TCA vs. frequency for all three principle directions.	153
6.6	Histogram of phonon mode stretches for the EQ (top) and UNI (bottom) case. The abscissa is expressed in units of fraction of the average N-N bond length.	154
6.7	Plot of N-N bond stretch contribution from discrete intervals in the frequency spectrum. The bond stretch has units of angstroms.	155
6.8	SED vs Frequency for an optical branch of 2x2x2 supercell.	156
6.9	Phonon Lifetimes vs Frequency for RDX 2x2x2 supercell.	157
6.10	: Number of phonon modes vs phonon relaxation time for RDX 2x2x2.	158

Chapter 6

6.11	: Total energy along three Cartesian directions emanating out from the hotspot center.	160
6.12	Flux components along the Cartesian directions emanating from hotspot center. The vertical black line indicates the hotspot boundary.	161
6.13	Contributions of (a) large EQ stretching modes and (b) large UNI stretching modes to the thermal flux along all three principal directions.	163

List of Abbreviations

3D	three dimensions
1D	one dimension
GF	Green's function
DFT	density functional theory
LD	lattice dynamics
MD	molecular dynamics
BTE	Boltzmann transport equation
pBTE	phonon Boltzmann transport equation
MOSFET	metal-oxide-semiconductor field-effect transistor
FinFET	fin field-effect transistor
BZ	Brillouin zone
FBZ	full Brillouin zone
RDX	full Brillouin zone
RTA	relaxation time approximation
MFP	mean free path
Kn	Knudsen number
LBM	lattice Boltzmann method
SMRT	single mode relaxation time
TTG	transient thermal grating
TDTR	time domain thermoreflectance
BB-FDTR	broadband frequency domain thermoreflectance
INS	inelastic neutron scattering
LA	longitudinal acoustic
LO	transverse optical
MC	Monte Carlo
GULP	general utility lattice program
DFPT	density functional perturbation theory
RMS	root mean square
NN	nearest neighbor
NNN	next nearest neighbor
IBZ	isotropic Brillouin zone
FBZ τ	full Brillouin zone with isotropic scattering
MEMS	microelectrochemical systems
NWs	nanowires
FBZ-BTE	full Brillouin zone Boltzmann transport equation
BCs	boundary conditions
v1	nanodevice geometry 1
v2	nanodevice geometry 2
TC	thermal conductivity

TCA	thermal conductivity accumulation
NMD	normal mode decomposition
LAMMPS	large scale atomic/molecular massively parallel simulator
SED	spectral energy density
N-N	nitrogen-nitrogen
EQ	equilibrium
UNI	uniform
CADOM	control angle discrete ordinates method

Chapter 1: Introduction

Thermal transport processes play a key role in the material behavior of a wide-array of important microscale engineering problems [3, 4]. For example, the overheating and energy dissipation in field effect transistors [5–12], energy conversion efficiency in thermoelectric devices [13–20], and initiation in energetic materials [21–29] are all processes which are inextricably linked to the microscale thermal behavior of these systems [30]. At the microscale, continuum descriptions of heat transfer, such as Fourier’s Law, break down. Therefore, accurate modeling of thermal transport requires consideration of the phonons, i.e. collective vibrations of the atomic lattice, which are the fundamental carriers of heat in non-metals. The importance of accurate modeling of microscale thermal transport properties will only continue to grow as an increasing number of devices operate in the sub-continuum regime. Amongst such devices are the transistors on computer chips and nanowires in thermoelectric devices, both of which are undergoing rapid reduction in size in order to increase computing power and thermoelectric efficiency, respectively. Therefore, accurate phonon modeling holds promise for resolving numerous engineering challenges such as improved transistor design, increased thermoelectric efficiency, and improved control over the initiation of energetic materials.

There exists a wide array of numerical approaches for the simulation of phonons, i.e. computational phononics. The length scale domain to which a computational phononics approach applies is delimited by important phonon wave properties, including phonon wavelength and mean free path, as well as the system size. In the sub-continuum regime, where length scales are on the order of the phonon mean free path or smaller, prevailing computational approaches include density functional theory (DFT), lattice dynamics (LD), molecular dynamics (MD), and the Boltzmann transport equation (BTE). The length scales at which these approaches are applicable are depicted in Fig. 1.1. Of these approaches DFT, LD, and MD all retain the

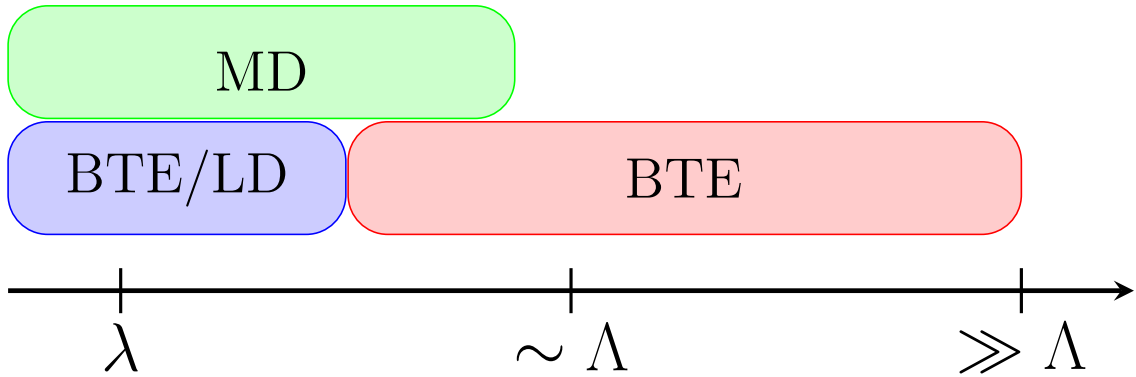


Figure 1.1: Length scales of applicability of the LD, MD, BTE, and DFT methods. In this figure λ represents the phonon wavelength while Λ represents the phonon mean free path.

complete atomic description of the system allowing for the calculation of important wave properties such as vibrational mode shapes and vibration spectrum. However, retaining all atomistic information comes at a high computational cost and these approaches are limited to length scales on the order of the phonon wavelengths. In

contrast, the phonon BTE neglects phase effects allowing it to access longer length scales on the order of the phonon MFP. Therefore, as this thesis will focus on material systems in which important thermal processes occur at both the nano- and micro- scale, the phonon BTE will be best equipped for studying relevant thermal transport problems.

1.1 Challenges Associated with Phonon Modeling

The phonon Boltzmann transport equation (BTE) describes the spatial and temporal evolution of the phonon distribution for *all* phonon modes present in a system. The phonon BTE is written [31]

$$\frac{\partial N}{\partial t} + \mathbf{v} \cdot \nabla N = \left[\frac{\partial N}{\partial t} \right]_{\text{collision}}, \quad (1.1)$$

here \mathbf{v} is the phonon group velocity (the speed and direction in which a phonon carries energy), N is the phonon distribution function, and the right side of Eq. 1.1 represents the phonon collision term, i.e. scattering. The challenge of BTE modeling lies in determining the seven-dimensional phonon distribution function, N , which is a function of real space, reciprocal space (i.e. space of vibrational modes), and time. Therefore, numerical approaches may become computationally demanding as discretization must be applied to seven variables. Further complicating the solution process is the fact that the phonon BTE requires a number of key phonon parameters as inputs, such as the group velocities and vibrational frequencies. Accurate calculation of these parameters requires atomistic simulations, such as MD, LD, or DFT. This adds an additional step to the simulation process that may be

computationally demanding, in the case of DFT, or requires access to accurate empirical potentials for certain complex systems, for example when using LD and MD. To deal with these computational challenges, previous Boltzmann transport based research efforts have often resorted to assumptions or approximations when applying the phonon BTE. In particular, two common simplifications are applied when modeling a material system. The first simplification involves reducing the dimensionality of a system by assuming variations in the phonon occupation occur in only one or two spatial dimensions. The second simplification involves approximating the three-dimensional reciprocal space representation of the phonon carriers as zero or one dimensional. We now elaborate on these two common simplifications.

a) 1D/2D Assumption

One of the predominant simplifying assumptions made when solving the phonon BTE is to approximate systems or devices to be nominally one or two dimensional. The earliest numerical solutions of the phonon transport equation considered a semi-infinite nominally 1D domain in order to model phonon transport across a thin film [32, 33]. Subsequent work studied other 2D geometries such as MOSFETs [12, 34, 35] and periodic microstructures [36, 37]. Only in the past decade have fully three dimensional phonon transport simulations begun to appear [30, 36, 38, 39], enabled by the continued increase in computing power. The importance of accurate microscale thermal modeling in three dimensions will continue to grow as silicon-on-insulator (SOI) technology improves, enabling geometrically complex microscale

devices. One such device is the FinFET transistor which has a raised fin geometry, resulting in a temperature profile that varies in three dimensions. Examples of systems that can be effectively modeled as one or two dimensional, as well as a recently developed FinFET device that has temperature profiles that vary in three dimensions, are shown in figure 1.2.

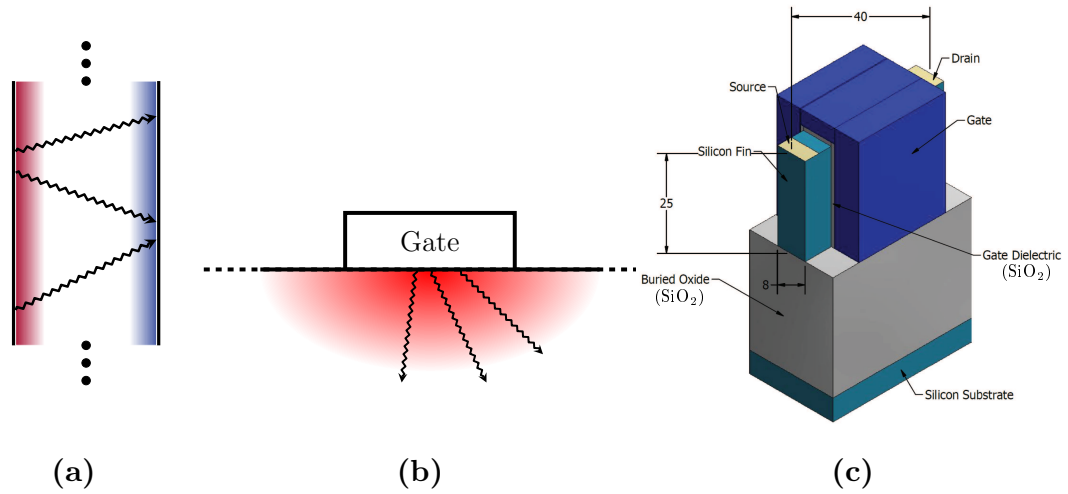


Figure 1.2: Examples of microscale systems that may be regarded as (a) one, (b) two, or (c) three dimensional. Cross-plane heat transport in a thin film (a) is a nominally one dimensional system. Heat flow in a planar MOSFET (b) can be modeled as a two dimensional system. Current generation transistors such as a FinFET (c) have thermal profiles which vary in all three dimensions.

b) Simplified BZ Representation

Another common challenge in the solution of the phonon BTE is the accurate representation of the full Brillouin zone (FBZ), i.e. the subset of reciprocal space containing all unique vibrational modes that exist within a material. Phonon wave

properties influencing energy transport include the phonon frequency, group velocity, specific heat, and lifetime. These phonon parameters depend on the vibrational mode in question, where the vibrational mode is uniquely indexed by wavevector, \mathbf{k} , and branch, λ . In an infinite crystalline material the wavevector \mathbf{k} varies continuously within the FBZ. Early solutions of the phonon BTE assumed the phonon parameters could be replaced by a single averaged value, which implicitly collapses the Brillouin zone to a single point, i.e. the *gray* phonon assumption [8, 32, 40, 41]. The gray assumption fails to account for the fact that the phonon frequencies, lifetimes, and group velocities each take on range of values that span several orders of magnitude, therefore leading to inaccurate predictions of thermal properties [12]. To remedy the failures associated with the gray phonon model, researchers incorporated dispersion characteristics by calculating the phonon parameters along a single direction in the FBZ and took the phonon parameters to be radially symmetric, effectively replacing the true Brillouin zone with a sphere of radially symmetric dispersion [38, 39, 42–44]. Figure 1.3 compares the full Brillouin zone representation to the simplified isotropic representation. While the isotropic dispersion model increases accuracy relative to the gray model, it necessarily ignores the fact that phonon parameters are, in general, anisotropic in the BZ. Furthermore, research of phonon transport in thin films has indicated that anisotropy has a significant effect on thermal conductivity predictions in microscale systems [45], even if the macroscopic anisotropy of the constituent material is relatively weak. Therefore, accurate modeling of phonon transport in micro- and nano- scale devices requires a FBZ representation.

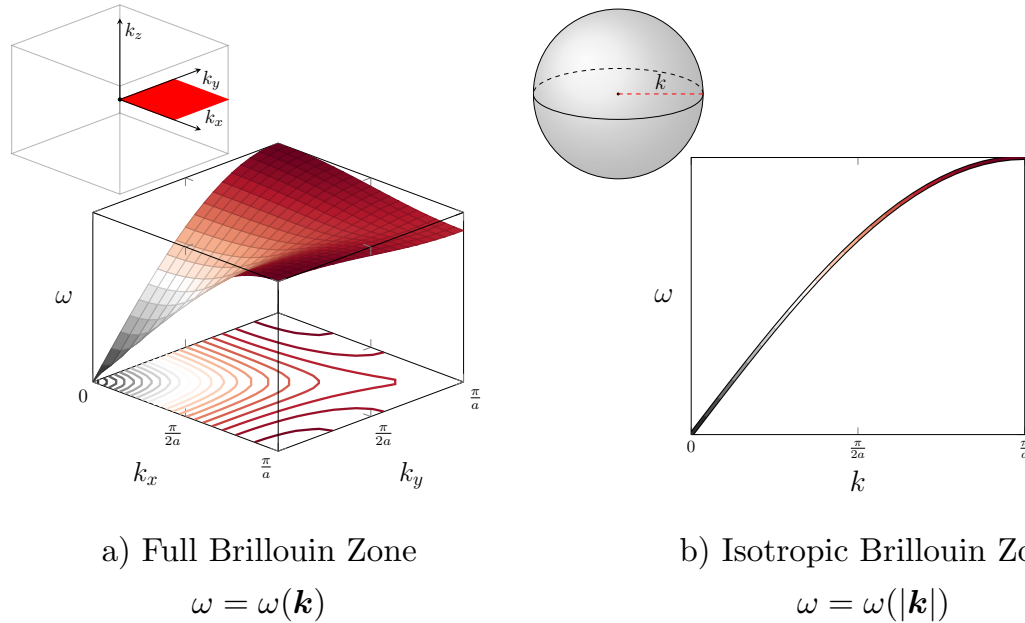


Figure 1.3: Comparison of a full Brillouin zone representation (a) versus the simplified isotropic dispersion representation (b). The constant frequency contours of the $k_z = 0$ plane in the isotropic Brillouin zone are circular sections. The gray approximation is not shown as it collapses the BZ to point where dispersion has no meaning, i.e. ω is a constant independent of wavevector \mathbf{k} .

1.2 Research Outline

The feasibility of three dimensional phonon transport simulation, coupled with full Brillouin zone phonon inputs, means we can now accurately simulate thermal effects in novel 3D device structures. These simulations could, in turn, inform how to engineer microscale devices with desirable thermal properties. Among the device geometries that have gained widespread interest in recent years are three dimensional FinFET transistors and silicon nanowire based thermoelectric systems.

These systems can be used to manufacture smaller transistors, leading to increased microchip computing power, and more efficient thermoelectric devices. However challenges remain such as efficient heat removal in FinFETs and nanowire device design for improved energy conversion capability in nanowire-based thermoelectrics. In addition to engineering phonon behavior in semiconducting systems, the phonon BTE may be used to better understand thermal transport properties in energetic molecular crystals. Advances in knowledge of thermal processes in energetics will allow for greater control over the sensitivity of these systems. Thus accurate 3D phonon modeling will aid in addressing a range of engineering challenges, ushering in smaller, more efficient semiconducting devices as well as highly controllable energetic systems.

The aim of this dissertation is to address these challenges through the development, and subsequent application, of a FBZ three dimensional phonon BTE solution methodology. In Ch. 2 we will cover the fundamentals of phonon theory, providing the reader with the prerequisite knowledge and intuition required for the remainder of the work. We also present a brief overview of the various numerical approaches for solving the phonon BTE.

In chapter 3 we will present an original phonon BTE solution method which accurately captures phonon transport behavior in three dimensions, accounting for the full range of phonon properties throughout the Brillouin zone. In addition we will describe the approach for determining the relevant phonon parameters required as inputs. The methodology will be verified through comparison to exact analytical solution to the BTE. The method will be used in chapters 4-6 to address three critical

microscale thermal engineering problems. Each of these investigations represents original work published by the author in [30], [46], [47], and [48].

Chapter 4 presents an investigation into the effects of anisotropy in a FinFET composed of a cubic lattice material. FinFETs represent the new generation of transistor technology consisting of a raised fin appendage surrounded on three sides by a gate (see fig. 1.2). This fin geometry allows for greater control over the transistor performance and decreased power consumption. However, due to the extreme scaling of the transistor dimensions (Intel's newest chips boast a characteristic dimensions < 20 nm) there is a large increase in boundary scattering, exacerbating Joule heating effects which may lead overheating and device failure. We perform a numerical experiment of a FinFET device, accounting for Brillouin zone and finite lattice effects on anisotropy. We extract the temperature profiles within the FinFET and analyze the role that anisotropic heat carriers play.

In chapter 5 we investigate the thermal conductance of a silicon nanowire with a chamber-offset geometry. This investigation is performed in the context of a recent surge in interest in the use of Si nanowires as components in thermoelectric devices. The interest in Si nanowires as a thermoelectric component is due to the prevalence of Si and the fact that Si nanowires have a thermal conductivity a factor of 10-100 times less than bulk silicon. As thermoelectric efficiency is inversely proportional to thermal conductivity, Si nanowires hold promise as thermoelectric components. Furthermore, a number of recent papers have found that modifying the geometry of Si nanowires may lead to further thermal conductivity reduction. In light of these studies, we consider a Si nanowire with periodically offset sections, finding that

this geometry has desirable thermoelectric characteristics and is a better candidate geometry for reducing thermoelectric flux than previously studied geometries. In addition we analyze the interior flow nature of phonons through the nanowire and consider the possible applications of the nanowire design as a "thermal filter."

Chapter 6 delves into the important role phonons play in the initiation processes of energetic crystals. Specifically, we study the molecular crystal RDX. It is believed that phonons play a key role in energetics via the "up-pumping" mechanism in which energy deposited into low-energy phonon modes is transferred, via phonon-phonon interactions, into higher frequency intramolecular vibrations which are closely linked with chemical decomposition and ultimately detonation. Therefore, we perform a careful examination of the phonon mode lifetimes in RDX as well as phonon transport in the vicinity of an RDX hotspot. Hotspots in energetic materials are localized regions of higher energy density and are believed to be the location where chemistry begins. In addition we parse the mode-wise contribution to thermal transport with special attention paid to phonon modes that are closely linked with Nitrogen-Nitrogen (N-N) bond stretching.

In chapter 7 we present a summary of our findings and identify key scientific questions for future work.

Chapter 2: Phonon Theory and Simulation ¹

In the first section of this chapter we present the fundamentals of phonon theory where, in the interest of pedagogy, we develop intuition for phonon behavior in microscale regimes. Specifically, we consider a one-dimensional model crystalline solid which avoids the cumbersome mathematical machinery required for the study of phonons in a real material. Subsequently, we outline the lattice dynamics approach and detail the mathematical framework for calculating the wave properties of phonons in a general crystalline system. The section concludes with a description of anharmonic effects, the role they play in thermal transport, and how they are handled within a modeling framework.

In section 2.2 we introduce the phonon Boltzmann transport equation which will be used throughout this work to model microscale phonon transport. A brief history of the solution techniques of the phonon BTE is presented along with a description of the microscale systems which have been studied using Boltzmann transport modeling.

¹Portions of this chapter appeared in the publication: *F. G. VanGessel, J. Peng, and P. W. Chung, A review of computational phononics: the bulk, interfaces, and surfaces. J. Mater. Sci. (2017) [47]*

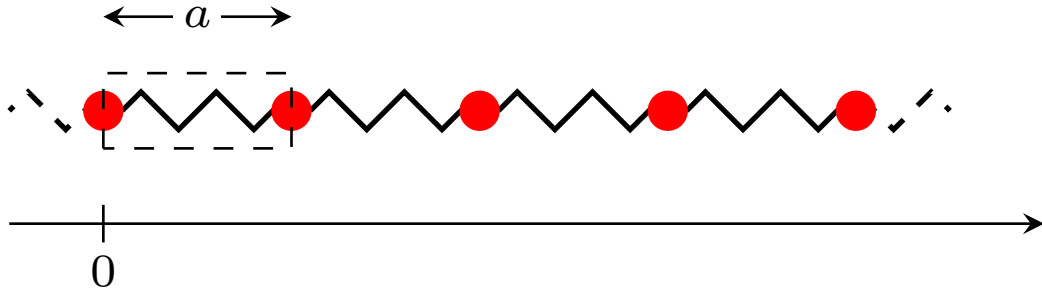


Figure 2.1: A 1D crystalline system consisting of atoms of mass m . Each mass is connected to its nearest neighbor via a linear spring. The spacing between nearest neighbors is a . The outline of the unit cell of the crystal is indicated by the dashed line.

2.1 Phonon Theory

2.1.1 1D System

In order to establish intuition for what constitutes a phonon, consider the simple one-dimensional crystalline system depicted in Fig. 2.1. A system is crystalline if it is composed of a periodic tiling of unit cells, where each unit cell contains an identical configuration of atoms (referred to as a *basis*). In our one-dimensional crystal, each unit cell, denoted by the dashed box, contains a single atom of mass m located at the left-hand side of the unit cell. Furthermore, each unit cell is repeated with a period of a and corresponding to each unit cell is an index l , where l is an integer. Therefore, the equilibrium position of the atom belonging to unit cell l is located at $r_l^0 = la$. Since the basis consists of only a single atom, and the system

is one dimensional, there is only a single phonon *branch* and vibrational modes are uniquely indexed by wavenumber k . In order to visualize the vibrations of atoms associated with a phonon, we take the motions to be *transverse* with respect to the orientation of the chain. In a materials of a higher dimensions, there exist both transverse and longitudinal polarizations of the atomic motion, termed the transverse phonon branch and longitudinal phonon branch respectively. Furthermore, systems with two or more atoms in the basis will contain multiple transverse and longitudinal phonon branches. In the following discussion we will refer to k as the wavevector, with the implicit knowledge that k corresponds to a single scalar component. We will now derive the phonon mode shapes, frequencies, and group velocities of all vibrational modes, indexed by k , in this crystal.

Begin by writing the equation of motion for an arbitrary atom affixed to unit cell l ,

$$m\ddot{u}_l = A(u_{l+1} - u_l) - A(u_l - u_{l+1}) = A(u_{l+1} + u_{l-1} - 2u_l) \quad (2.1)$$

here A is the spring constant. As we are seeking solutions of the plane-wave form, let $u_l = C_0 e^{i(kal - \omega t)}$. Inserting the functional form of u_l into Eq. 2.1 yields

$$-m\omega^2 = A [e^{ika} + e^{-ika} - 2] , \quad (2.2)$$

which upon rearrangement gives

$$\omega(k) = \sqrt{\frac{2A}{m}} [1 - \cos(ka)]^{1/2} \quad (2.3)$$

Thus we have an analytical form for the frequency of all phonon modes in the 1D chain. For an infinitely long crystal, the wavevector k is a continuous variable. Note

that the phonon mode shape is periodic under any translation of the wavevector by an integer multiple, n , of $2\pi/a$, i.e.

$$\begin{aligned}
u_l(k + 2\pi n/a) &= C_0 e^{i[(k + \frac{2\pi}{a}n)al - \omega t]} \\
&= C_0 e^{i[kal - \omega t]} e^{i2\pi ln} \\
&= C_0 e^{i[kal - \omega t]} \\
&= u_l(k) .
\end{aligned} \tag{2.4}$$

Thus all unique vibrational modes of the system are contained within a finite range of wavevectors where, by convention, we assign k to the interval $[-\pi/a, \pi/a]$. The region extending from $-\pi/a$ to π/a is called the *Brillouin zone* of our crystalline system. The equivalence of points falling outside the Brillouin zone to points within the Brillouin zone is visualized in Fig. 2.2.

From Fig. 2.2 one can see that all wavevectors falling outside the Brillouin zone may be mapped into the Brillouin zone, through the appropriate addition of $2\pi n/a$ where $n \in \mathbb{Z}$, where the corresponding atomic vibrations are invariant under the mapping. The frequency-wavevector relation is termed the phonon *dispersion curve*, and is plotted over the entire Brillouin zone in Fig. 2.3. The single curve, i.e. transverse phonon branch, is indicative of a one-dimensional system with a monatomic basis. The dispersion curve is zero at the Brillouin zone center and approaches a maximum, $\omega_{\max} = \sqrt{4A/m}$, at the Brillouin zone boundary. In a three-dimensional material the three low frequency branches, i.e. *acoustic* branches, follow a similar trend. In addition to visualizing the phonon wavevector-frequency relation, we can also visualize the displacements due to a phonon of wavevector k , i.e. the

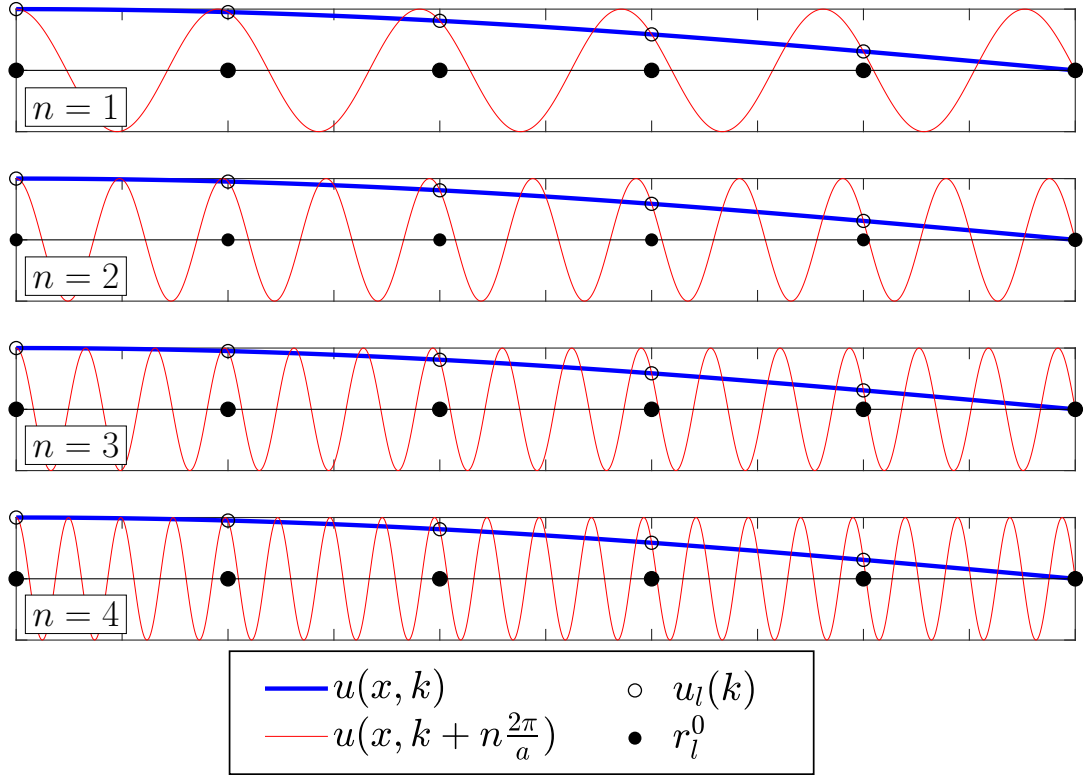


Figure 2.2: Plots of a six atom section, along with corresponding mode shapes, of the one-dimensional crystalline system. The continuous curves corresponding to $u(x, k) = C_0 e^{ikx}$ for $k = \pi/10a$ and $k = \pi/10a + 2\pi n/a$ ($n = 1, 2, 3, 4$) are shown in blue and red respectively. At the points r_l^0 (filled black circles) the displacements corresponding to $k = \pi/10a$ and $k = \pi/10a + 2\pi n/a$ (open black circles) are identical and therefore the atomic motion corresponding to the wavevectors outside the Brillouin zone is indistinguishable from wavevector, k , within the Brillouin zone.

phonon mode shape. These displacements are plotted for five different wavevectors in Fig. 2.4.

Phonons carry mechanical energy as they propagate, the speed at which a phonon propagates is termed its *group velocity*, defined as $v(k) = \partial\omega/\partial k$. In the case

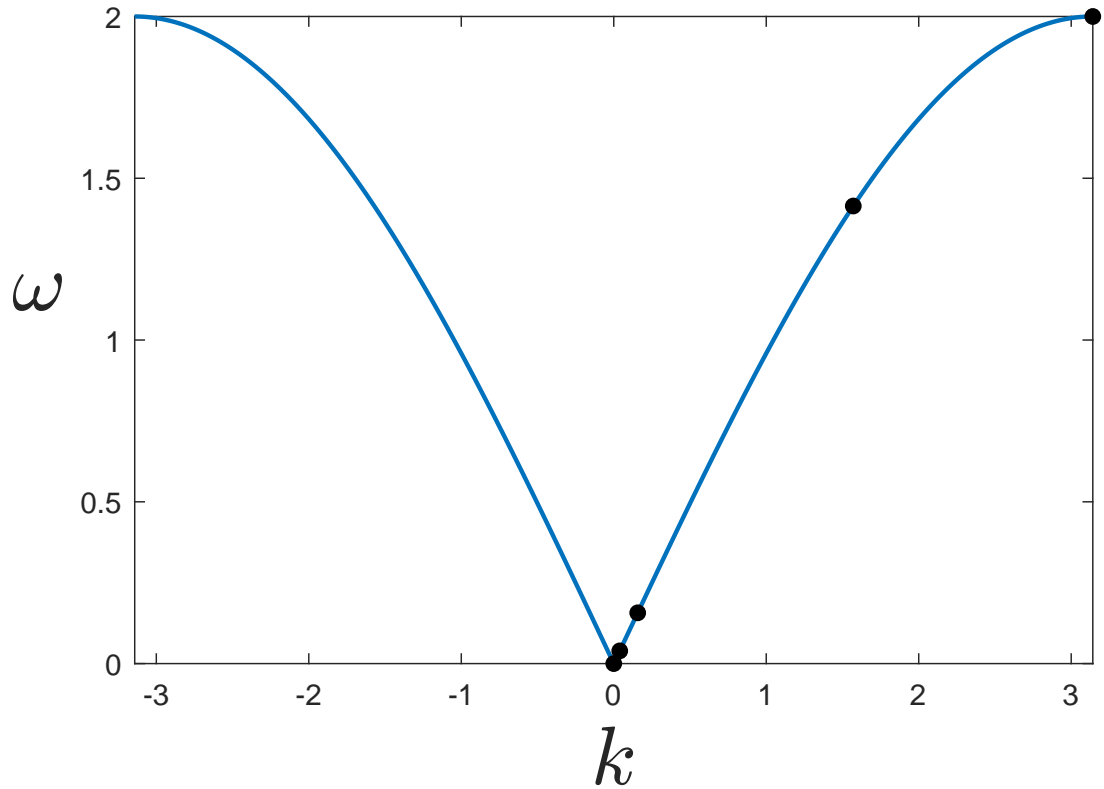


Figure 2.3: Phonon frequencies for 1D chain. The black dots correspond to the phonon modes visualized in Fig. 2.4

of our one-dimensional crystal the group velocity may be calculated analytically, doing so yields

$$v(k) = \left[\frac{Aa^2 \sin^2(ka)}{2m [1 - \cos(ka)]} \right]^{\frac{1}{2}}. \quad (2.5)$$

The relation between group velocity and wavevector is plotted in Fig. 2.5. Note that the group velocity attains a maximum value at the Brillouin zone center where $v_{\max} = a\sqrt{A/m}$ and approaches zero at the Brillouin zone edge. The acoustic modes of real materials follow a similar trend.

Thus far we have referred to vibrational mode and phonon interchangeably, however there is an important, but subtle, distinction between these two concepts. A

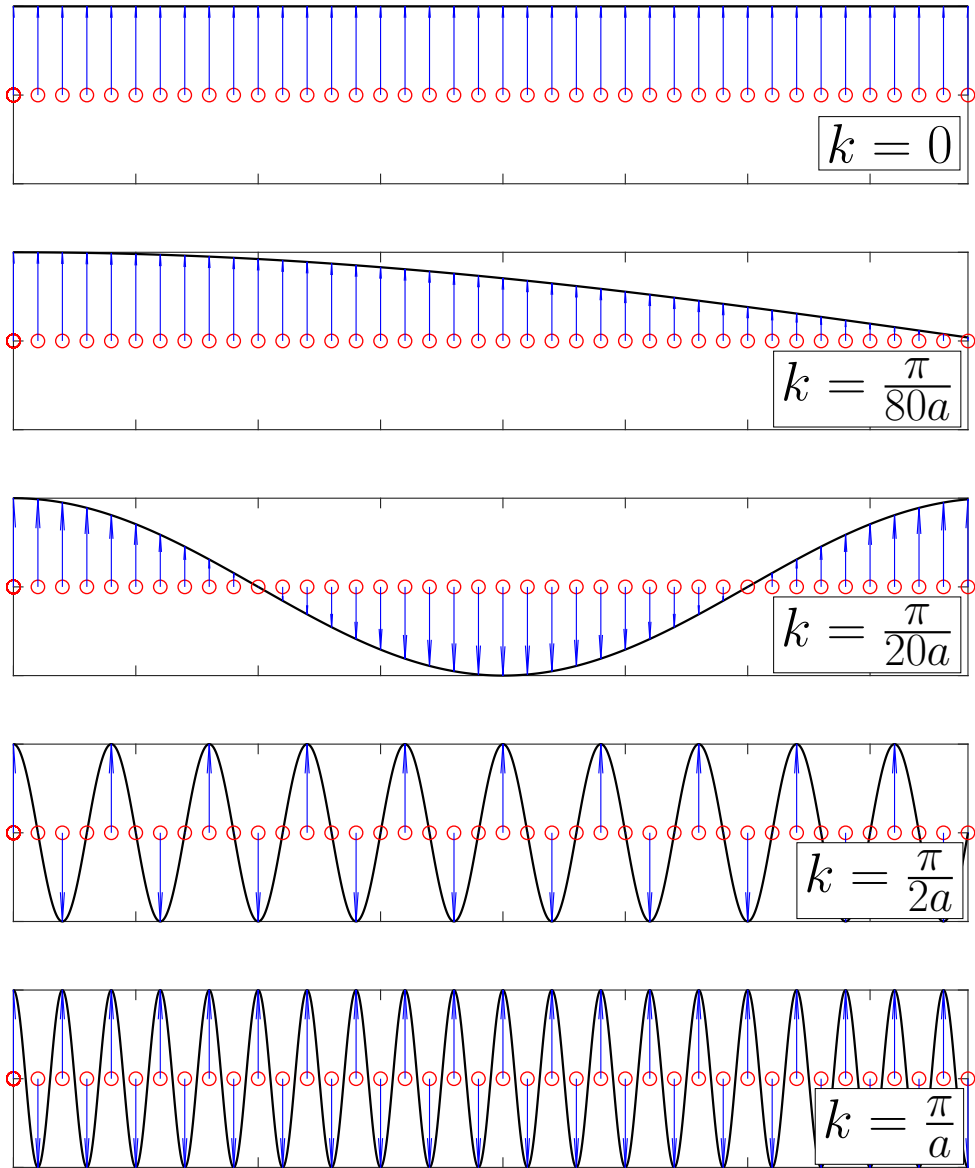


Figure 2.4: Phonon mode shapes for 5 different wavevectors. The equilibrium positions of the atoms are denoted by open red circles. The displacements of the atoms from equilibrium are indicated by blue arrows. The black lines are a visual aid to make the sinusoidal shape of the phonon mode more apparent.

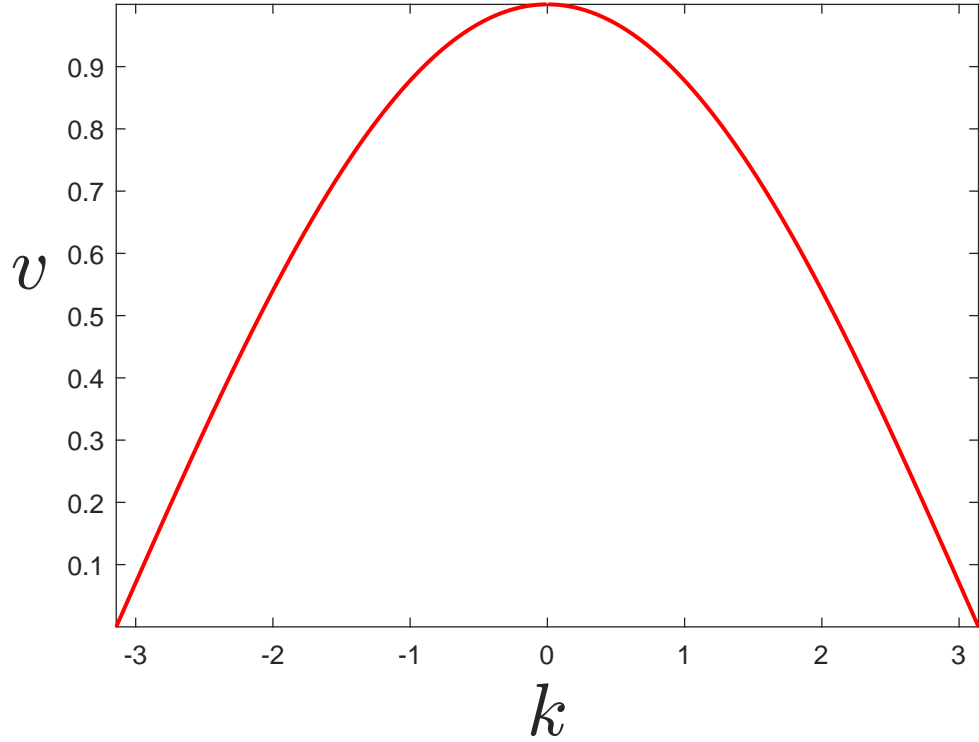


Figure 2.5: Phonon group velocities for 1D chain.

phonon, while corresponding to a single vibrational mode, is only a single quantum of energy within that mode. Therefore within a crystalline material there exists many vibrational modes, each of which contains a varying number of phonons. The number of phonons in a given mode is termed the modal *occupation number*, denoted by $N(k)$.

When a phonon system is in thermodynamic equilibrium at temperature T , the number of phonons in each vibrational mode follows a Bose-Einstein distribution

$$N(k) = \frac{1}{\exp\left(\frac{\hbar\omega(k)}{k_B T} - 1\right)} \quad (2.6)$$

where \hbar is Planck's constant, k_B is the Boltzmann constant, and T is temperature.

At equilibrium the total energy in the vibrational mode is equal to the number of

phonons in the mode, $N(k)$, multiplied by the energy of each individual phonon, $\hbar\omega(k)$, $E(k) = \hbar\omega(k)N(k)$. The amount of energy carried by a vibrational mode is proportional to the modal specific heat, which is calculated as the derivative of the energy stored in a vibrational mode with respect to temperature

$$C(k) = \frac{\partial E(k)}{\partial T} = k_B x^2 \frac{e^x}{[e^x - 1]^2} \quad ; \quad x = \frac{\hbar\omega(k)}{k_B T} . \quad (2.7)$$

The specific heat for all vibrational modes at three temperature regimes (low, medium, and high temperature regimes are taken relative to the quantity $\frac{\hbar\omega_{\max}}{k_B}$) is plotted in Fig. 2.6. Note that at low temperatures only the small k modes carry a substantial amount of heat, while at high temperatures, all vibrational modes carry the same amount of thermal energy.

To understand the role phonon modes of different k play in the transport of thermal energy we invoke the phonon gas model (PGM) of thermal conductivity [49]. Within the PGM framework, each phonon mode represents a quasiparticle that contributes to thermal conductivity κ , we express this relation for a one dimensional system as

$$\kappa = \int_{-\pi/a}^{\pi/a} \kappa(k) dk \quad ; \quad \kappa(k) = C(k)v(k)^2\tau(k) . \quad (2.8)$$

In Equation 2.8, τ represents the phonon relaxation time which will be discussed in detail in sec. 2.1.3 for now we take it to be a constant, $\tau(k) = \tau$. The thermal conductivity contribution from each wavevector is plotted in figure 2.7. Inspection of this figure indicates that phonon modes that correspond to small wavevectors carry a relatively larger amount of thermal energy than large wavevector modes. In fact at low temperatures nearly all the energy is carried by phonons near the Brillouin

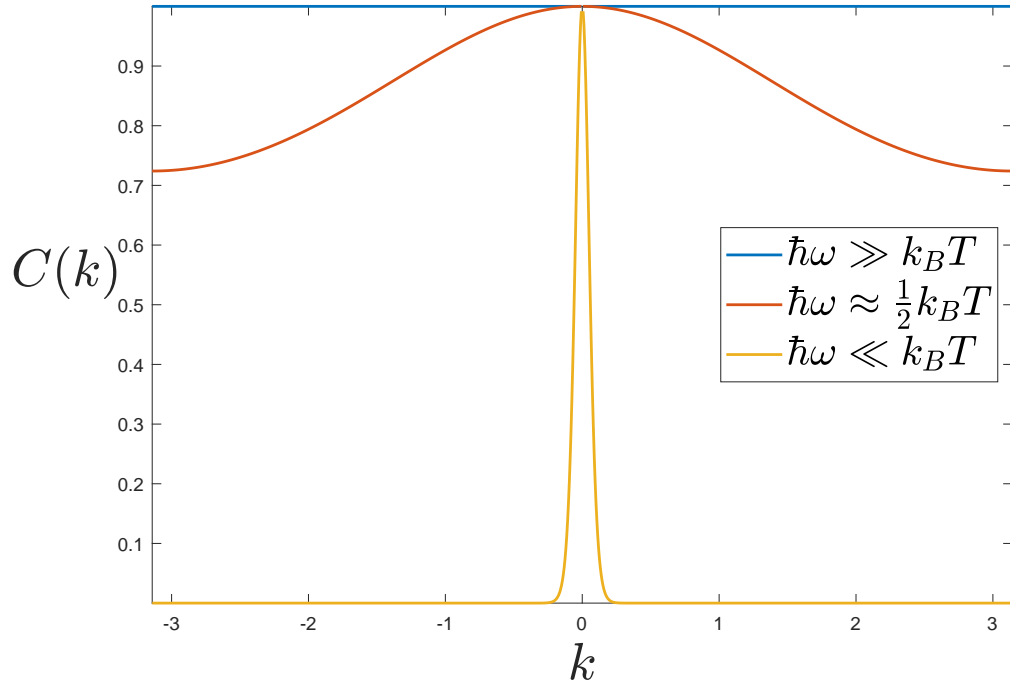


Figure 2.6: The specific heat as a function of wavevector at three distinct temperature regimes.

zone center due to the negligible occupation of phonon modes corresponding to medium and large wavevectors. The total thermal conductivity (the area under the curves in figure 2.7) of the system increases with temperature due to the increase in phonon population of all phonon modes as temperature rises. We stress that the observations made about phonon behavior in our one-dimensional systems are not strict rules and serve only as general guidelines for a real material. In real materials complicating factors include the three-dimensionality of the system, large basis containing many atoms, and complex interatomic potentials. However, these heuristics do provide a reasonable approximation for the behavior of the acoustic phonon branches which dominate heat conduction in most materials.

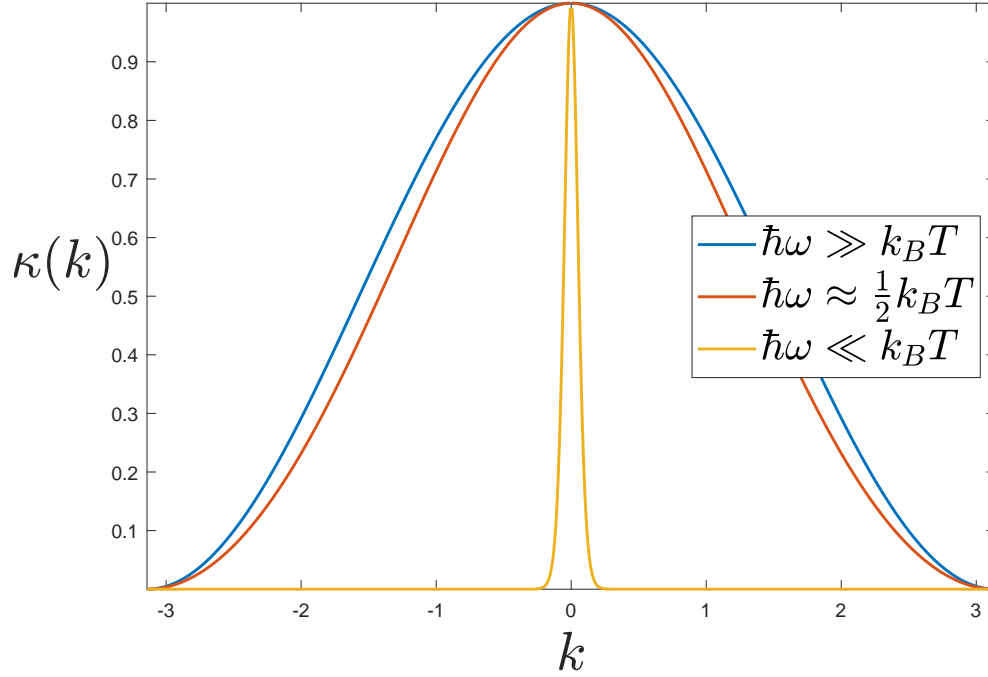


Figure 2.7: The thermal conductivity as a function of wavevector at three distinct temperature regimes.

The phonon specific heat, group velocity, and frequency form three of the four phonon parameters required for pBTE modeling of phonon transport. Here we calculated these parameters for all vibrational modes in one dimensional crystalline system. While we studied an idealized systems, much of the intuition gained here can be applied to more complex systems. Next, we provide a brief overview of lattice dynamics which is the mathematical formalism most often used for calculating phonon parameters in real materials.

2.1.2 Real Materials

We saw in figure 2.4 that phonons represent a delocalized harmonic vibration of atoms within a solid and therefore have wave-like properties such as mode shape and natural frequency. Lattice dynamics methods provide a general framework for the determination of these phonon parameters. We present a brief overview of the lattice dynamics approach here, but for greater detail the reader is referred to one of the many excellent texts on the topic [50–52].

Begin by writing the equation of motion for the displacement $\mathbf{u}(lb)$ of the b^{th} atom in l^{th} unit cell or lattice point,

$$m_b \frac{\partial^2 u_\alpha(lb)}{\partial t^2} = - \sum_{l'\beta} \Phi_{\alpha\beta}(lb, l'b') u_\beta(l'b') . \quad (2.9)$$

Next we assume that the displacement due to wavevector \mathbf{k} is of plane-wave form,

$$m_b u_\alpha(lb; \mathbf{k}) = U_\alpha(\mathbf{k}, b) \exp[i(\mathbf{k} \cdot \mathbf{x}_l - \omega(\mathbf{k})t)] , \quad (2.10)$$

where $U_\alpha(\mathbf{k}, b)$ and $\omega(\mathbf{k})$ are the mode shape and frequency corresponding to wavevector \mathbf{k} and \mathbf{x}_l is the location of the l^{th} lattice site in equilibrium. Under this assumption we obtain the eigensystem

$$\omega^2(\mathbf{k}) \mathbf{U}(\mathbf{k}) = \mathbf{D}(\mathbf{k}) \mathbf{U}(\mathbf{k}) \quad (2.11)$$

where the $3n \times 3n$ dynamical matrix \mathbf{D} , n being the number of atoms in the unit cell, is defined as

$$\mathbf{D}(\mathbf{k}) = \frac{1}{\sqrt{m_b m_{b'}}} \sum_{l'} \Phi(l') \exp(i\mathbf{k} \cdot \mathbf{x}'_l) \quad (2.12)$$

and $\Phi(l)$ is the harmonic force constant matrix representing the interactions between the 0th lattice point (located at the origin) and the l^{th} lattice point. Solution of Eq. 2.11 yields $3n$ eigenpairs, these solutions correspond to the $3n$ branches where the branches will be indexed by λ . Therefore, using lattice dynamics one can determine the mode shapes, $\mathbf{U}(\mathbf{k}, \lambda)$ and frequencies $\omega(\mathbf{k}, \lambda)$ for each phonon mode, $\phi = (\mathbf{k}, \lambda)$, in the system. From the phonon frequencies, it is straightforward to determine the phonon group velocities $\mathbf{v}(\mathbf{k}, \lambda)$ and specific heat, $C(\mathbf{k}, \lambda)$.

In three dimensions, visualization of the phonon dispersion relations, $\omega(\mathbf{k}, \lambda)$ becomes difficult requiring dimensionality reduction for visualization such as, for example, line traces. In this context it is easiest to visualize dispersion surfaces, i.e. "slices" through the Brillouin zone volume for a given branch. An example of such slices for the acoustic branches of Si are shown in Fig. 2.8. Inspection of these dispersion surfaces reveals that the dispersion properties are anisotropic, i.e. the constant frequency contours of ω are *not* circular conic sections. Each branch possesses varying degrees and orientations of phonon anisotropy as measured by the phonon energy flux along various crystallographic directions.

Up until this point all descriptions of the phonon transport properties have been derived under the so-called harmonic approximation. In the harmonic approximation the potential energy function is expanded as a Taylor series about the equilibrium atomic positions and truncated to second order. This approximation is necessary for decoupling the vibrational modes and, as a result, produces the phonon frequencies, group velocities, and specific heat, collectively termed harmonic properties. However, in real materials higher order anharmonic terms in the potential

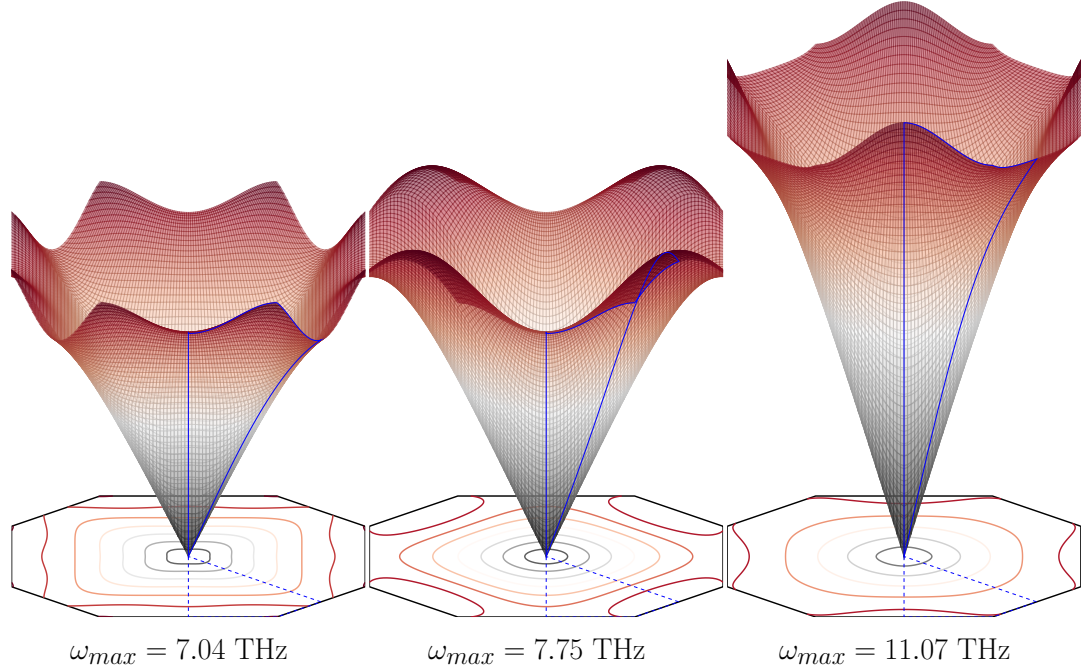


Figure 2.8: Dispersion surfaces of the first three branches (TA, TO, LA) of silicon in the $k_z = 0$ plane. The projected constant frequency contours indicate microscale dispersion anisotropy. The blue lines form an outline of the irreducible wedge of the first Brillouin zone.

energy function play a crucial role, they *couple* phonon modes. Without higher order terms, energy introduced into a given phonon mode would remain in that mode indefinitely. In an anharmonic system when a vibrational mode is excited out of equilibrium, phonon mode coupling relaxes the system back to equilibrium by redistributing the energy amongst all vibrational modes. This coupling process is commonly referred to as *phonon scattering* and represents the final transport property required for phonon BTE simulation. We will now discuss the physics of phonon scattering and common modeling approaches.

2.1.3 Phonon Scattering

In Peierls' seminal paper, "On the Kinetic Theory of Thermal Conduction in Crystals" he describes the importance of anharmonic terms of the potential energy to thermal conductivity of solids [31]. His consideration of third-order (and higher) terms resolves the paradox of infinite thermal conductivity present in harmonic theories of heat conduction. Infinite heat flux arose in harmonic theories due to the lack of coupling between modes. Consider a single mode that is excited out of equilibrium, therefore inducing a heat flux, the mode remains excited indefinitely even in the absence of a temperature gradient. Fourier's Law, $f = \kappa \nabla T$, with a non-zero flux, f , and zero temperature gradient, $\nabla T = 0$, intimates that this situation would indeed lead to infinite thermal conductivity. In contrast, anharmonicity causes energy to be siphoned from the excited mode and redistributed amongst the other vibrational modes, returning the system to equilibrium.

In his 1929 paper, Peierls determined that three vibrational modes can exchange energy contingent on the fact that these modes satisfy certain conservation criteria. Specifically, phonon scattering amongst three phonon modes occurs only if the three modes satisfy conservation of energy and conservation of crystal momentum (modulo a reciprocal lattice vector, \mathbf{G}).

$$\omega_{\phi} \pm \omega_{\phi'} = \omega_{\phi''} \tag{2.13}$$

$$\mathbf{k} \pm \mathbf{k}' = \mathbf{k}'' + \mathbf{G}$$

A numerical modeling approach termed the "full scattering iterative approach," described in sec. 2.2.2.3, enforces the explicit satisfaction of these relationships.

However, rigorous implementation of the scattering term derived in Peierls work is an arduous computational task. This computational difficulty stems from two sources, a search over a grid of wavevectors to identify all three phonon interactions (an $\mathcal{O}(n_k^3)$ algorithm for n_k wavevectors) that obey eq. 2.13 [53], and determination of the anharmonic force constants for each of the allowed three phonon interactions. Furthermore, the wavevector grid must be sufficiently refined to attain accurate results. While full-scattering approaches have certainly been utilized to great effect, see sec. 2.2.2.3, these approaches are predominantly zero-dimensional in nature [54–56], aside from the rare exception [57]. However, simulations of phonon transport in three dimensions eschew the full-scattering approach preferring a computationally simpler, if less rigorous, representation of phonon scattering.

One common simplification of the scattering term is a reversion to the kinetic theory of gases that employs the idea of a relaxation time, i.e. the characteristic time scale for a perturbed distribution to return to equilibrium. The so-called relaxation time approximation (RTA) simplifies the scattering term of eq. 1.1 into the form

$$\left[\frac{\partial N_\phi}{\partial t} \right]_{\text{collision}} = \frac{N_\phi^0 - N_\phi}{\tau_\phi} \quad (2.14)$$

where τ_ϕ is the phonon relaxation time for the ϕ^{th} phonon mode. If we combine eq. 1.1 with eq. 2.14 and set the group velocity to $\mathbf{0}$, we find that $n_\phi(t) = \exp(-t/\tau_\phi)$ where $n_\phi = N_\phi - N_\phi^0$ is the phonon modal occupation *deviation* from equilibrium. Therefore it is clear that the RTA causes the phonon modal occupation to relax toward equilibrium at the characteristic rate τ_ϕ . It is in this relaxation that the RTA indirectly models phonon-phonon collisions (in a pristine crystal these are

the only events that return the distribution to equilibrium), however no discrete collision events are calculated. Since τ_ϕ is an empirical parameter within the RTA model, a wide array of scattering events that occur in a real material, such as phonon-phonon, phonon-electron, impurity, etc., can be included in τ_ϕ . Typically, all scattering processes are incorporated into the RTA framework via Matthiessen's rule which dictates that the total modal relaxation time is calculated as

$$\frac{1}{\tau_\phi} = \sum_s \frac{1}{\tau_s} \quad (2.15)$$

where s indexes the various scattering processes. The most important type of scattering in the context of this work is phonon-phonon, or intrinsic, scattering caused by anharmonicity. Therefore, we assume for the remainder of this chapter that τ_ϕ refers to phonon-phonon scattering only.

The empirical formulas for τ_ϕ are generally expressed as a function of ω_ϕ^α and T , where α is a fitting parameter. In contrast to modeling all three phonon interactions within the full-scattering model, the assumption of a simple functional form for τ_ϕ greatly reduces the computing effort, as the relaxation time may be calculated directly from the phonon frequencies. It should be noted that caution must be taken when invoking the RTA as the use of the RTA introduces an inherent restriction on the types of heat transport phenomena that can be studied by the phonon BTE. Heat transport processes, for which modeling via the BTE using RTA, should occur over time scales longer than the slowest characteristic scattering time scale, i.e., phonon-phonon, phonon-electron, and impurity [58]. In this work we make use of the phonon relaxation time approximation, calculating the relaxation

time separately for each mode. To ensure the validity of our model, we restrict our studies to systems of sufficiently long time scales such that the RTA is a valid descriptor of intrinsic scattering. Further details for this calculation procedure are given in Sec. 3.3. We now provide a brief overview of numerical phonon BTE solution methods.

2.2 Phonon Boltzmann Transport Modeling

2.2.1 Phonon Boltzmann Transport Equation

We stated in chapter 1 that this dissertation will use the phonon BTE to investigate phonon behavior in a number of microscale systems. In this section we will describe the BTE in greater detail. Specifically, we will outline its derivation, how phonons are represented within the BTE framework, as well as important length scale considerations.

The BTE as written in eq. 1.1 governs the phonon distribution function N . We rewrite this equation, making the mode dependence, ϕ , explicit

$$\frac{\partial N_\phi}{\partial t} + \mathbf{v}_\phi \cdot \nabla N_\phi = \left[\frac{\partial N_\phi}{\partial t} \right]_{\text{collision}} . \quad (2.16)$$

The terms on the left-hand side of Eq. 2.16 indicates the phonon distributions vary with respect to both time and space, whereas the right-hand side represents the anharmonic coupling of phonon modes which may be treated with varying degrees of rigor. Within the RTA framework one can define the characteristic distance that a phonon of mode ϕ travels before experiencing a collision or scattering event

as the phonon mean free path (MFP), Λ_ϕ , where $\Lambda_\phi = |\mathbf{v}_\phi|\tau_\phi$. The MFP represents an important length scale, demarcating regimes of applicability of the phonon BTE. Phonons modeled using BTE are consistent with the wavepacket description of phonons, which represents the phonons as localized particles [51]. Wavepackets are formed from a weighted superposition of phonons modes from a small region of the Brillouin zone, resulting in a packet of vibrational energy that is spatially localized [59]. The BTE has been derived from energy conservation rules leading to an equation of motion [51]. Alternative derivations begin with the Liouville equation governing the time rate of change of the system probability density function [59]. By considering a single phonon mode ϕ and marginalizing over the remaining modes, the system probability function is projected onto a single-mode distribution function, f_ϕ . Applying this projection approach to the Liouville equation yields the BTE.

Note that Eq. 2.16 corresponds to the phonon BTE for a single phonon mode. Rigorously, a phonon mode is defined by a four-dimensional vector: a three-dimensional wavevector and a polarization number, thus technically, there are as many phonon Boltzmann transport equations as there are unique phonon modes. In the continuum limit, ϕ is a continuous variable which means there is an infinite number of equations governing the phonon distribution function. The distinction between whether a system is discrete or continuous is made based primarily on the number of phonon modes in the system. In the discrete case, the Born-von Karman boundary conditions [60] are the periodic boundary conditions, applied to a discrete set of atoms in a supercell, that lead to the requirement that the wavevector \mathbf{k} and

dimensions \mathbf{L}_i of the supercell lattice vector must satisfy $\exp(i\mathbf{k} \cdot \mathbf{L}_i) = 1$. Thus, the set of phonon modes is discrete. As an example, consider a cubic lattice where the supercell is defined by a tiling of N_l unit cells, for $l \in (1, 2, 3)$. Then, the neighboring wavevectors along the direction corresponding to $l = 1$ will be separated by a distance $\Delta k_1 \propto 1/N_1$. Likewise, along direction 2 and 3, the wavevectors are spaced proportionally to $1/N_2$ and $1/N_3$, respectively. Then, it is clear that in the limit of a system containing a large number of unit cells, the distance between wavevectors vanishes. In that limit, the wavevectors in the BTE problem are continuous variables and the set of allowed vectors is infinite. The vast majority of phonon transport studies have assumed the system of study to be large enough that the wavevector can be taken as a continuous variable. However, for small system size the distinction between discrete and continuous is important. Consider, for instance, lattice-scale anisotropy of thermal transport where the discreteness naturally gives rise to anisotropic effects, whereas the analogous continuous wavevector representation is otherwise isotropic. This effect will be further demonstrated in Chs. 3 and 4.

The BTE is well suited for modeling phonon transport in devices with characteristic dimensions large enough so that phonon properties are bulk-like [61]. Phonon properties may be considered bulk-like when the number of modes is sufficient to allow for the formation of wavepackets and when phase effects, namely constructive or destructive interference, are negligible. The latter effect, often referred to as coherency, is tantamount to averaging over all phases. Gurevich [51] refers to this assumption as "quantum mechanical averaging" which necessarily leads to the loss

of phase information. Both the assumption of sufficient vibrational modes and negligible coherent effects are key in the derivation of the phonon BTE [51]. Turney et al. [61] found that thin films of thickness 4.3 and 17.4 nm, for LJ argon and silicon, respectively, exhibited bulk-like densities of states and therefore represent a reasonable lower size limit for modeling by BTE. The BTE may technically be applied to the modeling of phonons in any material with characteristic length scales large enough to exhibit bulk-like dispersion characteristics. However, such an approach would be computationally inefficient for simulation of systems with characteristic lengths much larger than the dominant heat carrier MFP. At length scales much larger than the MFP, phonon transport is primarily diffusive and other approaches, such as Fourier’s heat equation, may be applied with negligible error [62]. The Knudsen number, $Kn_\phi = \Lambda_\phi/L_c$, provides a quantitative discriminator for determining whether a purely diffusive model is sufficient. It is a problem-dependent quantity defined as the ratio between Λ_ϕ , the phonon MFP, and L_c , a characteristic length scale in the flow domain. The characteristic length scale, L_c , may be, for instance, the spot size radius of a collimated laser used to heat a sample in a time domain thermoreflectance experiment [63], the spacing of the thermal grating in a transient thermal grating experiment [64], or the film thickness for heat conduction in a thin film [65]. Note that the phonon MFP’s within a given material span a large range of values, therefore resulting in a range of Knudsen numbers. Large values of the Knudsen number ($Kn_\phi \gg 1$) indicate phonon mode ϕ is a ballistic carrier, while small numbers ($Kn_\phi \ll 1$) imply a diffusive carrier. When applying Fourier’s Law, or other continuum approaches, one should take care to ensure all relevant carriers

in the system correspond to a small Knudsen number.

In the next section we detail the prevailing numerical techniques for solving the phonon BTE.

2.2.2 Numerical Methods

Solving the BTE numerically requires the consideration of three key components to each model:

- real space representation
- reciprocal space representation
- scattering model

The existing numerical techniques may be grouped, roughly, according to the component they emphasize. Some approaches seek to account for multiple components simultaneously. A table summarizing the spatial domain complexity, reciprocal space accuracy, and scattering term associated with hypothetical BTE model emphasizing a certain component is shown in table 2.1. Here, we review efforts that appear to emphasize a key development or finding and describe their assumptions that contribute to physical accuracy.

2.2.2.1 Real Space Discretization

The real space discretization is the discretization over the domain defined in the coordinate system of the physical body. Existing modeling methods use

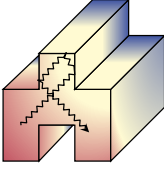
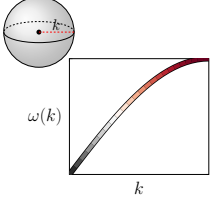
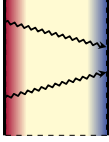
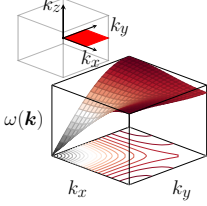
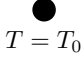
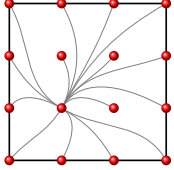
Component of Focus of BTE Model	Spatial Domain Complexity	Reciprocal Space Accuracy	$\left[\frac{\partial N}{\partial t} \right]_c$
Real Space Representation			$\frac{N_\phi^0 - N_\phi}{\tau_\phi}$
Reciprocal Space Representation			$\frac{N_\phi^0 - N_\phi}{\tau_\phi}$
Scattering Model			$\sum_{\phi' \phi''} \left[(\Psi_{\phi''} - \Psi_{\phi'} - \Psi_\phi) \Lambda_{\phi\phi'\phi''}^+ + \frac{1}{2} (\Psi_{\phi''} + \Psi_{\phi'} - \Psi_\phi) \Lambda_{\phi\phi'\phi''}^- \right]$ <p>subject to $\begin{cases} \omega_\phi \pm \omega_{\phi'} = \omega_{\phi''} \\ \mathbf{k} \pm \mathbf{k}' = \mathbf{k}'' + \mathbf{G} \end{cases}$</p>

Table 2.1: Comparison of the three types of phonon BTE numerical solution techniques, each of which emphasizes a certain component of the BTE model: real space, reciprocal space, or scattering. The primary differences between these types are the complexity of the spatial domains to which they are applied, how they represent the Brillouin zone (isotropic, anisotropic, or explicit calculation of mode to mode coupling), and how phonon-phonon scattering is modeled.

real space discretizations based on finite difference, finite volume, or finite element techniques. Methods based on a finite difference approximation are most often associated with the so-called lattice Boltzmann method (LBM) [45, 66]. The lattice Boltzmann method discretizes the spatial domain into a regular grid of points. Often the temperature field is sought that accounts for both ballistic (phonons that travel without scattering) and diffusive (phonons that undergo many scattering events)

thermal energy carriers. Due to the discretization of the angular domain, i.e. the set of all possible phonon propagation directions, into a small number of directions, temperature fields obtained from the LBM may be grid dependent, especially in the ballistic regime [45]. This behavior arises from the restriction of flow only along a fixed set of directions that correspond to grid lines between nearest neighbor grid points. The overwhelming majority of LBM simulations use grids with either six or eight nearest neighbor grid points. As a result, there are a relatively small number of allowed propagation directions, leading to the so called "ray-effect" in the ballistic regime. Other approaches such as the finite volume approach allow for refinement of the spatial and angular grid independently of one another. Therefore, these methods can achieve a relatively larger number of propagation directions, mitigating such ray-effects [67]. Modifications and advancements to the LBM have been made to better capture a wider array of phonon transport phenomena. Such advancements include consideration of phonon dispersion [68], where the phonon frequencies have a nontrivial dependence on the wavevector. Studies have also shown the effects of optical phonons [69] and 1D solutions of the phonon BTE accounting for wavevectors throughout the anisotropic first Brillouin zone [45]. Additionally, a coupled LBM-Fourier approach has been used to perform multiscale thermal transport simulations where ballistic phonon effects at the small length scale are captured by LBM, while diffusive heat transport at the larger length scale is modeled using Fourier's law [11].

Presently, most methods appear to be based on the finite volume method [12, 34, 35, 38–40, 43, 70–73]. Borrowing concepts developed from the computational fluid dynamics community, finite volume approaches for solving the phonon BTE

have been developed for varying degrees of physical and numerical complexity. Early work involved numerical experiments of microscale semiconductor devices, such as field effect transistors [12, 34, 35, 40, 73], while subsequent studies considered a wider range of systems [38, 39, 43, 46, 48]. The finite volume method has been developed to better describe phonon transport through the incorporation of phonon dispersion, microscale anisotropy, and heterogeneous structures [12, 34, 39]. In addition to improving existing finite volume approaches to better capture phonon mechanisms, recent work has focused on improving the computational efficiency of the method through novel parallelization schemes and algorithm development [38, 39, 70, 72]. Due to the very large number of degrees of freedom, parallelization techniques are needed to reduce compute time. Ali et al. [38] found the most efficient parallelization speedup comes from a hybrid band/cell-based parallelization in which parallelization is applied to bands in conjunction with a parallel linear solver. For a hybrid band/cell-based parallelization, 88% parallel efficiency was achieved. Band parallelization in the context of the single-mode relaxation time approximation should have relatively little communication overhead and therefore should be highly scalable. Ni and Murthy [72] applied spatial decomposition parallelization and phonon band decomposition parallelization to solutions of the phonon BTE using both a full scattering as well as an SMRT model. They found that under the RTA model both parallelization techniques performed equally well, while spatial decomposition performed better for the full scattering model. We note that despite the numerous developments to the finite volume approach, the vast majority still use isotropic dispersion relations, neglecting full Brillouin zone effects.

In the next section we focus on numerical methods that primarily address the reciprocal space representation of phonons.

2.2.2.2 K-Space Representation

The reciprocal space representation is essentially the discretization over the domain of wavevectors. When the set of allowed wavevectors is finite, or the domain is naturally discrete, no discretization is necessary. However, when the phonons are in a continuous medium, then the number of allowed wavevectors is intractably large ($\sim 4.5 \times 10^{22}$ phonons/m³ [42]). Since a full copy of the real space discretized geometry is modeled at each allowed wavevector or phonon mode, this is clearly problematic. In this situation, a subset of wavevectors and their assignments into the real space may be sampled using the Monte Carlo technique.

Monte Carlo approaches simulate phonon packets corresponding to an ensemble of phonons that have the same frequency, direction of propagation, and spatial location. The solution of the phonon BTE occurs in two steps. First, the phonon packet propagates in an advection step in an Eulerian description. Then, a collisional step occurs in which the probability of scattering is drawn from an exponential distribution [42]. If the phonon packet is scattered, it is then destroyed and a new phonon packet is resampled from the frequency, angular, and polarization stochastic spaces. Monte Carlo methods have been developed to include more complex phonon physics, such as phonon dispersion [42], optical phonons [74], three dimensionality [36, 75], and fully anisotropic Brillouin zone properties [76].

Furthermore, algorithm developments have extended the capabilities of the Monte Carlo approach. Lacroix and co-workers defined a new distribution function so that sampling phonon-phonon collisions conserves energy without resampling events [77]. Péraud and Hadjiconstantinou developed the variance reduction formulation [36] to study thermal conductivity in porous nanostructures where the phonon distribution deviation from equilibrium is determined numerically, while the equilibrium distribution is known analytically. The variance-reduced approach allows for the resolution of small temperature fluctuations without increased computational cost.

The Monte Carlo approach may be desirable for multiple reasons [36]. For instance, resources may be used to exploit an "embarrassingly" parallel problem which means that many simulations may be performed simultaneously to enable use of the Central Limit Theorem and thereby reduce error. Furthermore, the resources conserved by sampling may be redistributed to deal with larger real space grids or more complex device geometries. Samples of the phonon population, in the form of phonon packets corresponding to an ensemble of phonons, are drawn from seven stochastic spaces representing frequency space, real space, angular space, and polarization space. The number of phonon packet samples used in the simulation is chosen based on the desired accuracy as well as computational limitations [42]. The error in the calculated phonon distribution function is proportional to the inverse of the square root of the number of samples. In their work, Majumdar and Mazumder simulated phonon transport in silicon thin films using $\sim 100,000$ phonon packets [42]

Stochastic methods based on Monte Carlo simulations have also been used to study phonon-mediated heat transfer in a wide array of systems including the

effect of boundary scattering on the temperature distributions in thin wires [32] and in thin films [33]. Shomali et al. [75] studied temperature fields in 3D transistors. Additionally, Pop et al. [78] performed coupled electron-phonon transport simulations, while Yang and Minnich [76] studied thermal transport across grain boundaries. Common among all of these efforts is the material studied contained a very large, potentially computationally intractable, number of phonon modes. Numerical approaches for solving the BTE are also important for the interpretation of experimental results. Using theoretical and experimental techniques, respectively, Chen [79] and Sverdrup et al. [8] found that the effective thermal conductivity at length scales commensurate to the phonon MFP is smaller than the bulk value. At such small length scales, carriers with larger MFP were essentially being suppressed. In recent years, this phenomenon has been exploited to probe MFP spectra of materials with the aid of computational BTE solutions. Experiments such as transient thermal grating (TTG), time domain thermoreflectance (TDTR), and broadband frequency domain thermoreflectance (BB-FDTR) quantify the modal contributions of different phonons to the thermal conductivity by inducing a temperature gradient at length scales comparable to the phonon MFP [80]. For temperature gradients that occur over lengths smaller than a phonon MFP, the relative contribution of that phonon mode to the thermal conductivity is suppressed. In order to quantify the degree to which this suppression occurs for a specific phonon mode, the BTE is solved numerically for the experimental geometry to determine the *suppression function* [81]. Once the suppression function is determined, it may be used to interpret experimental values of the effective thermal conductivity in order to reconstruct

the material dependent MFP spectrum [82]. The suppression function may also be used to characterize thermal conductivity reduction due to boundary scattering in nanostructures such as in thin wires and thin films [65].

In the final section of this chapter we discuss solution of the phonon BTE which retain the full-scattering expression.

2.2.2.3 Full Scattering BTE

The numerical approaches detailed thus far focused on the solution of the phonon BTE under some variant of a relaxation time approximation. The relaxation time is an empirical parameter that can be estimated numerically (see, for instance [83]) but must be determined outside of the BTE simulation. The steady-state zero-dimensional phonon BTE has been solved while retaining the full scattering terms [55]. Due to the nonlinearity of the full scattering BTE, the solution to equation 1.1 is most readily realized through an iterative approach wherein the phonon distribution function is updated in each iteration as a result of changes to all other distribution functions [56]. All studies that follow the iterative approach follow a roughly similar calculation procedure and set of assumptions. The full scattering BTE accounting for three-phonon processes is given by

$$\begin{aligned}
 -\mathbf{v}_\phi \cdot \nabla T \frac{\partial N_\phi}{\partial T} = \sum_{\phi' \phi''} \left\{ \left[N_\phi N_{\phi'} (1 + N_{\phi''}) - (1 + N_\phi) (1 + N_{\phi'}) N_{\phi''} \right] \Lambda_{\phi \phi' \phi''}^+ \right. \\
 \left. + \frac{1}{2} \left[N_\phi (1 + N_{\phi'}) (1 + N_{\phi''}) - (1 + N_\phi) N_{\phi'} N_{\phi''} \right] \Lambda_{\phi \phi' \phi''}^- \right\}
 \end{aligned}
 \tag{2.17}$$

The setup of the model is as follows. First, the phonon distribution is linearized with respect to frequency, this linearization comes from the assumption that the

phonon distribution deviation from equilibrium is small [53], namely

$$N_\phi = N_\phi^0 - \frac{\partial N_\phi^0}{\partial \omega_\phi} \Psi_\phi \quad (2.18)$$

where N_ϕ^0 is the equilibrium Bose-Einstein distribution, and Ψ_ϕ is the unknown deviation factor.

Next, it is assumed that there exists local equilibrium at each point in the material. Doing so admits the definition of a temperature T . The deviation factor of the distribution function from equilibrium is then rewritten under the assumption that it is proportional to the local temperature gradient, thus the deviation factor becomes

$$\Psi_\phi = \mathbf{F}_\phi \cdot \nabla T \quad (2.19)$$

where \mathbf{F}_ϕ is the solution vector of length n_{dim} (n_{dim} is the dimensionality of the system) that we are solving for in the iterative procedure. The deviation from equilibrium, Ψ_ϕ describes the perturbing effect of the temperature gradient on the phonon distribution function. Substituting Eq. 2.18 into Eq. 2.17 gives the linearized steady-state full scattering phonon BTE (accounting only for three-phonon scattering events)

$$-\mathbf{v}_\phi \cdot \nabla T \frac{\partial N_\phi^0}{\partial T} = \sum_{\phi'\phi''} \left[(\Psi_{\phi''} - \Psi_{\phi'} - \Psi_\phi) \Lambda_{\phi\phi'\phi''}^+ + \frac{1}{2} (\Psi_{\phi''} + \Psi_{\phi'} - \Psi_\phi) \Lambda_{\phi\phi'\phi''}^- \right] \quad (2.20)$$

where $\Lambda_{\phi\phi'\phi''}^\pm$ is the probability of phonon creation and annihilation events

$$\Lambda_{\phi\phi'\phi''}^\pm = \frac{\hbar V}{32\pi^2} \frac{N_\phi^0 (N_{\phi'}^0 + \frac{1}{2} \pm \frac{1}{2}) (N_{\phi''}^0 + 1)}{\omega_\phi \omega_{\phi'} \omega_{\phi''}} |\Phi_\pm(\phi, \phi', \phi'')|^2 \times \delta(\omega_\phi \pm \omega_{\phi'} - \omega_{\phi''}) \delta(\mathbf{k} \pm \mathbf{k}' - \mathbf{k}'' - \mathbf{G}) \quad (2.21)$$

Here, V represents the unit cell volume, while the delta functions enforce energy and quasi-momentum conservation. These probabilities, determined from quantum mechanical rules governing transitions between phonon states, are functions of the second and third-order force constants, $\Phi_{\pm}(\phi, \phi', \phi'')$. These force constants may be obtained, for instance, from the third-order derivatives of the potential energy function [84]. By plugging eq. 2.19 into eq. 2.20 and rearranging we obtain the expression

$$\begin{aligned} \mathbf{F}_{\phi} = & \frac{1}{\sum_{\phi'\phi''} (\Lambda_{\phi\phi'\phi''}^+ + \frac{1}{2}\Lambda_{\phi\phi'\phi''}^-)} \sum_{\phi'\phi''} \left[\Lambda_{\phi\phi'\phi''}^+ (\mathbf{F}_{\phi''} - \mathbf{F}_{\phi'}) + \frac{1}{2}\Lambda_{\phi\phi'\phi''}^- (\mathbf{F}_{\phi''} + \mathbf{F}_{\phi'}) \right] \\ & + \frac{1}{\sum_{\phi'\phi''} (\Lambda_{\phi\phi'\phi''}^+ + \frac{1}{2}\Lambda_{\phi\phi'\phi''}^-)} \mathbf{v}_{\phi} \frac{\partial N_{\phi}^0}{\partial T}. \end{aligned} \quad (2.22)$$

Equation 2.22 may now be solved via an iterative procedure where the values of \mathbf{F}_{ϕ} are initialized and then successively updated using prevailing values for $\mathbf{F}_{\phi'}$ and $\mathbf{F}_{\phi''}$ at each iteration step. A typical choice for the initialization is

$$\mathbf{F}_{\phi}^0 = \frac{1}{\sum_{\phi'\phi''} (\Lambda_{\phi\phi'\phi''}^+ + \frac{1}{2}\Lambda_{\phi\phi'\phi''}^-)} \mathbf{v}_{\phi} \frac{\partial N_{\phi}^0}{\partial T}. \quad (2.23)$$

Upon determining \mathbf{F}_{ϕ} , the thermal conductivity may be obtained. This procedure is based on a presumption of the thermal conductivity tensor as implemented in Fourier's law, relating to the flux of thermal phonon carriers as follows

$$\mathbf{q} = \sum_{\phi} \hbar\omega_{\phi} N_{\phi} \mathbf{v}_{\phi} = -\boldsymbol{\kappa} \nabla T \quad (2.24)$$

and substituting Eqs. 2.19 and 2.19 into Eq. 2.24 gives the expression [56]

$$\boldsymbol{\kappa} = - \sum_{\phi} \hbar\omega_{\phi} \frac{\hbar N_{\phi}^0 (N_{\phi}^0 + 1)}{k_B T} \mathbf{v}_{\phi} \otimes \mathbf{F}_{\phi}. \quad (2.25)$$

To date, generalized iterative approaches have been challenging to develop due to their relatively larger computational costs. The large computational cost is due both to the iterative process itself, but also the calculation of $\Lambda_{\phi\phi'\phi''}^{\pm}$ which requires extensive Brillouin zone mapping in order to calculate the three-phonon interactions that satisfy energy and pseudo-momentum conservation rules (see eq. 2.13). Calculations based on the iterative approach require *at least* an order of magnitude larger computing time than the RTA method [56]. Furthermore, studies thus far have restricted application of the iterative approach to simple crystals. In fact, Broido et al. observed that the computationally intensive task of calculating the energy and momentum conserving processes currently precludes the study of crystalline solids with complex unit cells [53]. The iterative approach was first applied to thermal conductivity in an isotropic solid [55] and extended to include anisotropy in rare-gas solids interacting through a simple pair potential [85]. Subsequent work applied the approach to diamond-type lattices [86], modified the interactions to include non-central forces [87], and applied the iterative approach to superlattices [54]. As the force constants are the only inputs for the iterative approach, it is vital that the model selected for the atomic interactions accurately captures harmonic and anharmonic forces. It was found that several common classical interatomic potentials fail to reproduce the true force constants and as a result these early studies obtained computational results for the thermal conductivity two to four times greater than experiment [88].

To remove this flaw, researchers calculated harmonic and anharmonic force constants from density functional theory (DFT), leading to a substantial increase

in accuracy of the method [53, 56, 89]. Thermal conductivities calculated from the iterative procedure using force constants obtained from DFT are highly accurate in comparison with experiments over a wide range of temperatures [53]. This approach has been used with good effect to calculate the thermal conductivity of Si and Ge [53], diamond [90], graphene [91], several compound conductors [89], and thermoelectric materials [92].

Finally, while the BTE solution techniques detailed in this section have been applied to a wide range of atomic crystals, literature on phonons in molecular crystals and other complex crystals remains relatively sparse. Energetic molecular crystals such as RDX, HMX, and TATB are commonly used explosives with industrial and defense application [22]. Phonon behavior within these materials is important to chemical initiation processes [21]. Previous attempts to model heat transport in energetic materials have used Fourier's heat law which is known to break down when temperature variations occur over distances smaller than the MFP. Kroonblawd and Sewell investigated the difference in the temperature distributions predicted by MD and Fourier simulations of nanoscale heat transport and found that for TATB the phonon MFP is sufficiently small ($<10 \text{ \AA}$) to conclude that continuum methods provide reasonable accuracy for thermal modeling [93]. However, due to the lack of available MFP data for energetic molecular crystals, open questions remain as to how phonons actually contribute to initiation [22]. A particular challenge is the sheer computational complexity of dealing with unit cells that can contain tens to over one hundred atoms [22, 94], making calculations of dispersion curves nontrivial. Nevertheless, progress continues to be made in improving the understanding of

phonon behaviors in complex materials. Recently, Long and Chen [95] developed a theoretical approach for determining phonon lifetimes in energetic complex crystals allowing for the calculation of the MFP that brings us closer to developing a more complete phonon model of energetics. In this dissertation we utilize the phonon BTE, for the first time, to investigate phonon behavior in the molecular crystal α RDX, providing insight into the mechanisms that lead to initiation in energetic materials.

In the next chapter we present our own solution method for the three dimensional full Brillouin zone phonon BTE. This solution method involves independent real *and* reciprocal space discretizations in order to capture the full range of anisotropic thermal carrier behavior present in novel three dimensional phonon systems.

Chapter 3: Methodology for Solution of Full Brillouin Zone Three Dimensional Phonon BTE ²

In chapter 2 we introduced the fundamentals of phonon theory and formed an intuition for phonon mediated microscale thermal transport. In addition we surveyed the landscape of numerical techniques for solution of the phonon BTE, detailing the strengths and weaknesses of the prevailing approaches as well as providing examples of microscale systems that were studied using the various numerical techniques. In this chapter a model and associated numerical method are presented for simulation of heat transport at the microscale via the solution of the three dimensional phonon BTE. In small domains, the full Brillouin zone has a finite number of vibrational modes, as determined by Born von-Karman boundary conditions, and therefore has a discrete representation. As a result of this discreteness, the present method allows for general crystal anisotropy, at the lattice-, micro-, and macro- scale, as well as finite dimensional effects that naturally permit anisotropic thermal transport and energy flow. The method is shown and verified using analytical solutions for isotropic

²Portions of this chapter appeared in the publication: *F. G. VanGessel, P. W. Chung, An anisotropic full Brillouin zone model for the three dimensional phonon Boltzmann transport equation. Comput. Methods Appl. Mech. Engrg. (2017), <http://dx.doi.org/10.1016/j.cma.2017.01.010>*

[30]

thermal flows.

3.1 History of BTE Methodology Developments

In systems with characteristic length scales on or below the phonon MFP, accurate thermal modeling requires methods that account for the discrete nature of the system, i.e. atomistic or quasi-continuum methods. Whereas the average MFP in crystalline silicon at ambient conditions is 300 nm [96], transistor devices made of silicon now have feature sizes < 50 nm [97]. At such length scales, thermal carriers are predominantly ballistic, i.e. boundary scattering processes dominate phonon-phonon scattering. Anisotropy at such small length scales can arise from three factors. The finite-sized device structure severely reduces the number of carriers in the system relative to a bulk crystal [98]. If the aspect ratio of the device is sufficiently large, the spacing of carriers in reciprocal space becomes highly non-uniform along different principal directions, leading to anisotropy in the thermal flow [99–101]. In addition, even macroscopically isotropic crystals, i.e. cubic crystals, produce non-radially symmetric dispersion surfaces (see Fig. 2.8) and group velocities which directionally bias thermal carriers [65, 99, 102]. The resulting anisotropy, termed microscale phonon anisotropy, in thermal flow is only present at the microscale whereas the flow reduces to isotropic at length scales where all carriers become diffusive. Finally, non-cubic crystal structures can lead to macroscopic anisotropy, such as in hexagonal close packed systems or layered systems such as graphite [103–105]. The different types of phonon anisotropy as well as the associated source of anisotropy,

system length scale at which the anisotropy arises, and quantifying metric of the anisotropy, are detailed in figure 3.1. Computational approaches applied to modeling phonon transport in microscale systems must therefore be capable of modeling discrete and anisotropic carriers in both the ballistic and diffusive transport regimes. Furthermore, these approaches must possess the capability to capture all three distinct sources of thermal carrier anisotropy. The phonon BTE is well-suited to this task. It is capable of accurately determining phonon transport in devices with dimensions on the order of a phonon MFP [51].

Improvements to existing phonon BTE modeling methodologies are required to handle the challenges presented by new device designs and constituent device materials that result in increasingly complex phonon behavior. Two primary drivers of increasing complexity of phonon transport within next generation solid-state devices are emergent three-dimensional device geometries, i.e. vertical transistors [106], and reduction of device dimensions [97]. Earlier computational studies were focused on planar structures, primarily directed towards horizontal devices [34, 40, 42, 66, 73] which could be treated as nominally two-dimensional systems. However, interior phonon flow within novel device geometries with complex features, such as phononic thin films and nanowires [107–109], is complicated by re-entrant corners leading to phenomena such as phonon backscattering and phonon trapping [110–112]. Therefore, accurate phonon modeling of emergent devices requires accounting for the three dimensional spatial variation of the phonon energy field. Furthermore, Recent studies have also found that anisotropic effects play an important role in heat flow in silicon nanomembranes and layered graphite thin films [45, 100, 103]. Current com-

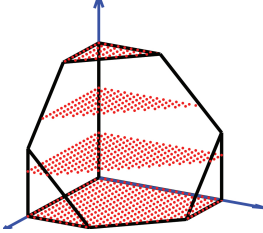
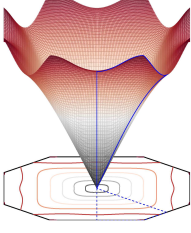
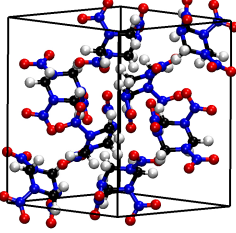
	Finite Lattice	Microscale	Macroscopic
			
Source:	Non-uniform wavevector distribution in Brillouin Zone	Brillouin zone anisotropy, $\omega(\mathbf{k}) \neq \omega(\mathbf{k})$	Non-cubic lattice structure ($a_i \neq a_j$)
Characteristic length scale (L_c) of system:	$L_c/a_i \sim \mathcal{O}(10)$ ($L_c < 100$ unit cells)	$L_c \lesssim \max \Lambda_\phi$ (ballistic transport)	anisotropy present for any L_c
Quantifying metric:	κ	$H_{\hat{d}}$	κ

Figure 3.1: The three types (finite lattice, microscale, and macroscopic) of phonon anisotropy. Associated with each type of anisotropy is the source, characteristic system length scale, as well as quantifying metric. The source of the phonon anisotropy indicates the underlying cause. The characteristic system length scale indicates the system dimensions for which the anisotropy produces non-negligible effects on phonon flow. The quantifying metric indicates the method for quantifying the degree, and directionality, of the anisotropy (either thermal conductivity, κ , calculated via the phonon gas model as defined in eq. 6.1, or phonon radiosity defined in eq. 4.3).

putational approaches appear to employ assumptions that do not make it obvious how they should be extended to consider all three types of anisotropic mechanisms. Notably, the majority of established methods employ an isotropic assumption where phonon behavior along a single high symmetry line of the Brillouin zone is taken to model the phonon properties in all directions [36, 38, 39]. This radially symmetric model of the Brillouin zone necessarily produces a diagonal conductivity tensor with equal terms. It cannot consider situations encountered in general anisotropic thermal flows due to one, or several, sources of anisotropy where the conductivity tensor has non-zero off-diagonal terms or non-equal terms along the diagonal, or both.

Early computational approaches for solving the phonon BTE were directed towards study of solids composed of group-IV chemical elements whose bonds are generally tetrahedrally-coordinated. Owing to this symmetry, the macroscopic thermal conductivity is isotropic. Thus the first computational methods assumed that phonon frequencies were radially symmetric, usually based on the frequencies in a high symmetry direction as described earlier, and therefore exhibit isotropy in their flows. For instance, Mazumder and Majumdar developed a Monte Carlo (MC) solution method for the two dimensional phonon BTE, which accounted for dispersion and multiple acoustic branches along a single direction in the Brillouin zone [42]. The method was used to determine thermal conductivity values in thin silicon films which were found to agree well with experimental values. Narumanchi et. al. developed a control volume method for the solution of the two dimensional isotropic phonon BTE [73] and similarly found good agreement in conductivity values with

experimental results for a range of film widths and dopant levels in silicon. Ali and Mazumder developed a technique for the solution of the three dimensional isotropic phonon BTE in a heterogeneous material which accounted for material interfaces [39]. Their model incorporated phonon scattering at material interfaces as well as variation in the dispersion relations in the two materials.

In transport of energy in finite dimensional structures of sufficiently small dimensions, the discreteness and truncation of the lattice leads to discreteness of carriers and, for large aspect ratios, anisotropic thermal flows. A general cubic crystal therefore should exhibit anisotropy in small device structures, namely in the ballistic regime, but isotropy at large scales in the diffusive regime [113]. Ni and Murthy accounted for the microscale anisotropy of phonon properties in a continuous representation of the Brillouin zone BTE [34]. These anisotropic features allowed them to also model anisotropic phonon scattering through directionally-dependent relaxation times. While anisotropy arising from non-radially symmetric dispersion surfaces could certainly be modeled through this approach, a continuous Brillouin zone largely confines that consideration to microscale and macroscopic anisotropy. It is not immediately apparent how such a continuous Brillouin zone representation could be used to capture anisotropy arising from finite dimensional effects.

In the remainder of this chapter, a method is presented for three dimensional solutions to the phonon BTE with explicit consideration for the physically allowed phonon modes in finite dimensional structures. Despite the numerous available BTE solvers and descriptions of solution methods, there remains remarkably few if any computer methods that have been described. Our goal is to investigate the role

of various sources of anisotropy on thermal transport and draw conclusions about the effects. The physically allowed phonon modes are determined from the system dimensions using Born von-Karman boundary conditions. The method is described in sec. 3.3 and then verified in sec. 3.4 using an emulated isotropic Brillouin zone that is compared with an analytical radiative transport solution.

3.2 Problem Definition

3.2.1 Material Domain

Consider a domain, Ω , with boundary Γ shown in Fig. 3.2. The side lengths of the domain are L_1, L_2 , and L_3 . The domain is composed of a crystalline ma-

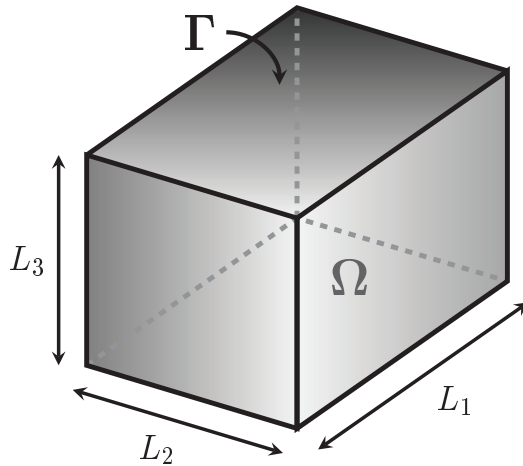


Figure 3.2: Domain Ω with boundary Γ

terial with primitive lattice vectors $\{\mathbf{a}_1, \mathbf{a}_2, \mathbf{a}_3\}$ and atomic basis $\mathbb{B} = \{\mathbf{b}_r | r \in (1, 2, \dots, p)\}$ composed of p atoms, where $\mathbf{a}_i \in \mathbb{R}^3$ and $\mathbf{b}_r \in \mathbb{R}^3$ for $i \in \{1, 2, 3\}$ and $r \in \{1, 2, \dots, p\}$. Figure 3.3 depicts a three dimensional crystal with a three

atom basis.

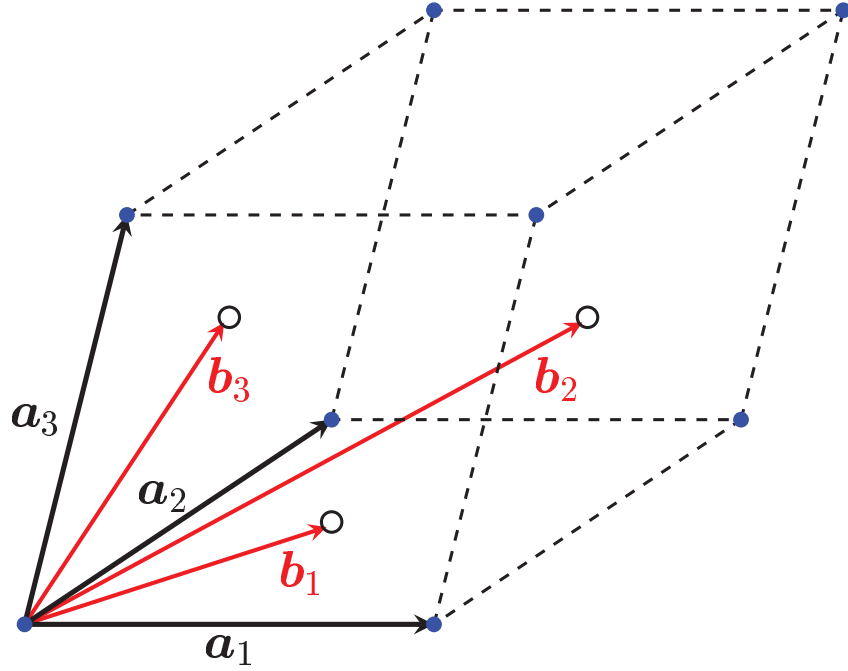


Figure 3.3: A crystal lattice with lattice points as blue dots, primitive lattice vectors $\{\mathbf{a}_1, \mathbf{a}_2, \mathbf{a}_3\}$, and three-atom basis $\{\mathbf{b}_1, \mathbf{b}_2, \mathbf{b}_3\}$.

Let $\{\hat{\mathbf{e}}_1, \hat{\mathbf{e}}_2, \hat{\mathbf{e}}_3\}$ be the unit vectors in the direction of \mathbf{a}_i . The set of lattice points inside Ω is

$$\mathbb{L} = \{n_1\mathbf{a}_1 + n_2\mathbf{a}_2 + n_3\mathbf{a}_3 \mid n_i \in (0, 1, \dots, N_i), i = 1, 2, 3\} \quad (3.1)$$

Where a lattice point $\mathbf{L}_\mathbf{n} \in \mathbb{L}$ indexed by $\mathbf{n} = (n_1, n_2, n_3)$, $\mathbf{n} \in \mathbb{Z}^3$, satisfies the condition $\mathbf{L}_\mathbf{n} \cdot \hat{\mathbf{e}}_i \leq L_i$, i.e. all allowed lattice points fall within Ω . The maximum index values, (N_1, N_2, N_3) , for a lattice point lying within Ω are obtained by solving

the linear system

$$\begin{bmatrix} N_1 \\ N_2 \\ N_3 \end{bmatrix} = \begin{bmatrix} \mathbf{a}_1 \cdot \hat{\mathbf{e}}_1 & \mathbf{a}_2 \cdot \hat{\mathbf{e}}_1 & \mathbf{a}_3 \cdot \hat{\mathbf{e}}_1 \\ \mathbf{a}_1 \cdot \hat{\mathbf{e}}_2 & \mathbf{a}_2 \cdot \hat{\mathbf{e}}_2 & \mathbf{a}_3 \cdot \hat{\mathbf{e}}_2 \\ \mathbf{a}_1 \cdot \hat{\mathbf{e}}_3 & \mathbf{a}_2 \cdot \hat{\mathbf{e}}_3 & \mathbf{a}_3 \cdot \hat{\mathbf{e}}_3 \end{bmatrix}^{-1} \begin{bmatrix} L_1 \\ L_2 \\ L_3 \end{bmatrix} \quad [x] = \max\{n \in \mathbb{Z} | n < x\} \quad (3.2)$$

Clearly, when the primitive lattice vectors are orthogonal such as in an orthorhombic crystalline systems, the matrix is diagonal.

3.2.2 Born von-Karman Boundary Conditions

Born von-Karman (BvK) boundary conditions are used to handle the finite size of the domain. Born von-Karman boundary conditions result in discrete vibrational modes where in the limit as the crystal becomes infinite, the allowed modes become continuous. The BvK conditions depend on the physical dimensions of the domain and the crystalline material composing the domain. Associated with the real space Bravais lattice, \mathbb{L} , is a reciprocal space lattice, $\mathcal{R} \subset \mathbb{R}^3$ and Brillouin zone, $\mathbb{BZ} \subset \mathbb{R}^3$. The reciprocal space lattice vectors are related to real space lattice vectors through

$$\mathbf{b}_i = 2\pi \frac{\mathbf{a}_j \times \mathbf{a}_k}{|\mathbf{a}_i \cdot (\mathbf{a}_j \times \mathbf{a}_k)|}. \quad (3.3)$$

Due to the periodicity of the lattice, the reciprocal lattice is also periodic and is given by

$$\mathcal{R} = \{l_1 \mathbf{b}_1 + l_2 \mathbf{b}_2 + l_3 \mathbf{b}_3 \mid l_i \in \mathbb{Z}, i = 1, 2, 3\}. \quad (3.4)$$

with a unit cell given by the *first Brillouin zone*. The first Brillouin zone is constructed by perpendicularly bisecting all lines connecting the origin of reciprocal

space to all other reciprocal lattice points. The bisecting planes then create a volume in reciprocal space enclosing the origin, this volume corresponds to the first Brillouin zone. Equivalently, the first Brillouin zone can be taken to be the locus of points lying closer to the origin than all other lattice points, i.e. the Voronoi cell surrounding the origin. Points lying outside the Brillouin zone may be mapped to a unique point within the Brillouin zone through the addition of a linear combination of reciprocal lattice vectors. In an infinite crystal, the Brillouin zone likewise contains an infinite number of points. However, for a crystal of a finite number of lattice points, there exist a finite set of discrete points corresponding to wavevectors (i.e. vibrational modes) in the Brillouin zone. These wavevectors, represented as \mathbf{k} , we will refer to as kpoints.

The atomic motion may be decomposed into vibrational waves in an atomic lattice whose corresponding atomic displacement for the r^{th} basis atom in the \mathbf{n}^{th} unit cell, is given by [50]

$$\mathbf{u}_{nr}(t) = \frac{1}{\sqrt{m_r}} \sum_{\phi} \mathbf{U}_{\phi r} e^{i(\mathbf{k} \cdot \mathbf{L}_n - \omega_{\phi} t)}. \quad (3.5)$$

Here \mathbf{u} is the atomic displacement from the equilibrium position, m_r is the mass of atom r , the sum ranges over all phonon modes ϕ , \mathbf{U} is the vibrational mode polarization vector, \mathbf{L}_n is the lattice point of cell \mathbf{n} , ω_{ϕ} is the vibrational frequency associated with mode ϕ , and t is time. Finally \mathbf{k} represents the wavevector associated with phonon mode ϕ .

The discrete nature of the allowed wavevectors, arising from the Born von-

Karman boundary conditions, originates from the requirement that

$$\mathbf{u}_{\mathbf{n},r}(t) = \mathbf{u}_{\mathbf{n}+\mathbf{G},r}(t) \quad (3.6)$$

$$\mathbf{G} = N_1 \mathbf{a}_1 + N_2 \mathbf{a}_2 + N_3 \mathbf{a}_3$$

Combining Eqs. 3.5 and 3.6 leads to the condition

$$e^{i\mathbf{k}\cdot\mathbf{L}\mathbf{n}} = e^{i\mathbf{k}\cdot(\mathbf{L}\mathbf{n}+\mathbf{G})} \implies e^{i\mathbf{k}\cdot\mathbf{G}} = 1 \quad (3.7)$$

this means that the size of Ω limits the allowed vibrational modes, \mathbf{k} , that can exist within the material. To satisfy Eq. 3.7, the argument to the exponential must be an integer multiple of 2π . Noting that $\mathbf{k} = k_1 \mathbf{b}_1 + k_2 \mathbf{b}_2 + k_3 \mathbf{b}_3$, and using the relation $\mathbf{a}_i \cdot \mathbf{b}_j = 2\pi \delta_{ij}$ leads to

$$\mathbf{k} \cdot \mathbf{G} = 2\pi N_1 k_1 + 2\pi N_2 k_2 + 2\pi N_3 k_3 . \quad (3.8)$$

Thus the components of \mathbf{k} must satisfy the relation

$$k_i = \frac{p_i}{N_i} \quad ; \quad p_i \in \mathbb{Z} \quad (3.9)$$

Therefore, we define the set of all physically allowed wavevectors, K , as

$$K = \left\{ \mathbf{k} : k_i = \frac{p_i}{N_i}, p_i \in \mathbb{Z} \forall i \in \{1, 2, 3\} \text{ and } \mathbf{k} \in \mathbb{B}\mathbb{Z} \right\} \quad (3.10)$$

In the limit as N_i becomes infinite, the distance between neighboring kpoints becomes zero. Thus, in phonon models of macroscale crystals it can usually be assumed that wavevectors are continuous variables. However, at the microscale finite-dimensional systems clearly have a discrete set of kpoints.

In addition, at each kpoint there exist a number of *branches* equivalent to three times the number of atoms in the basis (i.e. p). The set of all branches is denoted

$$\Lambda = \{ \lambda \mid \lambda \in (1, 2, \dots, 3p) \} . \quad (3.11)$$

Therefore the vibrational or phonon modes belong to the finite set

$$\Phi = K \times \Lambda = \{\phi = (\mathbf{k}, \lambda) \mid \mathbf{k} \in K, \lambda \in \Lambda\} . \quad (3.12)$$

In order to model thermal flow at the microscale within a crystalline material, the phonon Boltzmann transport equations must be discretized and solved for all physically allowed phonon modes, ϕ , in Φ .

3.2.3 Phonon Boltzmann Transport Equation

The general form of the phonon BTE is written

$$\frac{\partial N_\phi}{\partial t} + \mathbf{v}_\phi \cdot \nabla N_\phi = \left[\frac{\partial N_\phi}{\partial t} \right]_{\text{collision}} ; \quad \phi \in \Phi \quad (3.13)$$

where $\mathbf{v}_\phi \in \mathbb{R}^3$ and $N_\phi : \mathbb{R}^3 \rightarrow \mathbb{R}$. The discretization method can be applied equally to time dependent and steady state forms of the BTE. The time dependent term can be handled using, for instance, the generalized alpha family [114]. For the sake of simplicity we focus on the steady state form and neglect the time derivative term on the left hand side.

The collisional term in Eq. 3.13 can be considered using a multitude of approaches of varying degrees of physical approximation [50] including methods that permit the consideration of anisotropy in scattering [34]. The full-scattering expression is a complex non-linear function of the occupation numbers for all phonon modes [115]. However, for systems relatively close to equilibrium the scattering expression may be reduced to a linear form known as the relaxation time approxi-

mation (RTA) [50]. Thus we may write the phonon BTE as

$$\mathbf{v}_\phi \cdot \nabla N_\phi = \frac{N_\phi^0 - N_\phi}{\tau_\phi} \quad ; \quad \phi \in \Phi . \quad (3.14)$$

where \mathbf{v}_ϕ represents the phonon group velocity, τ_ϕ is the relaxation time, N_ϕ^0 is the equilibrium occupation of the phonon mode, and N_ϕ is the unknown occupation of the phonon mode. The occupation of a phonon mode represents the number of energy quanta, or phonons, in that mode. The equilibrium occupation is determined through Bose-Einstein statistics, whose associated phonon distribution is represented by the expression

$$N_\phi^0(\mathbf{r}) = \left[\exp \left(\frac{\hbar\omega_\phi}{k_b T(\mathbf{r})} \right) - 1 \right]^{-1} \quad (3.15)$$

where \hbar is Planck's reduced constant, k_b is the Boltzmann constant, and T is the temperature. Thus the right hand side contribution in Eq. 3.14 is non-zero in the presence of a nonequilibrium distribution of phonons.

Following [73], we choose to formulate the phonon BTE in terms of energy. The energy form is obtained by multiplying through Eq. 3.14 by $\hbar\omega_\phi$, neglecting the ground state energy, and including a phonon generation term, S_ϕ , the energy form of the BTE is obtained for a given mode ϕ ,

$$\mathbf{v}_\phi \cdot \nabla e_\phi = \frac{e_\phi^0 - e_\phi}{\tau_\phi} + S_\phi \quad ; \quad \phi \in \Phi . \quad (3.16)$$

Here $e_\phi = \hbar\omega_\phi N_\phi$ and $e_\phi^0 = \hbar\omega_\phi N_\phi^0$.

The problem of phonon transport may now be stated. Consider a finite domain in real space denoted by $\Omega \in \mathbb{R}^3$, with a boundary $\Gamma \in \mathbb{R}^2$. Γ may be further

partitioned into Γ^t , Γ^d , Γ^s , and Γ^p denoting regions with applied temperature, diffuse, specular, and periodic Dirichlet boundary conditions respectively. Associated with this domain is a discrete set, Φ , of allowed phonon modes which may exist within the crystalline material that constitutes Ω , a single mode is denoted ϕ . Find the energy density function $e_\phi : \mathbb{R}^3 \rightarrow \mathbb{R}$ such that

$$\begin{aligned}
\mathbf{v}_\phi \cdot \nabla e_\phi(\mathbf{r}) &= \frac{e_\phi^0(\mathbf{r}) - e_\phi(\mathbf{r})}{\tau_\phi} + S_\phi(\mathbf{r}) & \text{for } \mathbf{r} \in \Omega \\
e_\phi(\mathbf{r}) &= e_\phi^t(\mathbf{r}) & \text{for } \mathbf{r} \in \Gamma^t \\
e_\phi(\mathbf{r}) &= e_\phi^d(\mathbf{r}) & \text{for } \mathbf{r} \in \Gamma^d \quad ; \quad \forall \phi \in \Phi \\
e_\phi(\mathbf{r}) &= e_\phi^s(\mathbf{r}) & \text{for } \mathbf{r} \in \Gamma^s \\
e_\phi(\mathbf{r}) &= e_\phi^p(\mathbf{r}) & \text{for } \mathbf{r} \in \Gamma^p
\end{aligned}$$

3.3 Methodology

This section describes the computational method in two parts. The first portion covers the discretization of the phonon Boltzmann transport equation. The second portion involves the determination of the thermal transport properties of the phonon modes, where the modes are limited to the set, Φ , of those physically permitted in accordance with the Born von-Karman boundary conditions. Figure 3.4 illustrates the methodology structure. Phonon-phonon scattering is handled through an equilibrium temperature bath that serves as the driver for returning non-equilibrium phonon modes back to Bose-Einstein statistics.

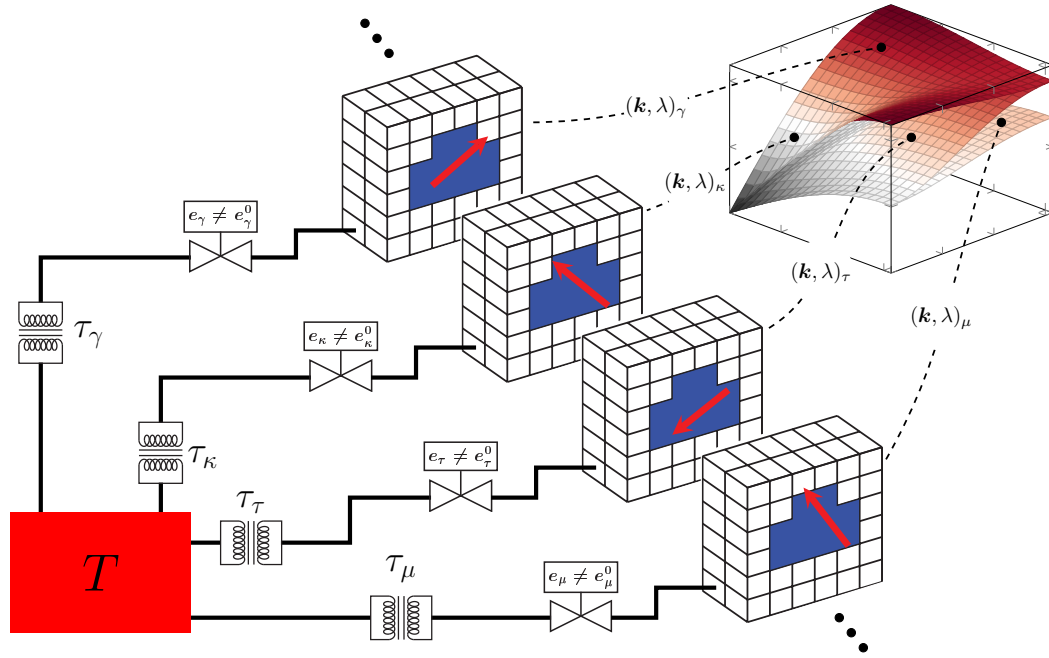


Figure 3.4: The BTE is solved for the complete set of phonon modes ($\dots, \gamma, \kappa, \tau, \mu, \dots$) as determined by Born von-Karman boundary conditions. The domain on which each mode resides is discretized and solved on copies of the same spatial grid. The advection properties of each mode are determined from the group velocity (red arrows). The coupling between phonon modes occurs through the RTA which models phonon-phonon scattering by relaxing each mode to an equilibrium thermal bath corresponding to the total system energy (red rectangle). Energy is transferred to and from each mode when the mode deviates from the equilibrium Bose-Einstein statistical distribution. The coupling strength of each mode to the thermal bath is determined by the mode relaxation time τ .

3.3.1 Discretization

For real materials, or in all but the simplest geometries, e_ϕ cannot be determined by solving Eq. 3.14 analytically. We therefore discretize using the control volume method [116] which was also employed in [39,40,73]. Solutions to the governing equations are determined at grid points which are located at both volume and surface centroids. The spatial discretization involves partitioning Ω and Γ into discrete volumes and facets. Ω is partitioned into N_Ω non-overlapping polyhedral control volumes, where the i^{th} control volume is denoted by Ω_i . Therefore $\Omega = \bigcup_{i \in \{1,2,\dots,N_\Omega\}} \Omega_i$. The boundary of Ω_i is denoted by $\partial\Omega_i$. The control volume boundary is comprised of m facets, each labeled as $\partial\Omega_{if}$, where $\partial\Omega_i = \bigcup_{f \in \{1,2,\dots,m\}} \partial\Omega_{if}$, where for a brick-shaped control volume, $m = 6$. Each facet has an associated constant normal vector $\hat{\mathbf{n}}_{if}$. Gradients or fluxes are then defined on facets and boundary conditions are imposed through control points in facets that intersect the domain surface, Γ .

The domain boundary, Γ is partitioned into N_Γ non-overlapping control areas, where $\Gamma = \bigcup_{l \in \{1,2,\dots,N_\Gamma\}} \Gamma_l$. Associated with each control area is the outward-directed normal vector $\hat{\mathbf{n}}_l$. Hereafter i and j are indices for control volumes, while l is the index for control areas. The union of all bulk control volumes and the boundary control areas forms the spatial grid discretizing the entire domain, $\Omega \cup \Gamma$. The boundary mesh and the bulk domain grid are conforming. The discretized domain is depicted in Fig. 3.3.1. We express the conservation of energy of mode ϕ in each control volume by integrating Eq. 3.16, for phonon mode ϕ , over the control volume

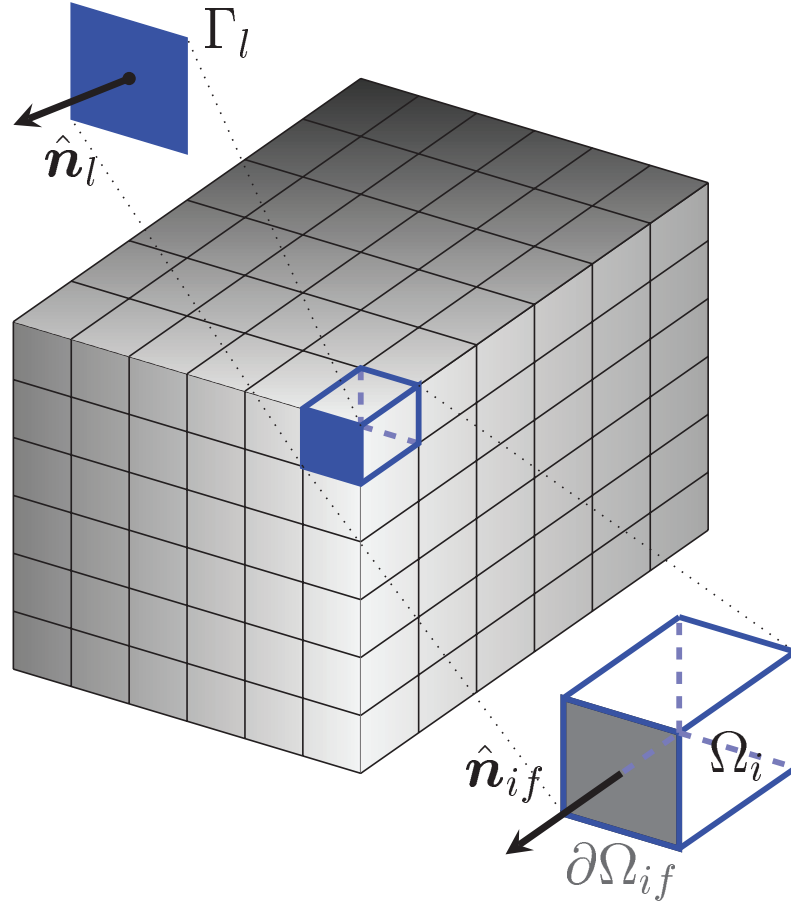


Figure 3.5: Domain Ω discretized into control volumes. A single control volume, Ω_i , is depicted along with a surface facet, $\partial\Omega_{i,f}$, and the associated normal vector, $\hat{\mathbf{n}}_{i,f}$. Additionally the boundary control area that Ω_i intersects, Γ_l , is shown along with the associated normal vector $\hat{\mathbf{n}}_l$

Ω_i ,

$$\int_{\Omega_i} \mathbf{v}_\phi \cdot \nabla e_\phi(\mathbf{r}) d\mathbf{r} = \int_{\Omega_i} \frac{1}{\tau_\phi} [e_\phi^0(\mathbf{r}) - e_\phi(\mathbf{r})] d\mathbf{r} + \int_{\Omega_i} S_\phi(\mathbf{r}) d\mathbf{r} . \quad (3.17)$$

Following the control volume method [116], let us assume that the e_ϕ and e_ϕ^0 are

constant over the control volume, this allows Eq. 3.17 to be written in the form

$$\int_{\Omega_i} \mathbf{v}_\phi \cdot \nabla e_\phi(\mathbf{r}) d\mathbf{r} = \frac{1}{\tau_\phi} [e_{\phi i}^0 - e_{\phi i}] \Omega_i + S_{\phi i} \Omega_i. \quad (3.18)$$

Applying the Gauss divergence theorem to the term on the left hand side of Eq. 3.18, the following expression is obtained

$$\int_{\partial\Omega_i} \mathbf{v}_\phi \cdot e_\phi(\mathbf{r}) \hat{\mathbf{n}} dS \quad (3.19)$$

where now integration is over the surface of the cell, $\partial\Omega_i$, and $\hat{\mathbf{n}}$ is the outward-facing normal to the boundary. Divide the surface integral into individual integrals over the m facets of $\partial\Omega_i$, where over each facet both the facet normal, $\hat{\mathbf{n}}_{if}$, and the facet energy density, $e_{\phi f}$, are taken to be constant. Under this assumption Eq. 3.19 becomes

$$\sum_{f=1}^m A_f e_{\phi f} \mathbf{v}_\phi \cdot \hat{\mathbf{n}}_{if} \quad (3.20)$$

where A_f is the area of the f^{th} facet. In order to resolve the value of $e_{\phi f}$, the first order upwinding approximation is applied, following [116] this is written as

$$e_{\phi f} = \frac{\max(\mathbf{v}_\phi \cdot \hat{\mathbf{n}}_f, 0)}{|\mathbf{v}_\phi \cdot \hat{\mathbf{n}}_f|} e_{\phi i} + \frac{\max(-\mathbf{v}_\phi \cdot \hat{\mathbf{n}}_f, 0)}{|\mathbf{v}_\phi \cdot \hat{\mathbf{n}}_f|} e_{\phi j} \quad (3.21)$$

where f is the facet that is shared by control volumes i and j .

Then combining Eqs. 3.18, 3.20, and 3.21, yields

$$\begin{aligned} & \sum_{f=1}^m A_f \left[\frac{\max(\mathbf{v}_\phi \cdot \hat{\mathbf{n}}_f, 0)}{|\mathbf{v}_\phi \cdot \hat{\mathbf{n}}_f|} e_{\phi i} + \frac{\max(-\mathbf{v}_\phi \cdot \hat{\mathbf{n}}_f, 0)}{|\mathbf{v}_\phi \cdot \hat{\mathbf{n}}_f|} e_{\phi j} \right] \mathbf{v}_\phi \cdot \hat{\mathbf{n}}_f \\ &= \frac{1}{\tau_\phi} [e_{\phi i}^0 - e_{\phi i}] \Omega_i + S_{\phi i} \Omega_i. \end{aligned} \quad (3.22)$$

Equation 3.22 describes the energy balance for the ϕ^{th} phonon mode in the i^{th} control volume. It indicates that the energy leaving through the facets should be balanced by

the energy entering the phonon mode through phonon scattering, modeled through the relaxation time, or due to phonon generation within the control volume. The values of the phonon energy densities at the facets are expressed in terms of the cell centered values e_ϕ due to the upwinding approximation. Equation 3.22 represents a balance equation for the i^{th} control volume. Assembling the balance equations for all control volumes and control areas results in a system of linear equations. The approach for treating the effect of boundary conditions, and determination of phonon energy density values at the control area face centers, will be detailed in Sec. 3.3.3. The final step in the discretization is to recast the linear system into matrix form, $[K_\phi]\{e_\phi\} = \{f_\phi\}$, where $[K_\phi] \in \mathbb{R}^{(N_\Omega+N_\Gamma) \times (N_\Omega+N_\Gamma)}$ and $\{f_\phi\} \in \mathbb{R}^{(N_\Omega+N_\Gamma)}$ whose terms can be shown to be

$$[K_\phi]_{\alpha\beta} = \begin{cases} \frac{1}{\tau_\phi}\Omega_\alpha + \sum_{f=1}^m A_f \frac{\max(\mathbf{v}_\phi \cdot \hat{\mathbf{n}}_f, 0)}{|\mathbf{v}_\phi \cdot \hat{\mathbf{n}}_f|} \mathbf{v}_\phi \cdot \hat{\mathbf{n}}_f & \alpha = \beta \\ A_f \frac{\max(-\mathbf{v}_\phi \cdot \hat{\mathbf{n}}_f, 0)}{|\mathbf{v}_\phi \cdot \hat{\mathbf{n}}_f|} \mathbf{v}_\phi \cdot \hat{\mathbf{n}}_f & \alpha \neq \beta \\ 1 & \alpha = \beta \\ 0 & \alpha \neq \beta \end{cases} \begin{matrix} ; \Omega_\alpha \in \Omega \\ \\ \\ ; \Gamma_\alpha \in \Gamma \end{matrix} \quad (3.23)$$

and

$$\{f_\phi\}_\alpha = \begin{cases} \frac{1}{\tau_\phi}\Omega_\alpha e_{\phi\alpha}^0 + S_{\phi\alpha}\Omega_\alpha & ; \Omega_\alpha \in \Omega \\ e_{\phi\alpha} & ; \Gamma_\alpha \in \Gamma \end{cases} \quad (3.24)$$

here $\alpha, \beta \in \{1, 2, \dots, N_\Omega + N_\Gamma\}$. Recasting the linear system in matrix form allows one to make use of the plethora of highly efficient linear system numerical solvers. Solving the linear system yields the cell-centered phonon mode energy densities, $e_\phi \in \mathbb{R}^{(N_\Omega+N_\Gamma)}$. This is repeated for all phonon modes in Φ . The total cell centered energy

density within each control volume may then be computed via the summation,

$$e_i = \sum_{\phi \in \Phi} e_{\phi i} \quad \text{for all} \quad \Omega_i \in \Omega . \quad (3.25)$$

Once the energy field has been obtained the temperature field is determined through thermodynamic relations involving the specific heat.

3.3.2 Specific Heat

Often the quantity of interest in thermal transport simulations is the material temperature rather than the energy or energy density. To convert the energy density field to a temperature field, the specific heat is used. The volumetric specific heat is a thermodynamic quantity relating energy to temperature change, and is defined as

$$C = \left. \frac{\partial U}{\partial T} \right|_V \quad (3.26)$$

where U is the internal energy density and the derivative is taken at constant volume. The contribution to the volumetric specific heat from a single mode may be written as [98]

$$C_\phi = \frac{\partial e_\phi}{\partial T} \quad (3.27)$$

where for the microscale heat transfer problems considered here it is assumed the material remains at constant volume. Temperature as a thermodynamic quantity is only defined in equilibrium [73], therefore the phonon mode energy density in Eq. 3.27 may be replaced by the equilibrium value, e_ϕ^0 . Since the temperature dependence of the phonon mode energy at equilibrium is known to be

$e_\phi^0 = \hbar\omega_\phi \left[\exp\left(\frac{\hbar\omega_\phi}{k_b T}\right) - 1 \right]^{-1}$, the analytical form of the mode-wise specific heat follows from Eq. 3.27,

$$C_\phi = \frac{1}{V} \frac{(\hbar\omega_\phi)^2}{k_b T^2} \frac{e^{\frac{\hbar\omega_\phi}{k_b T}}}{\left[e^{\frac{\hbar\omega_\phi}{k_b T}} - 1 \right]^2} \quad (3.28)$$

where V is the volume of the crystal. Equation 3.28 is a fully quantum mechanical expression in that it is a result of Bose-Einstein statistics.

The total specific heat of the crystalline material is determined by summing all mode contributions,

$$C = \sum_{\phi \in \Phi} C_\phi . \quad (3.29)$$

Equation 3.28 indicates that the specific heat is a function of temperature, however for temperature ranges of interest in this work the specific heat will be assumed to take on a constant value at some reference temperature T_{ref} . The choice of T_{ref} is non-unique, where a sensible choice could be an average of the prescribed temperature Fourier boundary condition (see Sec. 3.3.3), therefore $C(T) = C(T_{ref})$.

The assumption of constant specific heat allows for a simple relationship between energy and temperature by combining Eqs 3.25 and 3.27 in Eq. 3.29, yielding

$$e = C (T - T_{ref}) . \quad (3.30)$$

Note that the energy density obtained in this manner corresponds to the difference between the system energy density at temperature T and the system energy density at temperature T_{ref} . Temperature as a thermodynamic quantity is not well defined on length scales below the phonon mean free path [3]. However, following [73] a temperature as defined in Eq. 3.30 will be used throughout the simulation. The

temperature defined in this way corresponds to a measure of energy within the system [73].

Finally, note that Eq. 3.24 may be rewritten using Eqs. 3.28, 3.29, and 3.30 to give

$$\{f_\phi\}_i = \frac{1}{\tau_\phi} \Omega_i C_\phi (T_i - T_{ref}) + S_{\phi,i} \Omega_i . \quad (3.31)$$

3.3.3 Boundary Conditions

Phonons are confined to the crystalline lattice and therefore scatter at material boundaries. Each control area may be assigned a different type of boundary scattering. The four types of boundary conditions considered presently are: prescribed temperature condition, specular scattering, diffuse scattering, and periodic boundary condition (note that this periodic boundary condition is fundamentally different than Born von-Karman boundary conditions). At the boundary, only phonon modes propagating into the domain, i.e. phonon mode ϕ such that $\mathbf{v}_\phi \cdot \hat{\mathbf{n}}_l < 0$, have an applied boundary condition. Modes leaving through the boundary have no effect on the solution variables, $e_{\phi i}$.

3.3.3.1 Applied Temperature Condition

Following [40], the applied temperature condition assumes blackbody behavior at the boundary, where phonons propagating out of the domain are perfectly absorbed by the boundary. Conversely, phonon modes propagating into the domain are assumed to be in equilibrium, as determined by Bose-Einstein statistics,

at the applied temperature. The applied temperature condition at control area Γ_l is expressed as

$$e_{\phi l} = C_{\phi}(T_l - T_{ref}) \quad ; \quad \mathbf{v}_{\phi} \cdot \hat{\mathbf{n}}_l < 0 \quad (3.32)$$

where $\hat{\mathbf{n}}_l$ is the boundary outward facing normal and T_l is the prescribed temperature at the control area facet which intersects with the applied temperature boundary, i.e. $\Gamma_l \subseteq \Gamma^t$. Note that this boundary condition allows for a non-zero net flux through the boundary. The applied temperature condition prescribes the value of $e_{\phi l}$ for all facets that intersect Γ^t .

3.3.3.2 Specular Scattering Condition

At specular boundaries, phonons undergo reflection such that the component of the phonon group velocity tangential to the boundary remains unchanged. The process is depicted in Fig. 3.6. Specular reflection models either phonon reflection

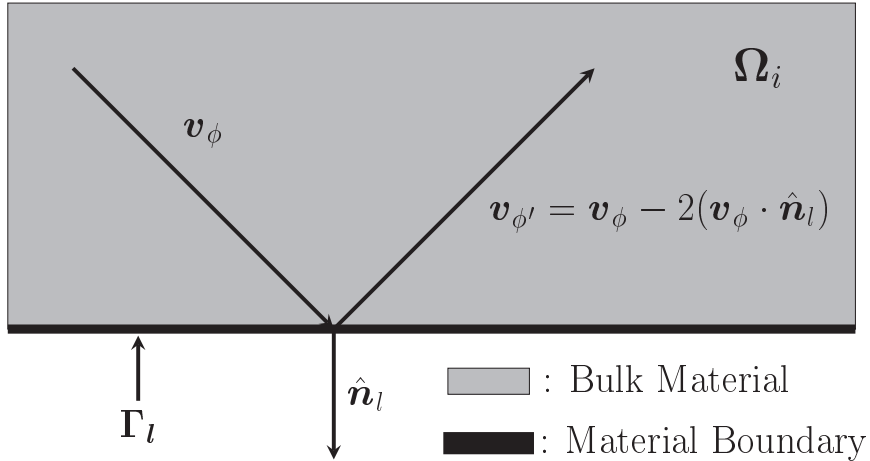


Figure 3.6: Phonon wavepacket undergoing specular reflection

at crystal boundaries that are highly ordered, or a symmetry plane in the domain.

The condition is expressed as

$$e_{\phi l} = e_{\phi i} \quad ; \quad \phi = (\mathbf{k}, \lambda) \quad , \quad \phi' = (\mathbf{k}', \lambda)$$

such that (3.33)

$$\mathbf{v}_{\phi'} = \mathbf{v}_{\phi} - 2(\mathbf{v}_{\phi} \cdot \hat{\mathbf{n}}_l) \hat{\mathbf{n}}_l$$

where $e_{\phi l}$ represents the energy density at the boundary control area Γ_l which intersects the facet of the i^{th} control volume, i.e. there is a facet f of $\partial\Omega_i$ such that $\Gamma_l = \partial\Omega_{if}$. The specular scattering condition thus determines $e_{\phi l}$ for control areas intersecting Γ^s and ϕ propagating into the domain from the boundary.

3.3.3.3 Diffuse Scattering Condition

Fabrication techniques for nanoscale devices often create disorder within the crystalline lattice near, or at, the device surface. This surface roughness is assumed to diffusely reflect phonons [39, 117]. Diffuse reflection means the energy in phonon modes colliding with the boundary is *thermalized*. Thermalization refers to the transfer of energy in phonon modes incident on the boundary into incoming phonon modes in a manner which equilibrizes the phonons locally at the boundary. Specifically, the energy is redistributed according to Bose-Einstein statistics amongst the incoming modes [118]. The equilibrium boundary temperature, T_b , is determined such that there is zero net flux across the boundary, thus the diffuse scattering condition is adiabatic. Note that the diffuse scattering condition is different than the applied temperature condition in that the boundary temperature is not predetermined, but rather wholly determined by the intensity of phonon impinging of the

adiabatic boundary. A diffuse scattering process is depicted in Fig. 3.7.

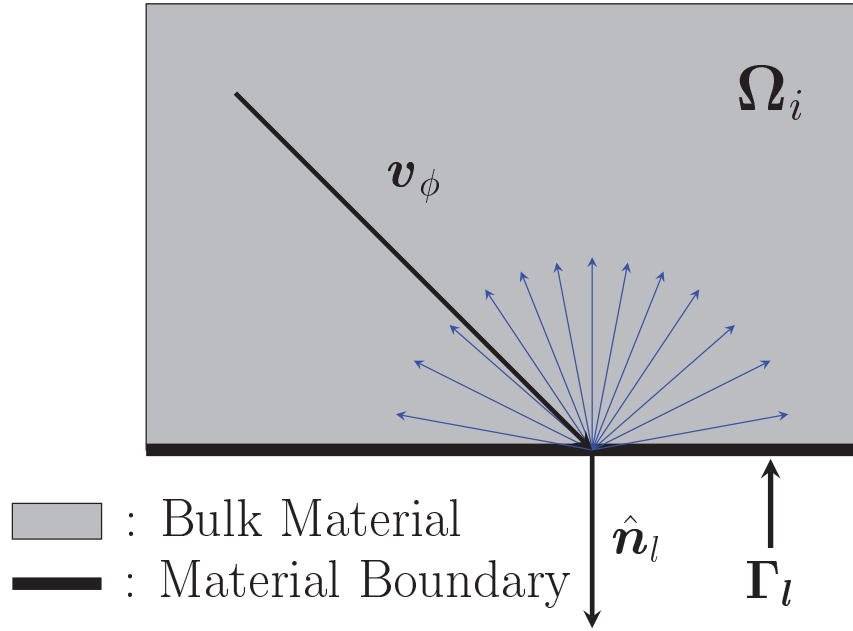


Figure 3.7: Phonon wavepacket undergoing diffuse reflection in an idealized material with radially symmetric dispersion surfaces.

The expression for diffuse reflection is

$$e_{\phi l} = e_{\phi}^0(T_b) \quad \text{such that} \quad \mathbf{v}_{\phi} \cdot \hat{\mathbf{n}}_l < 0 \quad (3.34)$$

where

$$\sum_{\substack{\phi \\ \phi \cdot \hat{\mathbf{n}}_b < 0}} e_{\phi}^0(T_b) |\mathbf{v}_{\phi} \cdot \hat{\mathbf{n}}_b| = \sum_{\substack{\phi \\ \phi \cdot \hat{\mathbf{n}}_b \geq 0}} e_{\phi i} |\mathbf{v}_{\phi} \cdot \hat{\mathbf{n}}_b| \quad (3.35)$$

recalling that $e_{\phi}^0(T_b) = C_{\phi}(T_b - T_{ref})$, the boundary temperature can be directly calculated as

$$T_b = T_{ref} + \frac{\sum_{\substack{\phi \\ \phi \cdot \hat{\mathbf{n}}_b \geq 0}} e_{\phi i} |\mathbf{v}_{\phi} \cdot \hat{\mathbf{n}}_b|}{\sum_{\substack{\phi \\ \phi \cdot \hat{\mathbf{n}}_b < 0}} C_{\phi} |\mathbf{v}_{\phi} \cdot \hat{\mathbf{n}}_b|} . \quad (3.36)$$

Note that $e_{\phi i}$ corresponds to the bulk control volume, Ω_i which intersects the boundary control area Γ_l . Thus $e_{\phi l}$ of the facets that intersect Γ^d are known. The redistribution that occurs during thermalization is on a *per branch* basis. The diffuse scattering resists the component of energy flux tangential to the material boundary, and therefore gives rise to thermal resistance at the domain surface.

3.3.3.4 Periodic Condition

Periodic boundary conditions assume that the phonon deviation from equilibrium is periodic. More precisely, we specify that at point \mathbf{r}_0 , the local equilibrium temperature is T_0 , and similarly at point \mathbf{r}_1 , the local equilibrium temperature is T_1 . These two points are separated by the translation vector $\mathbf{T} = \mathbf{r}_1 - \mathbf{r}_0$. Periodic boundary conditions then state that the deviation of energy in phonon mode ϕ from equilibrium, as determined by the local temperature, is periodic with respect to the translation vector \mathbf{T} . This is expressed mathematically as

$$e_{\phi}(\mathbf{r}_0) - e_{\phi}^0(T_0) = e_{\phi}(\mathbf{r}_1) - e_{\phi}^0(T_1) \quad (3.37)$$

It is assumed that each control area Γ_l that is prescribed as a periodic boundary has a corresponding control area $\Gamma_{l'}$ such that $\mathbf{r}_{l'} = \mathbf{r}_l + \mathbf{T}$, where \mathbf{r}_l and $\mathbf{r}_{l'}$ are the centroids of control areas Γ_l and $\Gamma_{l'}$ respectively.

In practice the periodic boundary conditions are implemented as follows. Consider the control area pair Γ_l and $\Gamma_{l'}$. Associated with Γ_l is the centroid \mathbf{r}_l , local temperature T_l , and intersecting control volume Ω_i . Analogously, associated with $\Gamma_{l'}$ is the centroid $\mathbf{r}_{l'}$, local temperature $T_{l'}$, and intersecting control volume $\Omega_{i'}$.

The centroids are connected by the translation vector \mathbf{T} such that $\mathbf{r}_{l'} = \mathbf{r}_l + \mathbf{T}$. The incoming phonon modes at Γ_l and $\Gamma_{l'}$ are then determined to be

$$\begin{aligned} e_{\phi l} &= e_{\phi l'} + C_\phi [T_l - T_{l'}] & : & \quad \mathbf{v}_\phi \cdot \mathbf{T} \geq 0 \\ e_{\phi l'} &= e_{\phi l} + C_\phi [T_{l'} - T_l] & : & \quad \mathbf{v}_\phi \cdot \mathbf{T} < 0 . \end{aligned} \tag{3.38}$$

The periodic boundary condition is used to replicate infinite systems. A subset of infinite systems are phononic systems, which have generated widespread interest due to their desirable thermal transport properties. Phononic systems are defined by an artificial secondary periodicity that exists in addition to the atomic level periodicity inherent in every crystalline lattice.

All four types of boundary conditions amount to specifying the solution variable e_ϕ over all of Γ . Our approach calculates the energy densities at all control areas from the energy field of the control volumes. Additionally, diffuse, specular, and periodic boundary conditions are dependent upon the solution field and will therefore require an iterative procedure to obtain the steady state solution.

3.3.4 Determination of Phonon Properties

The full Brillouin zone properties that serve as inputs to the numerical method must be determined for all phonon modes, i.e. for all $\phi \in \Phi$. The required properties are frequency (ω_ϕ), group velocity (\mathbf{v}_ϕ), specific heat (C_ϕ), and relaxation time (τ_ϕ). Together with Born von-Karman boundary conditions, these properties respectively define the vibrational mode frequencies of the lattice, the velocity at which energy is transported by each mode, the amount of energy each mode can store, and the average time between collisions of each phonon carrier. The properties can be ob-

tained from either classical or quantum modeling techniques. We presently employ a simple classical potential for the sake of convenience.

It is important to note that due to the anisotropic nature of crystalline systems, the properties will also be anisotropic in general. Only, in the special case where k points lie on spherical constant frequency surfaces in the Brillouin zone, the phonon properties are isotropic. By accounting for the anisotropy of phonon properties in the method described here, any anisotropy in thermal flow will also be captured.

In what follows, standard phonon dispersion calculation methods are employed. These are extensively described in classic references [50, 98, 119] whose details are not critical to this paper. Thus readers are referred to these texts for a more in-depth discussion of the determination of phonon properties, while presently we limit the discussion to more practical methodology details. Specifically we will detail the approach for determining the phonon properties used in Ch. 4, where the extension of these techniques to other problems is straightforward.

3.3.4.1 Frequencies

Crystal lattices are invariant under certain rotation and reflection operations, and the Brillouin zone of the lattice also possesses the same invariance properties, or *point group symmetries*. Furthermore, a function in reciprocal space will exhibit the same symmetry properties [50]. The dispersion relation, i.e. frequencies $\omega(\mathbf{k})$, of the lattice is such a function and therefore all unique frequency values are contained in a subset of the Brillouin zone [50]. This subset is referred to as the *irreducible*

wedge. Thus when obtaining the frequencies for all allowed kpoints, only frequencies of kpoints falling within the irreducible wedge need be determined. Then the frequencies for other kpoints in the BZ can be determined through point group operations. In this paper, this will be shown for a crystal structure that has a cubic symmetry by generating the full BZ from the irreducible wedge through $\pi/2$ rotations about the \hat{e}_1 , \hat{e}_2 , and \hat{e}_3 Cartesian axes. For such a crystal the irreducible wedge coincides with the positive octant of the Brillouin zone, $\mathbb{BZ}^+ \subset \mathbb{R}^3$, where

$$\mathbb{BZ}^+ = \{\mathbf{k} \in \mathbb{BZ} : k_x \geq 0, k_y \geq 0, k_z \geq 0\}. \quad (3.39)$$

A wide variety of techniques exist for the determination of the phonon frequencies, any of which may be used with the present developments. We chose to use the molecular dynamics package General Utility Lattice Program (GULP) [120] to obtain the frequencies for the cases considered in chapters 4-6. Once the frequencies within the irreducible wedge are determined, the remaining phonon mode frequencies in the rest of the Brillouin zone are determined from the point group symmetry of the cubic lattice. The frequencies in \mathbb{BZ} are related to those within \mathbb{BZ}^+ through the relation

$$\begin{aligned} \omega_{\phi'} = \omega_{\phi} ; \quad \phi &= (\mathbf{k}, \lambda) \quad , \quad \mathbf{k} = (k_x, k_y, k_z) \in \mathbb{BZ}^+ \\ \phi' &= (\mathbf{k}', \lambda) \quad , \quad \mathbf{k}' = (\gamma k_x, \gamma' k_y, \gamma'' k_z) \in \mathbb{BZ} \end{aligned} \quad (3.40)$$

where $\gamma, \gamma', \gamma'' \in \{+1, -1\}$. Note that this relation is material dependent, i.e. corresponds to the point group symmetry of the lattice. Therefore, in general, other relations would be required for crystals with a non-cubic symmetry.

3.3.4.2 Group Velocities

The phonon group velocity for mode ϕ is defined as [121]

$$\mathbf{v}_\phi = \frac{\partial \omega_\phi}{\partial \mathbf{k}}. \quad (3.41)$$

The group velocity defines the speed and direction with which energy in mode ϕ can travel. In order to determine the group velocity for all physically allowed phonon modes the following procedure is used. First the set of allowed kpoints which fall within the irreducible wedge of the Brillouin zone, \mathbb{BZ}^+ , are determined. For a general kpoint, $\mathbf{k} = (k_x, k_y, k_z) \in \mathbb{BZ}^+$, the central differencing scheme is used to determine \mathbf{v}_ϕ by generating six perturbed kpoints

$$\left\{ \begin{array}{l} \mathbf{k}_{+x} = (k_x + \Delta k, k_y, k_z) \\ \mathbf{k}_{-x} = (k_x - \Delta k, k_y, k_z) \\ \mathbf{k}_{+y} = (k_x, k_y + \Delta k, k_z) \\ \mathbf{k}_{-y} = (k_x, k_y - \Delta k, k_z) \\ \mathbf{k}_{+z} = (k_x, k_y, k_z + \Delta k) \\ \mathbf{k}_{-z} = (k_x, k_y, k_z - \Delta k) \end{array} \right.$$

At all six of the perturbed kpoints, the frequencies are determined in the same manner used in Sec. 3.3.4.1. The frequencies at the perturbed kpoints are then used to determine the phonon mode group velocity via central differencing

$$\begin{aligned} v_{\phi x} &= \frac{\partial \omega_\phi}{\partial k_x} = \frac{\omega_{+x} - \omega_{-x}}{2\Delta k} \\ v_{\phi y} &= \frac{\partial \omega_\phi}{\partial k_y} = \frac{\omega_{+y} - \omega_{-y}}{2\Delta k} \\ v_{\phi z} &= \frac{\partial \omega_\phi}{\partial k_z} = \frac{\omega_{+z} - \omega_{-z}}{2\Delta k} \end{aligned} \quad (3.42)$$

where $\omega_{\pm\alpha}$ is the respective frequency corresponding to wavevector $\mathbf{k}_{\pm\alpha}$ where $\alpha = x, y, z$.

Next the phonon mode group velocities through the rest of the Brillouin zone are determined using symmetry relations and the fact that group velocity is an odd function of k_x, k_y , and k_z [33]. Letting \mathbf{v}_ϕ be the group velocity of mode $\phi = (\mathbf{k}, \lambda)$ where $\mathbf{k} \in \mathbb{BZ}^+$. Then the group velocity of any mode $\phi' = (\mathbf{k}', \lambda)$, where \mathbf{k}' is a permutation of \mathbf{k} such that $\mathbf{k}' = (\gamma k_x, \gamma' k_y, \gamma'' k_z)$ and $\gamma, \gamma', \gamma'' \in \{+1, -1\}$, is given by the relation

$$\begin{aligned} v_{\phi'x} &= \gamma v_{\phi x} \\ v_{\phi'y} &= \gamma' v_{\phi y} \\ v_{\phi'z} &= \gamma'' v_{\phi z} \end{aligned} \tag{3.43}$$

By using the antisymmetry of the group velocity in k_x, k_y , and k_z , \mathbf{v}_g for all modes is determined.

3.3.4.3 Specific Heat

The lattice capacity for energy storage can be composed from the contributions of the individual phonon modes. It can be expressed in the form of the specific heat. In control volume i , the total specific heat is

$$C_i = \sum_{\phi \in \Phi} C_{\phi i} \tag{3.44}$$

and depends only on the frequencies of the modes. Where $C_{\phi i}$ was defined in Eq. 3.28. The mode-wise specific heat depends only on the phonon mode frequency. Therefore once the frequencies are determined via the procedure described in Sec.

3.3.4.1, the phonon mode specific heats may be determined for all phonon modes which then yield the total specific heat using Eq. 3.44.

3.3.4.4 Relaxation Times

The collisional term in the phonon BTE, Eq. 3.13, represents a variety of phonon interaction processes such as phonon-phonon, phonon-electron, and phonon-impurity scattering. In infinite defect-free semiconductors only phonon-phonon scattering is present as this form of scattering arises from the intrinsic anharmonicity of the atomic interactions [98]. In this work we restrict our study to that of pristine lattices and therefore assume the only intrinsic scattering mechanism is phonon-phonon interactions. The phonon-phonon scattering term, and the associated wide array of modeling approaches, was discussed in detail in Ch. 2. We use the RTA to model phonon-phonon collisions, where the RTA was described in sec. 2.1.3.

The relaxation time τ represents the average time a phonon travels before colliding with a boundary, impurity, or other energy carriers. During extended periods of ballistic flight, the phonon mode can deviate from equilibrium and no longer be represented by Bose-Einstein statistics, N_{ϕ}^0 . Collisions are restorative in the sense of helping to return the phonon to the equilibrium distribution. A wide range of relaxation time expressions appear in the literature. Early expressions for τ were derived from theory using simplifications such as the assumption of low temperature [49, 83], or were fit to experimental data for bulk crystals [122]. However, *ab-initio* calculations performed using density functional perturbation theory (DFPT)

allow relaxation times to be fit to data obtained from third-order force constants. Analytic models for relaxation times, parameterized in this way, have been found to accurately predict the thermal conductivity of common semiconductor materials silicon and germanium [123].

A commonality amongst most empirical models is that the phonon mode relaxation time depends on temperature and mode frequency i.e. $\tau_\phi = \tau_\phi(\omega_\phi, T)$, where the exact functional form depends on the specific model. Therefore, once the appropriate empirical formula has been chosen for the problem under consideration, the relaxation times may be calculated using the frequencies as determined in sec. 3.3.4.1, and temperature $T = T_{ref}$ where T_{ref} was defined in Sec. 3.3.2.

3.4 Verification

To verify the numerical implementation of the methodology, we first demonstrate that numerical solutions recover the classic isotropic gray solution for a semi-infinite continuum slab. Physically, this problem corresponds to a slab of material, infinite in the lateral dimensions, with a finite width. Furthermore, the heat carriers within the material are gray, i.e. have the same specific heat, group velocity magnitude, and relaxation time, and the propagation directions of the carriers is an infinite continuum. We test solutions for convergence as a function of the number of kpoints using a spherical Brillouin zone that has a single dispersionless branch. Mathematically, this problem is identical to that of a gray photon radiating across an open gap for which analytical solutions are known [67, 124, 125].

At small slab thickness, the gray phonon model predicts that the transport is ballistic, i.e. phonons propagate through the slab without scattering, and strong deviation occurs from the equilibrium carrier distribution. With increasing slab width, the transport takes on a more diffusive character as phonons undergo a significant number of scattering events [42]. Therefore, this problem serves as a good measure for whether our method is capturing ballistic and diffusive transport as well as the intermediate regime. The general solution for the normalized temperature, Φ_b , is given by [67]

$$\Phi_b(x) = \frac{1}{2} \left[E_2(x) + \int_0^L \Phi_b(x') E_1(|x - x'|) dx' \right] \quad (3.45)$$

$$\Phi_b(x) = \frac{T^4(x) - T_2^4}{T_1^4 - T_2^4} \quad ,$$

where L is the slab thickness normalized by the MFP, T_1 and T_2 are the prescribed temperatures on the two slab faces, and the elliptic integral is defined as

$$E_n(x) = \int_0^1 \mu^{n-2} e^{-x/\mu} d\mu . \quad (3.46)$$

x is the distance along the domain normalized by the mean free path of the phonons. Thus all distance quantities are expressed as a fraction of the phonon MFP. The MFP for a phonon mode ϕ is defined as $\Lambda_\phi = |\mathbf{v}_\phi \tau_\phi|$, where because the material is gray Λ_ϕ reduces to a constant, $\Lambda_\phi = \Lambda$. Φ_b is determined through the *method of successive approximations* (details can be found in [67]) using the trapezoidal rule with 4000 intervals which ensures an L_2 error of less than 10^{-8} .

3.4.0.1 Pseudo-1D Slab

The physical setup of the pseudo-1D slab numerical experiment is depicted in Fig. 3.8. The large slab has front and back faces held at two different temperatures. To simulate the infinite lateral directions, the slab is modeled as a large brick-shaped material of a small thickness along the x -direction with specular reflection conditions imposed on the four faces oriented normal to the x -direction. In this set up, like the original classic problem, temperature and energy profiles will vary only in a single direction, i.e. the x -direction in Fig. 3.8, despite the present use of three-dimensional real space geometries and Brillouin zones. A slab of variable thickness but with an area of $1000\Lambda \times 1000\Lambda$ is discretized into a $1000 \times 3 \times 3$ spatial grid of control volumes, where the finer discretization is along the thickness (x) direction. The accompanying gray phonon properties are given in Table 3.4.0.1.

Group Velocity Magnitude	$ v $	$6400 \frac{\text{m}}{\text{sec}}$
Relaxation Time	τ	$7.2 \times 10^{-12} \text{ sec}$
Frequency	ω	16.0 THz
Mean Free Path	Λ	$4.608 \times 10^{-8} \text{ m}$

Table 3.1: Gray phonon properties

The front and back faces have an applied temperature boundary conditions with $T(x = 0) = T_1 = 301K$ and $T(x = L) = T_2 = 300K$. We calculate the error between our BTE solution and the analytical formula given in Eq. 3.45 for a range of

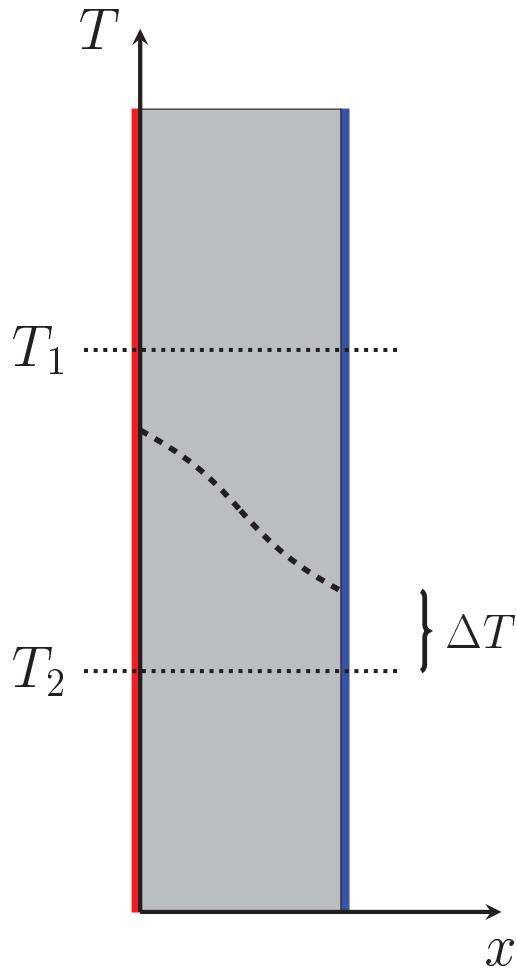


Figure 3.8: Temperature profile (thick dashed line) of a slab geometry composed of material with gray phonon properties. The Fourier boundary conditions at the boundaries are given by the temperatures T_1 (red) and T_2 (blue).

kpoint refinements. Eight Brillouin zone models were created with different numbers of kpoints (shown in Fig. 3.9) to study the refinement effect. The kpoints lie on the surface of the sphere in a roughly uniform distribution with the number of kpoints ranging from 102 to 49,426 points. A simulation that would be identical to the analytical model would have a spherical Brillouin zone with an infinite continuum

of kpoints covering the sphere. Three different slab thicknesses of $.1\Lambda$, 0.5Λ , 1Λ are studied.

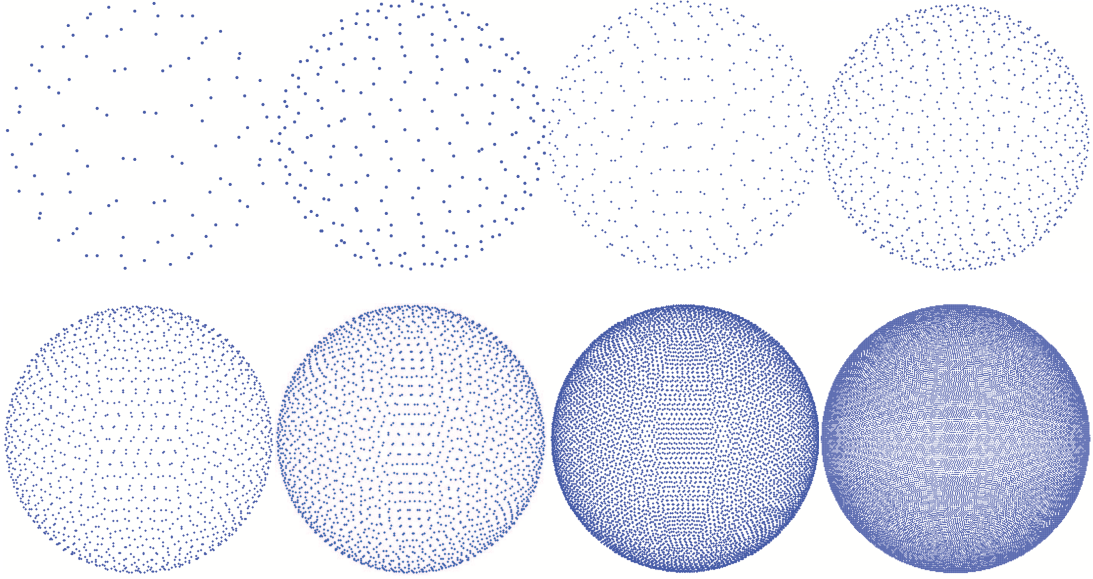


Figure 3.9: Spherical Brillouin Zones of (a) 102 kpoints (b) 236 kpoints (c) 408 kpoints (d) 824 kpoints (e) 1444 kpoints (f) 2208 kpoints (g) 9092 kpoints (h) 49426 kpoints. Kpoints are placed on the surface of a sphere so that their distribution is as uniform as possible.

3.4.0.2 Verification Results

For each slab thickness, the difference between the computed and analytical temperature solutions are plotted Fig. 3.10. The pointwise error is plotted for Brillouin zones containing 102, 1444, and 49426 kpoints to show the reduction in error as the number of kpoints is increased. The error is greatest near the slab boundaries. Error near the boundaries is likely a result of two compounding issues, namely, a) the finite number of carriers which cannot fully sample the entire hemisphere of

directions in which the energy can theoretically propagate, and b) the finite gap between the boundary and the first interior control volume grid point. As the slab thickness decreases, transport becomes purely ballistic, resulting in a wall temperature slip [67]. This temperature slip is predicted in the analytical solution, where there exists a discontinuity in the energy field as we take an infinitely small step into the material away from the fixed temperature wall. The temperature slip is a result of transport being ballistic due to the absence of phonon-phonon scattering, leading to a highly non-equilibrium system.

The L_2 -norm error is shown in Fig. 3.11 as a function of the number of kpoints. For slab thicknesses $\Lambda/10$ and $\Lambda/2$ the convergence rate appears to be roughly .5 while for a slab thickness of Λ the convergence is approximately .3. The convergence with respect to kpoint refinement, as seen in Fig. 3.11, is clearly non-monotonic. This behavior is an unavoidable consequence of using discrete kpoints to represent a continuum of solid angles in which the carriers can propagate. When the discrete kpoints are unevenly distributed over the sphere surface, a relatively larger error is observed. Achieving a perfectly even distribution of points on a sphere is an unsolved classic mathematical problem known as Fejes Tóth's Problem. Thus, the non-monotonic convergence seen in the present results is attributed to possible uneven placement of kpoints on the spheres seen in Fig. 3.9. Methods such as the Control Angle Discrete Ordinates Method (CADOM) [67] employ a weighted approach based upon associating a control area with each kpoint. Thus CADOM represents a more accurate model of the continuum of propagation directions. In Fig. 3.11, the convergence rate noticeably declines with increasing slab thickness.

This trend is attributable to the use of the same number of control volumes, in the thickness direction, for all slab models. Thus the control volumes are effectively larger for larger slab thickness whereas the phonon mean free path remains constant. This implies that the thicker slab is studied with a relatively coarser grid which in general leads to larger error, even in spite of kpoint refinement.

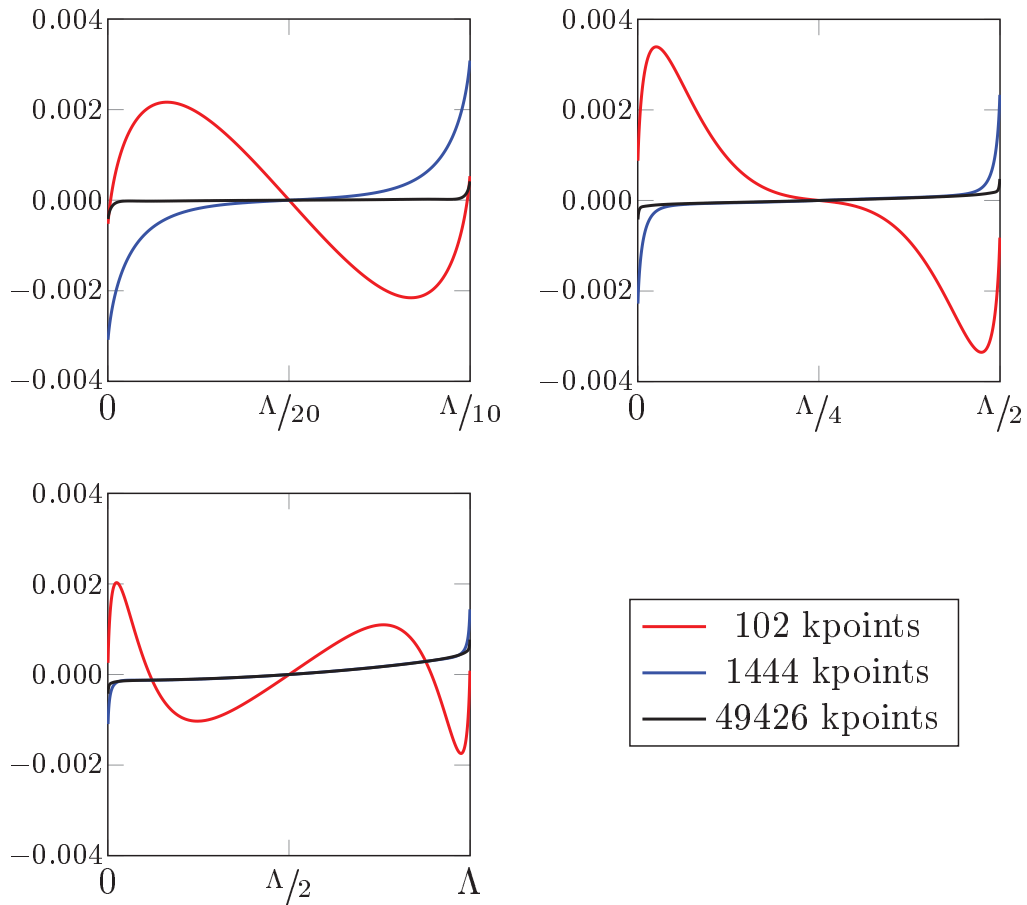


Figure 3.10: Point wise error in the temperature results for numerical experiment of 1D slabs with varying thickness.

Using a fixed number of 99,576 kpoints, real space grid refinement shows convergence to the exact solution in Fig. 3.12, with a rate of convergence of the

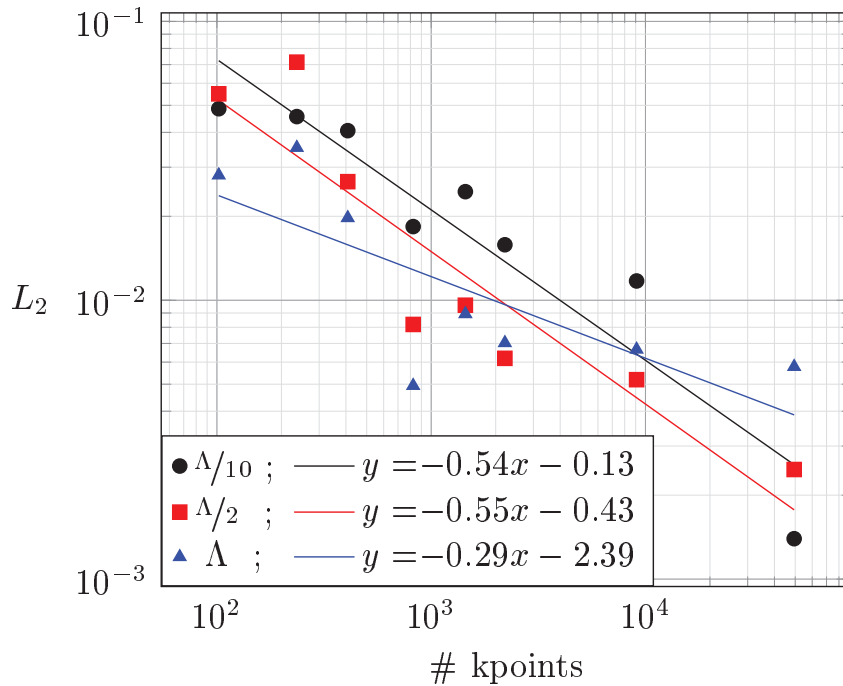


Figure 3.11: RMS error vs. number of kpoints in Brillouin zone for varying slab thickness.

RMS error of approximately 1. This convergence rate is consistent with the use of the first order upwinding scheme. Note that the upwinding scheme used here will suffer from false diffusion which can be mitigated through the use of higher order differencing schemes [126].

This completes the presentation of the solution method for the full Brillouin zone three-dimensional phonon BTE. In sections 3.2 and 3.3 we defined the microscale thermal transport problem and detailed the discretization approach for numerically solving a set of phonon Boltzmann equations. Section 3.3.4 contained a discussion of a practical approach for calculating the full Brillouin zone phonon transport properties. Finally in sec. 3.4 we verified the implementation of the com-

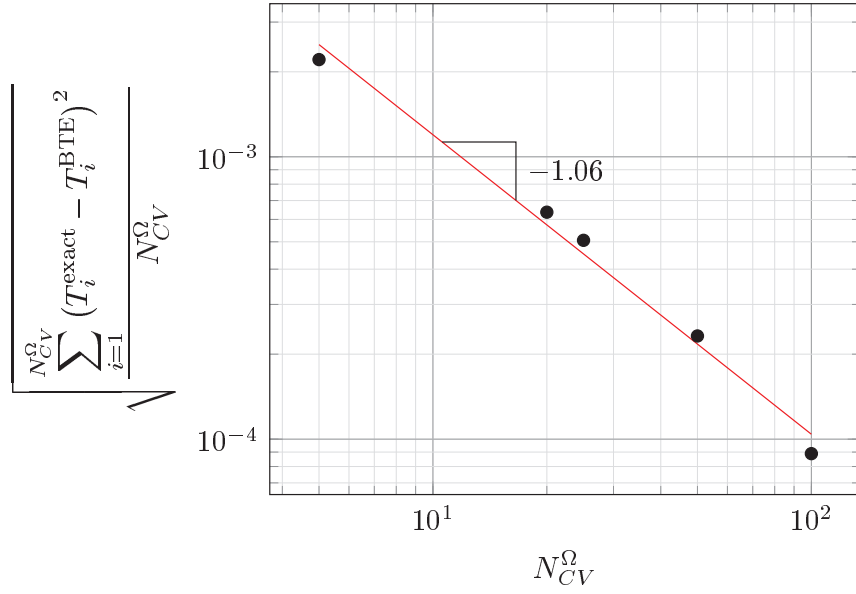


Figure 3.12: Root mean square (RMS) error between the Boltzmann method and the exact numerical solution from Eq. 3.45 for variable grid sizes. Slab thickness is $\Lambda/10$.

puter method. The remainder of this work presents applications of our methodology to thermal engineering problems in microscale and nanoscale systems.

Chapter 4: Effect of Phonon Anisotropy in FinFET Device ³

In chapter 3 we presented our numerical methodology for the simulation of heat transport at the microscale via the solution of the three dimensional phonon BTE. In this chapter a series of simulations are performed, using our newly developed methodology, to calculate temperature and energy profiles in a fin field effect transistor composed of a cubic crystalline material. The anisotropic thermal conductivity and the accompanying significance on thermal fields are calculated. The differences between an isotropic solution and the anisotropic model are shown to be significant with differences in the temperatures approximately 10%. Furthermore, the temperature differences between a partially isotropic model and the fully anisotropic model are found to be as large as 30%. At larger scales, where phonon-phonon scattering becomes more prevalent, differences in the solutions become smaller and macroscopic isotropy is recovered due to the cubic symmetry of the material.

³Portions of this chapter appeared in the publication: *F. G. VanGessel, P. W. Chung, An anisotropic full Brillouin zone model for the three dimensional phonon Boltzmann transport equation. Comput. Methods Appl. Mech. Engrg. (2017), <http://dx.doi.org/10.1016/j.cma.2017.01.010>* [30]

4.1 FinFET Device Simulation

A FinFET is a transistor design in which the semiconducting material has a vertical "fin" geometry, surrounded by a gate on two or three sides (see Fig. 4.1).

The multi-gate design allows for better control over the flow of electrons in the

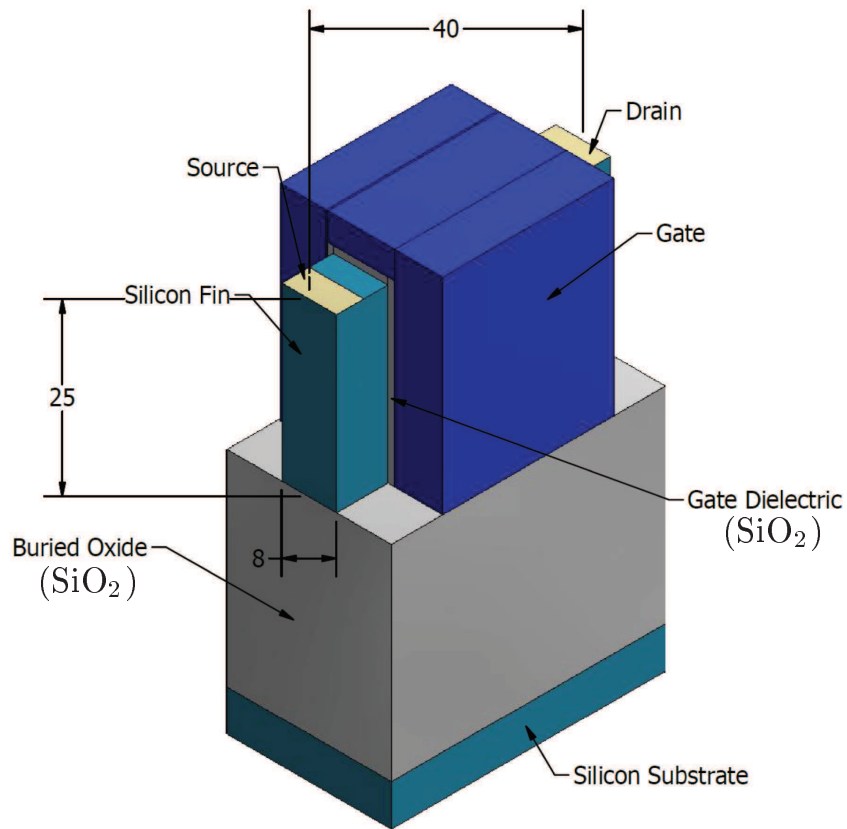


Figure 4.1: FinFET device, the dimensions are given in units of nanometers.

fin, thereby enabling smaller devices without sacrificing performance. The reduced device dimensions subsequently enables high transistor densities which enable faster and more capable central processing units (CPUs). However, the reduced sizes lead to increased boundary scattering, exacerbating localized Joule heating effects. Joule

heating refers to the electron-phonon interactions which occur in the presence of an electric current. As the electrons move under the influence of an electric field, they collide with the atomic lattice creating phonons and therefore heat. Overheating in FinFETs is known to degrade device performance and shorten device lifetime [5]. In this section we investigate thermal effects in a FinFET undergoing Joule heating, by modeling the effect of full Brillouin zone representation, and finite dimensional structural features, on the thermal flow. The importance of anisotropic effects in a nanostructure is quantified by calculating the peak temperature within the FinFET for both an isotropic, and full, Brillouin zone representation.

4.1.0.1 FinFET Numerical Experiment Problem Set-Up

For the parameter study, three fin widths were chosen as well as three source region geometries (the latter drawn from [2]). The overall energy sourced into the system due to Joule heating is assumed to be the same regardless of the geometry of the fin or heated region. The FinFET dimensions are on the same order of magnitude as the phonon MFPs at 300K, placing transport in the semi-ballistic regime.

For the sake of this numerical experiment, we assume the material is an idealized Lennard-Jones solid with a simple cubic crystal lattice, with nearest neighbor (NN) and next nearest neighbor (NNN) interactions. The associated Brillouin zone is depicted in Fig. 4.2. The interatomic potential is

$$V_n(r_{ij}) = 4B_n \left(\frac{A_n^{12}}{r_{ij}^{12}} - \frac{A_n^6}{r_{ij}^6} \right) \quad n = NN \text{ or } NNN \quad (4.1)$$

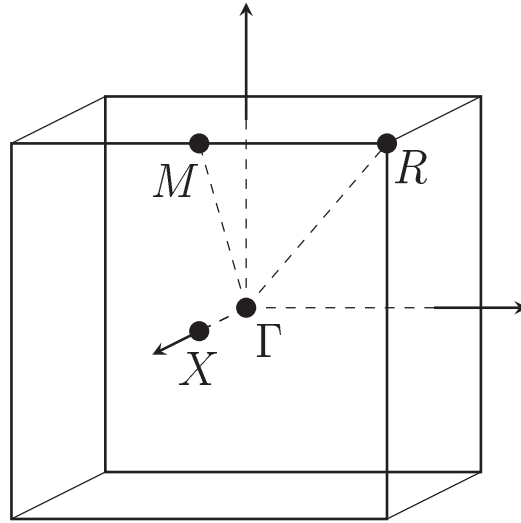


Figure 4.2: Brillouin zone for idealized Simple Cubic Lattice including high symmetry points (Γ , X , M , and R)

where r_{ij} is the distance between atoms i and j , and A_n and B_n are the Lennard-Jones parameters. The associated parameters are listed in Table 4.1. The dispersion surfaces of the cubic lattice material is depicted in Fig. 4.3 in the $k_z = 0$ plane of the three dimensional Brillouin zone. The microscopic anisotropy is clearly demonstrated by the non-circular constant frequency contours. Figure 4.3 shows the continuous dispersion curves which would apply to an infinitely large material, whereas as a consequence of the Born von-Karman boundary conditions, only a discrete set of points lying on these curves represent actual carriers in a finite-size system. This means that the shape of the structure, i.e. FinFET dimensions, will influence the anisotropy. Specifically, unequal fin dimensions necessarily yields a distribution of carriers which are not uniformly spaced along each of the three principal directions.

This non-uniformity results in anisotropic thermal flow in spite of the cubic symmetry of the crystal. Thus the microscopic anisotropy, due to non-radially symmetric dispersion surfaces, *and* the lattice anisotropy due to Born von-Karman conditions will both contribute to the total observed anisotropy in the system. For this exam-

A_{NN}	4.4545×10^{-10} [m]
B_{NN}	2.7×10^{-20} [J]
A_{NNN}	6.2996×10^{-10} [m]
B_{NNN}	1.9×10^{-20} [J]

Table 4.1: Interatomic potential constants

ple, we use the empirical relaxation time model from [1] to model phonon-phonon collisions. The relevant properties are summarized in Tables 4.2 and 4.3.

Polarization	τ_U^{-1}	τ_N^{-1}
Transverse	$B_{TU}\omega^2 T e^{-C_T/T}$	$B_T\omega T^4$
Longitudinal	$B_{LU}\omega^2 T e^{-C_L/T}$	$B_L\omega^2 T^3$

Table 4.2: Functional form of the phonon scattering rates from [1] for both Umklapp, τ_U^{-1} , and normal, τ_N^{-1} , scattering rates.

We apply the heating selectively in control volumes that are located in regions known to have the highest electron density, namely the so-called *channel* region. The

B_T [K ⁻⁴]	B_{TL} [s/K ³]	B_{TU} [s]	B_{LU} [s]	C_T [K]	C_L [K]
2×10^{-13}	2×10^{-21}	1×10^{-19}	5×10^{-19}	55	180

Table 4.3: Parameter values for phonon scattering rates in Table 4.2 given by [1]

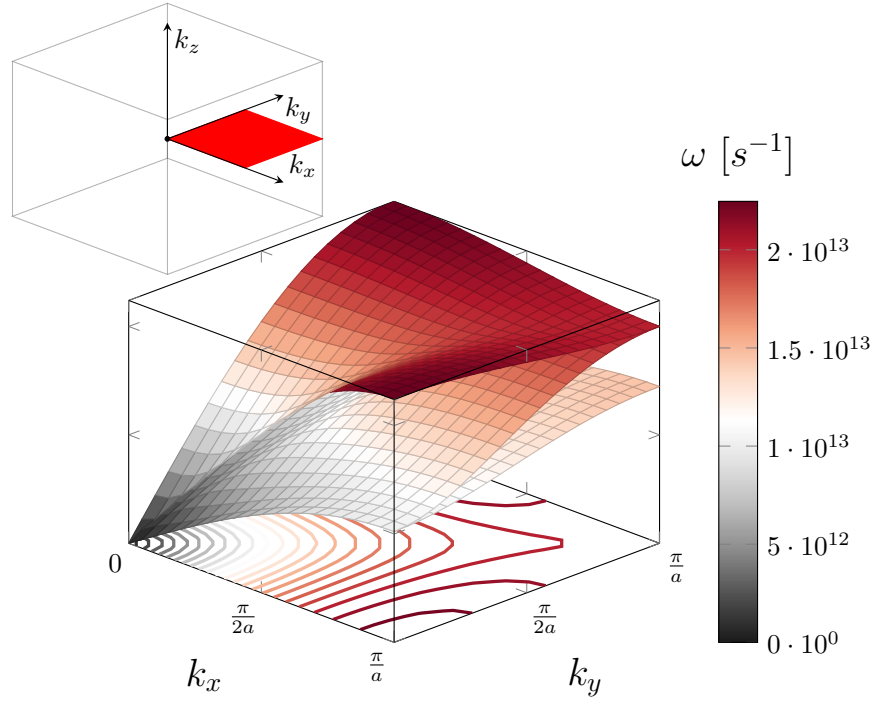


Figure 4.3: Dispersion surfaces in a quadrant of the $k_z = 0$ plane. The constant frequency contours of the longitudinal acoustic branch are projected below the dispersion surfaces.

shape of the channel varies because a higher applied voltage draws the conducting electrons closer to the gate interface. To consider the spatial variation in electron density as the voltage changes, three different channel region geometries were used corresponding to the shapes estimated for the low, middle, and high voltage scenarios [2]. These are labeled channels I, II, and III and are shown in Fig. 4.4, where the depth, i.e. length in x -direction, of all channels is set to 10 nm. Joule heating imparts energy to phonon modes that are relatively close in energy to the energy of

the electrons [127]. Namely, the probability that electron-phonon scattering imparts energy into phonon modes with energy levels comparable to the energy of electrons is significantly larger than the probability that the energy will scatter into a low energy acoustic phonon mode. Phonon-phonon interactions then scatter energy deposited into high energy phonon modes into lower energy acoustic modes. The low-energy acoustic modes, in general, have larger group velocities and therefore subsequently transport energy away from the channel region. To capture this effect, nontrivial source terms are applied only to modes whose frequencies are larger than $\omega_{max}/2$ where $\omega_{max} = \max_{\phi \in \Phi} \omega_{\phi}$. We use ω as a discriminator for high-energy modes as the energy of a phonon is linearly related to the phonon frequency, i.e. a quanta of energy in phonon mode ϕ has energy $\hbar\omega_{\phi}$. No source term is applied to lower energy modes. The total energy injected into the channel is constant for all fin widths and for all channel geometries. The total energy per unit time sourced into the domain is 3.33×10^{-7} Watts. This energy is evenly divided amongst all kpoints and to all control volumes occupying the source region.

The FinFET dimensions are also varied to investigate the effect of fin width on the temperature field. Three fin widths were considered, depicted in Fig. 4.5, the shaded brown surfaces correspond to Si/SiO₂ interfaces while all other surfaces of the fin are free surfaces. Due to symmetry of the geometry and boundary conditions only a quarter of the FinFET is simulated. However the allowed wavevectors must be determined from Born von-Karman boundary conditions using the dimensions of the full physical domain. Specular boundary conditions are applied to the symmetry surfaces. Diffuse boundary conditions are applied to the free surfaces

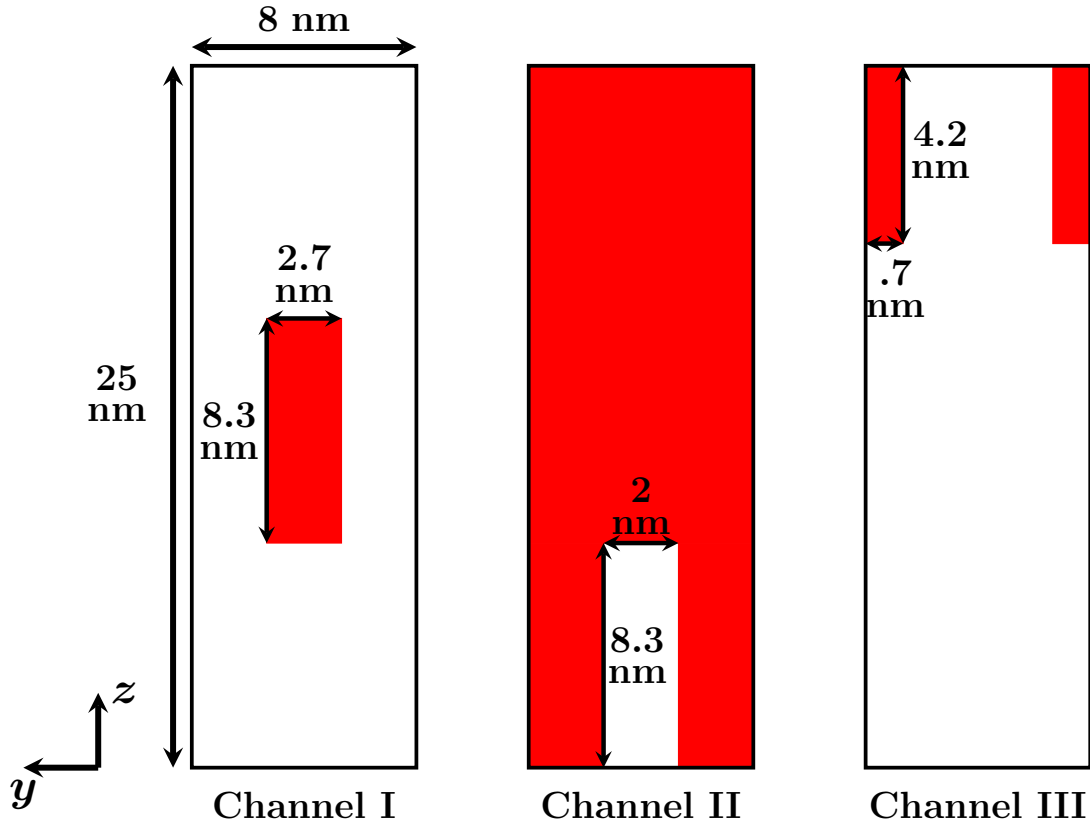


Figure 4.4: Three channel geometries simulated in FinFET device. Channels I, II, and III correspond respectively to the low, medium, and high applied gate voltage conditions [2]. Energy is sourced only into control volumes with centroids lying within the source region.

due to disorder in the crystal structure at these boundaries. Applied temperature boundary conditions are applied to the silicon/silicon dioxide (Si/SiO_2) interfaces. It is assumed that the majority of heat generated within the domain is removed through the Si/SiO_2 interfaces, corresponding to interfaces between the fin and gate dielectric as well as the fin and buried oxide. All applied temperature boundary conditions are set to 300 K.

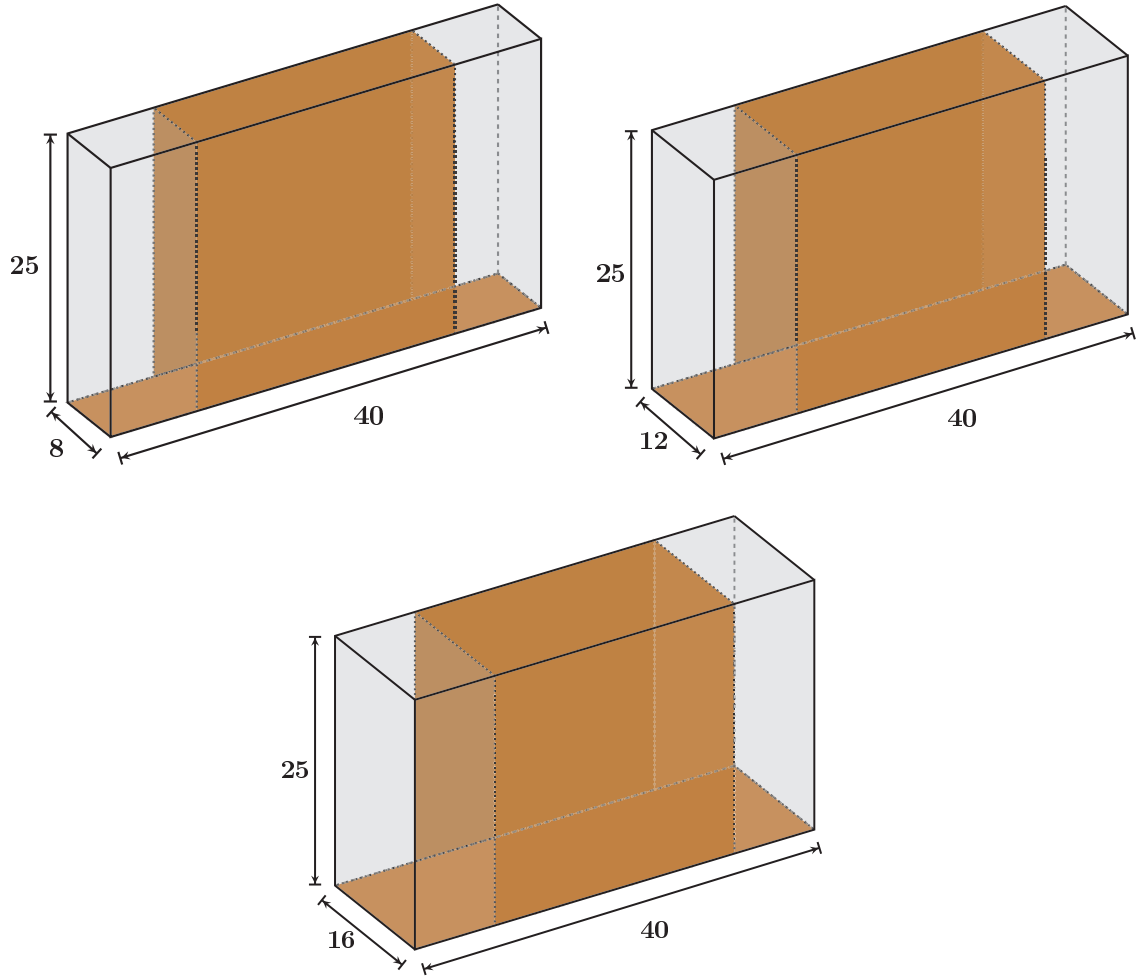


Figure 4.5: FinFET dimensions for the three fin widths, all dimensions are in units of nanometers.

4.1.0.2 Device Simulation Results

The temperature field is obtained using an iterative approach to calculate e_ϕ within all control volumes. Iteration is required since the boundary conditions depend on the energy density field. The iterations are performed until the L_2 norm of the change in the energy field at the k^{th} iteration, $\Delta e^k = \sqrt{\sum_{i=1}^{N_\Omega} \sum_{\phi \in \Phi} [e_{\phi i}^k - e_{\phi i}^{k-1}]^2}$, reaches a tolerance value of 10^{-6} . The calculated steady-state temperature fields for

all nine parameter combinations of channel geometries and fin widths are shown in Fig. 4.6, where each row corresponds to a channel geometry and each column to a fin width. The solutions show that the maximum temperature experienced by the fin depends in the shape and size of the channel region, width of the fin, and relative proximity of the channel to the non-adiabatic boundaries. As the amount of energy sourced into each system is held constant, one expects that widening the fin would result in a lowering of the peak temperature, if all other factors remain constant.

For the channel I case, the temperatures are highest in the center of the channel region and decrease sharply outside. The energy is confined to the channel region as heat is generated before phonon-phonon scattering has had a chance to transfer energy into lower frequency modes that are more conductive.

Channel II has a larger heated region volume than channel I which results in a lower peak temperature for the same total imparted energy, i.e. channel II source is of lower energy density. The channel region in this configuration is in closer proximity to the applied temperature boundary which allows for expedited removal of heat. It appears that the short distances separating the phonon generation region from non-adiabatic boundary result in transport of energy out of the domain by high-frequency phonon modes which are typically less conductive. The ability of these phonon modes to directly transport energy circumvents the need to scatter the energy to the higher velocity acoustic modes prior to removal.

Channel III produces the highest peak temperatures due to the confined region where the source energy is applied. The channel lies adjacent to an applied temperature boundary as does channel II. However this configuration has the largest

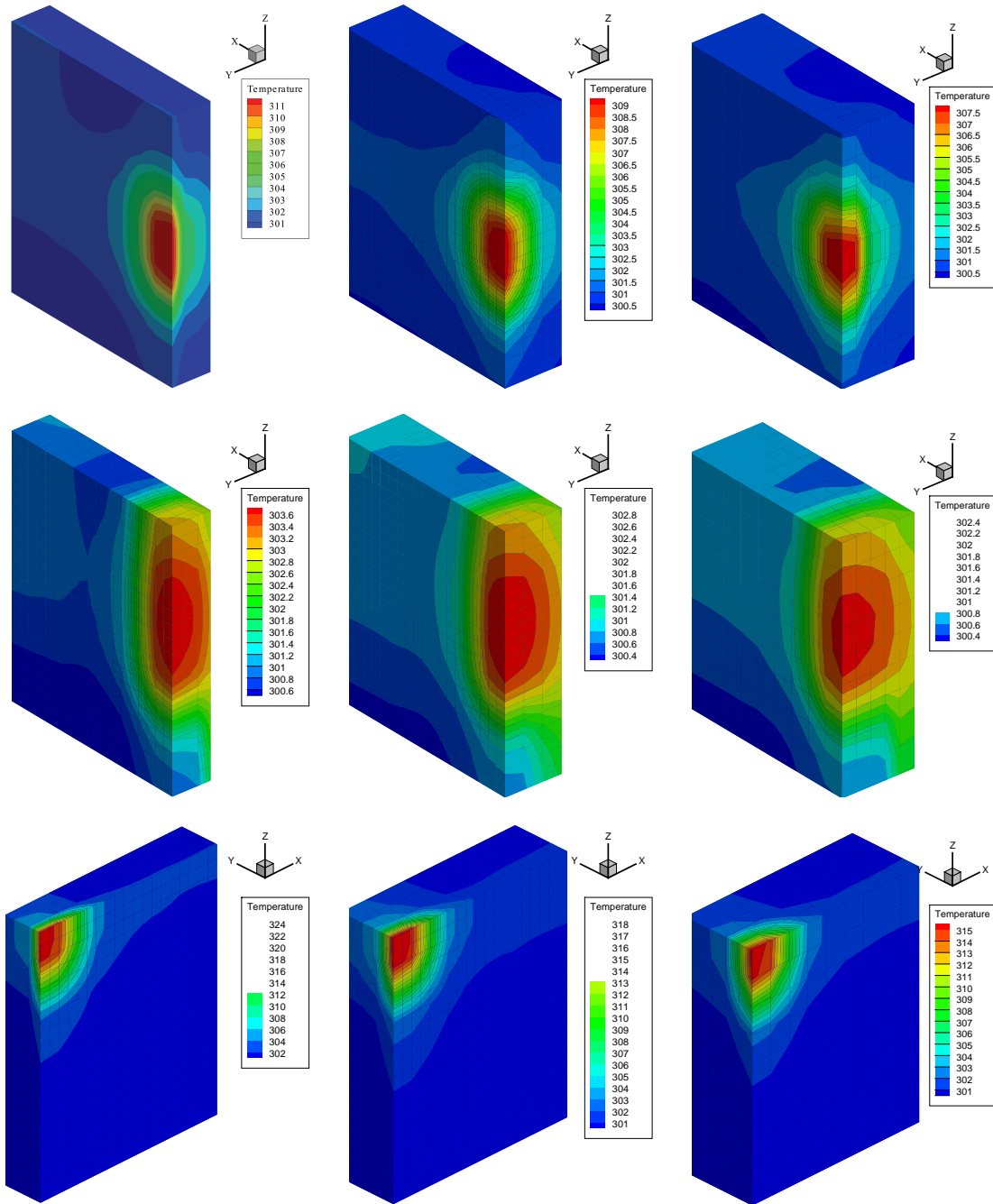


Figure 4.6: Temperature profiles obtained from the FinFET numerical experiment. The three different channel regions are labeled by row. All temperatures are reported in units of Kelvin.

energy density among the channel configurations studied. Thus, while high energy modes will expedite the removal of heat in a manner analogous to that observed in channel II, the higher local source magnitude still produces a larger peak temperature than in channel II. Also, sharp temperature gradients are observed in regions near the channel. This effect is characteristic of non-equilibrium ballistic transport at the nanoscale and has been observed in similar device simulations [39].

The maximum temperature increases are listed in Table 4.4. Several conclu-

	Thin Fin	Medium Fin	Thick Fin
Channel 1	12.245 K	9.735 K	8.276 K
Channel 2	3.823 K	3.024 K	2.535 K
Channel 3	24.966 K	19.044 K	16.048 K

Table 4.4: Maximum temperature rise in each simulation over 300K.

sions may be drawn from these results. First, smaller channel configuration volumes, corresponding to large applied gate voltages, produce larger peak temperatures. This is a consequence of our use of the same total imparted energy for all channel configurations and fin widths. Furthermore, as the fin thickness is increased, peak temperatures decrease. This is because the smaller fin is accompanied by a larger source energy density due to the same amount of energy being introduced into a smaller volume.

In order to ascertain the effects of anisotropy on the calculated temperature field, we compare anisotropic and isotropic solutions. Three simulations are per-

formed with the 8 nanometer fin in the channel I configuration. The first uses the isotropic gray phonon approximation (IBZ), the second uses a crystalline dispersive material with gray scattering (FBZ τ), and the third is of the same dispersive material but where scattering is anisotropic (FBZ). The FBZ model corresponds to our full Brillouin zone phonon BTE methodology outlined in chapter 3. The IBZ simulation uses a spherical Brillouin zone with 50,008 kpoints in the gray phonon approximation, analogous to the Brillouin zones used in the 1D slab verification problem. Isotropic scattering in an anisotropic crystalline dispersive material is not an entirely realistic assumption. However, its present use is to differentiate the anisotropy in the Brillouin zone dispersion surfaces, manifesting in the specific heat and group velocity phonon parameters, from anisotropy due to the scattering term. Isotropic scattering is enforced by employing an average relaxation time for all phonon modes in the calculation. The average relaxation time is determined from

$$\tau_{\text{avg}} = \sqrt{\frac{\sum_{\phi} \sum_{i,j=1}^3 (C_{\phi} v_{\phi i} v_{\phi j} \tau_{\phi})^2}{\sum_{\phi} \sum_{i,j=1}^3 (C_{\phi} v_{\phi i} v_{\phi j})^2}}. \quad (4.2)$$

The total specific heats in FBZ, FBZ τ , and IBZ are kept equal so that we may calculate the equivalent temperatures from the energy distributions using Eq. 3.30. The specific heat in IBZ is equally distributed amongst all modes, while the modal specific heat in FBZ and FBZ τ is calculated from Eq. 3.28. The average group velocity magnitude is then chosen such that the trace of the thermal conductivity tensors of FBZ and IBZ are equal. This ensures that thermal flow in the diffusive regime is equivalent in the two models. The gray phonon properties are given in

Tab. 4.5. The thermal conductivity tensors, in units of W/m K , for FBZ, FBZ τ , and

ω_{avg} [s^{-1}]	v_{avg} m/s	τ_{avg} [s]	C_{tot} J/K
1.363×10^{13}	1.767×10^3	3.288×10^{-11}	1.006×10^6

Table 4.5: Average phonon properties used in the IBZ BTE simulation of the Fin-FET.

IBZ are calculated using the phonon gas model of Callaway [113]. The conductivities are

$$\kappa_{\text{FBZ}} = \begin{bmatrix} 35.06 & 0 & 0 \\ 0 & 33.68 & 0 \\ 0 & 0 & 34.87 \end{bmatrix} \quad \kappa_{\text{FBZ}\tau} = \begin{bmatrix} 34.59 & 0 & 0 \\ 0 & 34.44 & 0 \\ 0 & 0 & 34.58 \end{bmatrix}$$

$$\kappa_{\text{IBZ}} = 34.54 \begin{bmatrix} 1 & 0 & 0 \\ 0 & 1 & 0 \\ 0 & 0 & 1 \end{bmatrix}$$

All simulations were performed using the same real space discretization, channel geometry, and source energy magnitude as those from the parameter study of the 8nm width fin with channel I source geometry. In FBZ and FBZ τ , the source term is applied as described in section 4.1.0.1. For the IBZ case the source term is applied equally to all phonon modes.

Figure 4.7 shows the percent differences in the temperatures along a two dimensional slice in the $y = 3\text{nm}$ plane for FBZ and FBZ τ (blue line) as well as for FBZ and IBZ (red line). Each plot shows the temperature field difference along a line of control volumes in the z direction at various points along the xz -plane of the fin (plane in which the data points lie is outlined in red in the inset of Fig. 4.7).

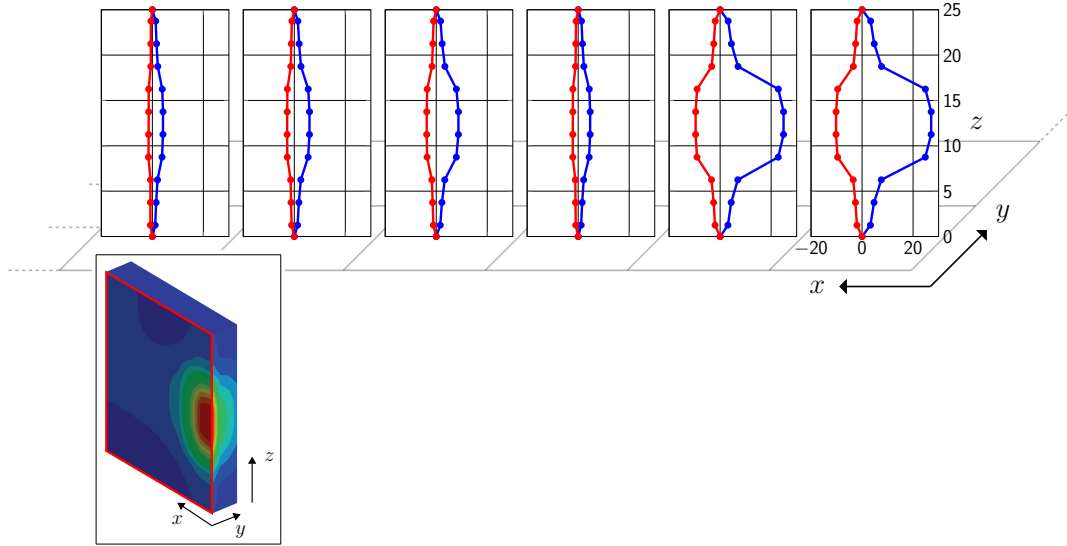


Figure 4.7: Percent difference in the cell centered temperatures of the FBZ and FBZ- τ models (blue) and the FBZ and IBZ models (red) for control volumes in the xz -plane of the FinFET. The xz -plane corresponding to the plots is outlined in red in the inset schematic.

The difference in temperature fields between FBZ and FBZ τ are found to be as large as 28.45% where FBZ τ has higher temperatures overall. Conversely, IBZ has lower temperatures than FBZ with difference in the temperature fields as large as 10.2%. The temperature difference predicted by the three solutions decreases further into the fin as scattering occurs and the transport becomes more diffusive. In the ballistic regime, however, the results show significant influence of anisotropy on thermal flows.

Temperatures from FBZ are generally lower than those from FBZ τ . This is due to the relatively smaller relaxation times in FBZ τ . The smaller τ resists phonon propagation by reducing the phonon MFP. Thus energy is less readily removed

from the source region in FBZ τ due to relatively more phonon-phonon scattering. However, temperatures from FBZ are larger than those from IBZ. This is partly explained by the non-dispersive nature of the gray phonon modes. As a result all gray phonon modes have non-trivial group velocities and therefore may contribute to thermal energy transport. Furthermore all phonons within IBZ have phonon MFPs of approximately 58.2 nm and therefore propagate ballistically within the fin, only experiencing resistive effects when undergoing diffuse surface reflections.

To further understand the temperature differences among the three models the respective phonon irradiation values are compared. The phonon irradiation, $H_{\hat{\mathbf{d}}}$, is a measure of the energy propagating in a direction $\hat{\mathbf{d}}$ per unit area per unit time and is defined

$$H_{\hat{\mathbf{d}}} = \sum_{\substack{\phi \in \Phi \\ \mathbf{v}_{\phi} \cdot \hat{\mathbf{d}} \geq 0}} e_{\phi}^0 \mathbf{v}_{\phi} \cdot \hat{\mathbf{d}}. \quad (4.3)$$

Thus the phonon irradiation may be viewed as a measure of the phonon flux in the ballistic regime which is a good approximation for phonon flow in the present system. The phonon irradiation is solely dependent upon the harmonic properties of the crystal. $H_{\hat{\mathbf{d}}}$ for FBZ and FBZ τ is equivalent as $H_{\hat{\mathbf{d}}}$ is independent of relaxation time which is the only difference between the two models. The values for the radiosity of IBZ and FBZ along the three principal spatial directions is given in table 4.6. Inspection of table 4.6 indicates phonons within IBZ carry more energy at a faster rate away from the source region compared to their FBZ counterparts resulting in relatively smaller temperatures in IBZ.

Anisotropic effects, which give rise to the temperature differences, are due to

$H_{\hat{d}}$	\hat{x}	\hat{y}	\hat{z}
IBZ	1.33	1.33	1.33
FBZ	1.12	1.10	1.12

Table 4.6: Radiosity of IBZ, FBZ, and FBZ τ along the principal direction, all values are in units of $10^{11} \text{ W}/m^2$.

the finite crystal lattice, as well as non-isotropic Brillouin-zone properties. These effects have been shown to have a significant impact on temperature fields as demonstrated by Fig. 4.7. However further work is required in understanding and quantifying the effect of all sources of anisotropy. Namely the effects of a finite number of carriers with different number of carriers along each direction producing lattice-scale anisotropy, microscale anisotropy in the Brillouin zone properties, and macroscopic anisotropy in non-cubic crystals.

4.1.0.3 Verification of FinFET Simulations

While the implementation of our numerical approach was verified in ch. 3, we desire additional confirmation that we are correctly modeling phonon transport within a FinFET. In order to ensure the veracity of our results we ensure the simulation results agree with physical intuition. Namely, one would expect that the peak temperatures in the parameter study should correspond to systems with the largest source energy density, this intuition is confirmed by table 4.4. Furthermore, as the conductivity tensors of all models have an equal trace one would expect the

temperatures predicted to agree at locations far from the Joule heating region [83]. This agreement of the model predictions is precisely what is observed in fig. 4.7, as we noted in sec. 4.1.0.2. Thus, we are confident that we are correctly solving the mathematical model *and* also capturing the full Brillouin zone effects as well as the nanoscale feature size effects on phonon flow.

4.2 Conclusion

The capability of simulating anisotropic thermal flow in three dimensional nanoscale devices was demonstrated through models of a three dimensional Fin-FET transistor. The presented results show that the influence of anisotropy can be significant; for the configuration studied in this work the differences in temperature solutions were found to be as large as 28.45%. Furthermore, it is observed that models that represent anisotropy in the crystal without anisotropy in the scattering result in larger errors than the fully isotropic model. Further studies are required to quantify the relative effects of all sources of anisotropy. However, it is clear that accurate thermal modeling in nanoscale devices require a full Brillouin-zone representation in order to capture important anisotropic effects on phonon flows.

Chapter 5: Phonon backscatter, trapping, and misalignment effects on microscale thermal conductance below the Casimir limit ⁴

Thermoelectric devices convert waste heat into electricity and therefore hold promise as maintenance free sources of clean energy at little cost to the environment [128, 129]. However, the low energy conversion efficiency of thermoelectric devices has been a stumbling block to their widespread acceptance. Thus significant opportunity exists for engineering more efficient thermoelectric devices. Improved efficiency could be realized through material selection and/or nano- and micro- scale feature design, ushering in an entirely new class of highly efficient thermoelectric devices. Among the promising candidates for improving thermoelectric efficiency are Si nanowires (NWs), which are garnering increasing attention as thermoelectric components due to their unique heat transfer properties.

In this chapter we study microscale thermal transport in Si NWs, identify-

⁴Portions of this chapter appeared in the publication: *F. G. VanGessel, P. W. Chung, Phonon backscatter, trapping, and misalignment effects on microscale thermal conductance below the Casimir limit, Int. J. Heat Mass Transfer, (2018), <https://doi.org/10.1016/j.ijheatmasstransfer.2018.09.028> [46]*

ing a specific NW geometry that improves thermoelectric efficiency. At nanometer to micron length scales, there exists a strong competition between phonon-phonon (intrinsic) and boundary (extrinsic) scattering mechanisms that fundamentally alters the thermal transport. Despite significant progress in demonstrating the ability to reach thermal transport behaviors below the Casimir limit, little appears to be understood about the competition between these scattering sources. In this investigation, we propose a simple one-parameter NW geometry that simultaneously modulates backscattering and trapping effects to enable directed study of these different means of controlling phonons. The geometry is a simple sequence of chambers offset from one another by a defined distance. We use the geometry to study the effects of phonon backscatter, trapping, and corner-turning on the thermal conductance in Si nanowires (NWs). We employ a the phonon BTE method, detailed in ch. 3, to determine spatially-varying phonon densities in the geometry. By creating a geometry that maximizes backscatter, a roughly 8-fold reduction in thermal conductance below the Casimir limit can be achieved at room temperature which is a factor of four smaller than the nearest reported value in the literature. The geometry is also useful for systematic investigation of other means of controlling phonons and affecting thermal transport; particularly, we investigate diffuse versus specular boundary scattering and the induced misalignment between the phonon flow and thermal flux due to the shape of the geometry. These effects offer new insights into fundamental phonon behaviors and possible routes toward phonon control.

5.1 Controlling Phonons in Nano- and Micro- structures

As the trend towards smaller, more powerful, and more efficient microelectronic and MEMs devices continues, high fidelity control over thermal energy transport continues to grow in importance for maximizing the performance of these devices. Advances in silicon-on-insulator technologies have made devices with nanoscale features smaller than 100nm commonplace [130]. Furthermore, while early nanostructures were primarily simple nanowires or thin films, it is now possible to engineer nanostructures with novel geometries that deviate significantly from those earlier designs. However, at the submicrometer length scale, classical boundary Brillouin zone-averaged scattering expressions, such as those derived in [131, 132], neglect phonon mode-level effects such as the propagation direction of individual phonon modes, an important mechanism in heat transport in nanostructures [103]. For example, Casimir predicted the mean free path of phonons within a cylindrical rod of diameter D were uniformly attenuated to $\Lambda = D$ [131]. This approximation neglects the range of phonon MFPs present in a material as well as the direction of propagation of individual phonon modes relative to the cylinder axis. Therefore, in order to utilize novel device geometries to engineer desirable thermal transport characteristics, a more complete understanding is required of how nanodevice geometries affect phonon transport, resist heat flow, and alter the carriers ability to conduct heat at the level of individual phonon modes. Many types of devices stand to benefit from the improved ability to engineer heat transport behavior including transistors, photodiodes, and thermoelectrics.

Research efforts to manipulate heat transport at small scales has brought considerable attention to phononic crystals, i.e. crystalline systems with an artificial secondary periodicity. Such crystals can be developed to have desirable heat transport properties such as a high degree of anisotropy, phononic band gaps, or reduced thermal conductivity. Three types of phononic crystal concepts are found in the present literature. One uses nanopillars [133] or nanodots [134] periodically arranged on structures. The additional features create nonpropagating vibrational modes which can trap thermal energy and reduce thermal conductivity. Another concept uses membranes patterned with periodically-arranged circular [135], square [136], hexagonal [137], and triangular [138] pores. The pores can obstruct phonon flow and thereby reduces thermal conductivity, enhances anisotropy of the heat flow, and in the coherent limit creates phononic band gaps. A third concept uses NWs with periodically modulated thickness [139] or irregular surface geometries such as sawtooth [110], corrugated [140], or fishbone [107] features that backscatter phonons or also create nonpropagating modes thereby leading to increased thermal resistance and reduced conductivity. All of these concepts are motivated by the potential to engineer desirable phonon behaviors using mechanisms that manipulate the way scattering occurs in the material. Efforts to combine concepts, such as pores and nanowires [109] and films and nanowires [141], have also shown some degree of efficacy.

A separate class of techniques for manipulating heat transport operates in a different MFP regime than is of current interest. Whereas we are primarily focused on long MFP phonons, approaches that modulate transport through control over

small MFP phonons using defects such as impurities [42], voids/vacancies [142], and dislocations [143], or superlattice constructions [144] have been pursued.

Tangential to studies of phononic materials, there has been the surge of interest in reducing thermal conductivity in materials for thermoelectric applications [19, 20, 107, 135, 140, 145]. Silicon nanowires (NWs) have gained increasing use as components of thermoelectric systems over the past 10 years due to their desirable thermal conductivity of $25 \text{ W m}^{-1} \text{ K}^{-1}$ [146] which is nearly an order of magnitude smaller than its bulk value ($\sim 156 \text{ W m}^{-1} \text{ K}^{-1}$ at 300K [147]). More recently studies have found that silicon NWs with roughened sidewalls may attain thermal conduction far below $10 \text{ W m}^{-1} \text{ K}^{-1}$, with conductivity as low as $1.6 \text{ W m}^{-1} \text{ K}^{-1}$ for a NW with 52 nm cross-sectional dimension at room temperature having been reported [19]. Therefore, the synergistic effect of rough NWs coupled with phononic features offers a possible route to achieving extremely low thermal conductivity devices.

Recent NW studies have shown that the net effects of phononic features on thermal conductivity can be significant. Blanc et al. experimentally studied corrugated Si NWs at low temperatures (0.3K - 5K) and found that corrugation resulted in thermal conductance of roughly half the Casimir limit at 1K [140]. Poborchii et al. studied corrugated Si nanowires at temperatures ranging from 300-400 K observing a 60%-70% reduction in κ for strongly corrugated wires at 300K [148]. Monte Carlo simulations indicated that the observed reduction in thermal conductance may be due to phonon trapping or backscattering within the corrugations. Several groups have studied NWs with periodically modulated thickness [107, 139, 149–153].

Based on the emerging findings, there is now strong evidence that backscattering or trapping plays some role in reducing thermal conductance from intrinsic bulk value. Yet, a careful study investigating the degree to which backscattering and trapping effects reduce thermal conduction does not appear to be available presently. In the remainder of this chapter we develop a parametric model for systematically altering a Si NW geometry in order to study the phonon transport properties as we approach the limit of zero thermal conduction. The *Casimir limit* for minimum thermal conductivity refers to the theoretical minimum limit where all phonon MFPs are attenuated to the characteristic dimension of a microscale device (i.e. the diameter of a NW). Our goal is to study thermal transport below the Casimir limit, which arises due to variations in the device dimensions. Namely, we wish to ascertain whether thermal conductivity can be substantially reduced below the Casimir limit in NWs with simple boundary modifications using the interplay and competition between boundary and intrinsic scattering mechanisms. We examine the interactions of backscatter and constriction and attempt to isolate these from the effects of intrinsic, i.e. phonon-phonon, scattering. For the sake of future experimental fabrication ease and potential three dimensional device designs, we avoid interior scattering features such as in [135–138] and instead favor a nanowire-like domain composed of short NW sections, or chambers, offset from one another. The offsets cause periodically-spaced regions where increased backscattering occurs. Phonons must flow around obstructions, creating regions of misalignment between the phonon flux and the macroscopic temperature gradient. Furthermore, large offsets, relative to the NW cross-section, produces constriction effects that lead to a greater degree

of phonon trapping, or when a phonon undergoes multiple backscattering events within a single chamber before exiting. In contrast to previous studies showing reductions in thermal conductivity of 35-70% compared to the uniform NW of same cross-section area [107, 110, 148, 154, 155], we find that backscattering and trapping are the dominant mechanisms for reducing transport and can alone achieve reductions over 90%. The increased backscatter shifts the degree to which individual modes participate in thermal transport, and serves as a filter for modes of a certain mean free path. Wires with rough sidewalls allow phonons to more easily realign with the macroscopic temperature gradient and flow around offsets. Approaches that do not maximize backscattering produce smaller reductions in conductance.

The outline of this chapter is as follows. The chamber-offset NW and its geometrical parameters are defined in sec. 5.2.1. Section 5.2.2 describes the methodologies used for ray-tracing and three dimensional full Brillouin zone Boltzmann transport models. Section 5.3 presents the modeling results for NW thermal conductance as well as the analyses of the fundamental mechanisms leading to the reduction in phonon transport. Finally, in Section 5.4 we provide our concluding remarks.

5.2 Methodology

5.2.1 Model Geometry

We use Si NW models in this paper. These are composed of cubical chambers with an offset between adjacent chambers. A section of the geometry is shown

in Figure 5.1 with \hat{x} as the transport direction. The chamber-offset is composed of a periodically repeating segment (indicated by the dash line box), with period $\mathbf{T} = W\hat{x} + H\hat{y}$ where W is 50nm and H is the free parameter varied from 0nm to 40nm. Thus the area through which phonons may flow between adjacent chambers is $W \times (W - H)$. NWs of both infinite and finite (450nm) length are studied. These dimensions are in contrast to previous experimental studies which considered NWs with cross sectional areas ranging from 20nm x 20nm to 196nm x 550nm and lengths ranging from $1.7\mu\text{m}$ to $18.8\mu\text{m}$ [156–158]. When $H = 0$ the geometry

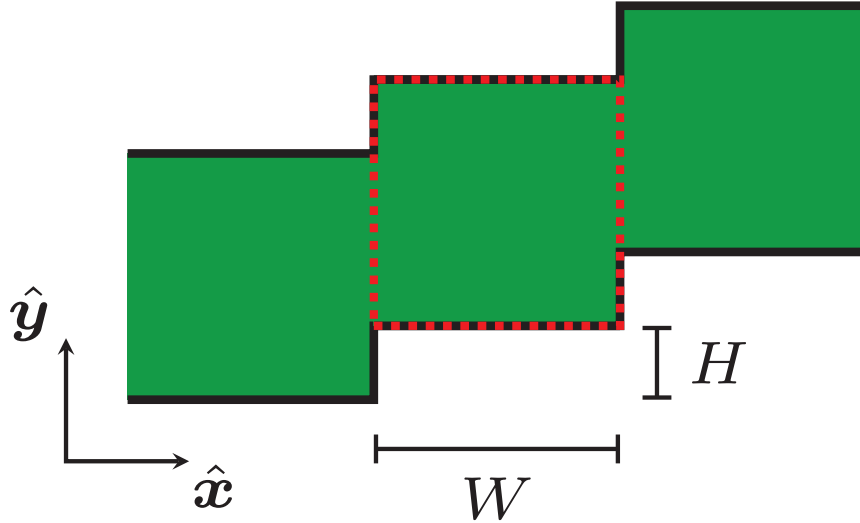


Figure 5.1: Finite section of chamber-offset NW geometry. The red dotted area denotes a single *chamber*.

reduces to straight uniform wire with square cross-section. This case provides the reference transport properties. A vertical surface is introduced for any value of $H \neq 0$, which promotes phonon backscattering leading to a reduction in thermal conductance. The backscattering increases thermal resistance even when reflections

at the sidewalls are purely specular. The inlet is the face on the left, normal to the x -axis, and the outlet is the opposite face on the right. Despite this nomenclature, phonons can leave through either the inlet or the outlet. Furthermore, we rigorously define backscattering as any scattering event in which the component of the phonon group velocity aligned with the macroscopic temperature gradient changes sign. Thus while backscattering is most often associated with a resistive scattering event, it can, on occasion, lead to an increase in thermal conductivity i.e. when phonons are "forward" scattered toward the outlet.

The phonon scattering mechanisms that are presently considered include boundary scattering and intrinsic phonon-phonon scattering. Sidewall scattering can be either diffuse or specular. This distinction is important because when a significant portion of phonon modes have an intrinsic phonon MFP that exceeds the limiting dimensions of the NW, transport becomes semi-ballistic and the type of boundary scattering plays a significant role in thermal transport [112]. For the temperature and length scales under consideration, scattering of phonons at boundaries is expected to be largely diffuse [112]. However, in this study specular and diffuse sidewalls are both considered as they represent the respective minimum and maximum effects of boundary scattering on thermal resistance. These conditions will allow us to separately *i*) capture the extremal values attainable in the thermal conductance in the presence of strong boundary scattering, and *ii*) study the combined contribution of phonon backscattering and Umklapp scattering to thermal resistance when the sidewall reflections are specular.

5.2.2 Modeling Approach

5.2.2.1 Ray Tracing

In order to study a limiting case in which backscattering is the only resistive mechanism, we use a simple ray-tracing method with Monte Carlo sampling with specular boundary scattering and no intrinsic phonon-phonon scattering. The calculation entails counting particles that pass through a finite region of the chamber-offset NW using the gray model Brillouin zone with isotropic phonon velocities. Each ray incident on the boundary undergoes specular reflection, as defined in Sec. 3.3.3. In addition to the boundaries depicted in the model, specular reflection conditions are applied on faces normal to the \hat{z} -axis. Thus, although the geometry of the NW is 3D, the thermal transport behaviors in the specular boundary scattering limit can be observed in two dimensions, namely the $\hat{x}\hat{y}$ plane. The steps to perform the ray-tracing are as follows. For a given number of chambers, N_c , we introduce a ray, representing a phonon wavepacket, at the inlet. The initial location and propagation direction of the ray is drawn from the uniform distribution between $[0, W]$ and $[0, \pi]$ respectively. We then track the ray, specularly reflecting at any boundaries it encounters, until it exits the nanowire. An example simulation domain for $N_c = 3$ and $H = W/5$ is shown in Figure 5.2. For each simulation the flux reduction relative to the $H = 0$ case, f^{red} , is calculated as:

$$f^{red} = \frac{\text{number of rays reaching the outlet}}{\text{total number of rays simulated}}. \quad (5.1)$$

The number of rays simulated is set to 10^5 .

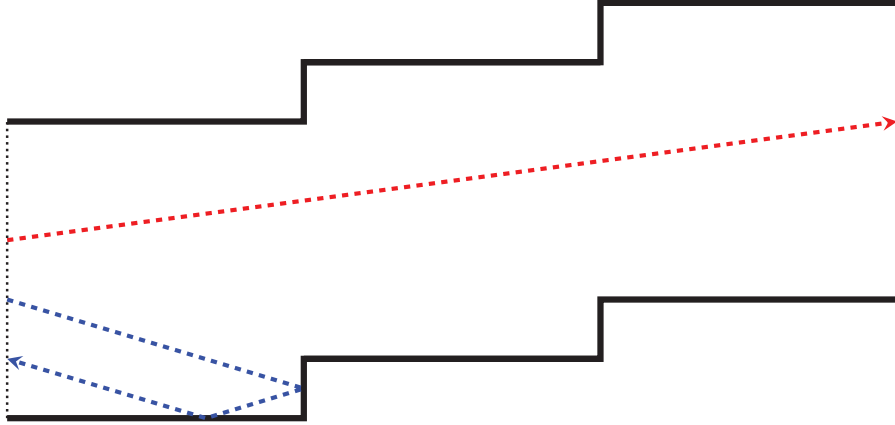


Figure 5.2: Ray tracing through a chamber-offset NW. The red ray contributes to the flux through the wire, however the blue ray experiences a backscattering event and therefore does not increase the total flux.

5.2.2.2 Phonon BTE

The full Brillouin zone three-dimensional phonon Boltzmann Transport Equation (FBZ-BTE) is solved using the method outlined in chapter 3 to account for the combined effects of diffuse/specular sidewall boundary scattering and intrinsic phonon-phonon scattering on the thermal conductance. Variants of this FBZ-BTE method has been previously used to investigate internal phonon flow in nanobeam "labyrinths" [154] as well as external phonon flow in nanoporous Si thin films [111,138,153]. Furthermore, the FBZ-BTE captures anisotropy in the phonon transport which would otherwise be neglected in simpler approaches that employ a grey or Debye approximation or where the 3D Brillouin zone is spherical. Anisotropy in phonon transport has been shown to cause a 25% difference in thermal conductivity predictions for thin silicon films, when compared to simulations using an isotropic

Brillouin zone [102], indicating the importance of using an FBZ model when simulating phonon transport within nanostructures. For this work we use a uniform sampling of 16,518 phonon modes from the full Brillouin zone, thus inherently capturing ballistic anisotropy of the phonon transport. In addition, we simulate phonon transport only for acoustic phonons, assuming the contribution of acoustic phonons to thermal transport dominates over that of optical phonons. However, we use the phonon relaxation time parameterization taken from [159], which accounts for acoustic-optical phonon scattering processes. Note that it has been shown that in nanostructures optical phonons may contribute 15-20% of the total thermal conductivity [160, 161], compared to only 5% in a bulk system. Therefore, we expect inclusion of optical phonons will have a non-negligible effect on the calculated conductivities and conductance. However, rough estimates show that including the optical phonon contributions will not change our fundamental conclusions. The phonon parameters used for all results reported here are generated in the manner described in 3.3.4 using a Si interatomic potential [162]. The simulation results reported in sections 5.3.2-5.3.3 discretize the spatial domain using 27,000 control volumes while the results in Sec 5.3.4 use 72,000 control volumes.

Solution of the phonon BTE yields the spatial variation of the modal phonon energies over the entire domain, i.e. $e_\phi(\mathbf{r})$. From these energies, the mode flux \mathbf{f}_ϕ and total heat flux \mathbf{f} can be determined from

$$\mathbf{f}_\phi = \mathbf{v}_\phi e_\phi \ ; \ \mathbf{f} = \sum_{\phi} \mathbf{f}_\phi \ . \quad (5.2)$$

The thermal conductivity can then be estimated based on Fourier's Law using

the total flux, the applied temperature difference, and the length of the NW. The definition of conductivity is therefore

$$\kappa = \frac{fL}{\Delta T} \quad ; \quad L = \sqrt{W^2 + H^2} \quad , \quad (5.3)$$

where $f = |\mathbf{f}|$. In the classical definition of conductance $G = \kappa A/L$, leading to the conductance definition

$$G = \frac{fA}{\Delta T} \quad . \quad (5.4)$$

5.2.2.3 Boundary Conditions

Four types of boundary conditions (BCs) are used in the simulations - periodic, applied temperature, specular reflection, or diffuse reflection. The inlet and outlet are assumed to be either periodic with respect to the phonon deviation from equilibrium, or in equilibrium with a heat bath of specified temperature. Periodic BCs are used to model the limiting case when the NW is infinitely long. Applied temperature BCs are used when the boundary is affixed to a heat bath with negligible thermal boundary resistance, analogous to an experimental set-up in which the nanowire is directly integrated with the heating and sensing pads during fabrication [130], such as those studied in [19, 145]. The side walls are assumed to be adiabatic with the phonon scattering to be either specular or diffuse. Specular BCs assume each phonon undergoes a specular reflection at the NW sidewall, while diffuse BCs assume all phonons are perfectly thermalized at the local temperature of the sidewall. NWs with specular or diffuse BCs will be referred to as smooth NWs or rough NWs respectively. The boundary conditions are applied according

to the approach outline in sec. 3.3.3. In the case of an infinite NW, the periodic translation vector is set to be $\mathbf{T} = W\hat{\mathbf{x}} + H\hat{\mathbf{y}}$

5.3 Results & Discussion

Four sets of results are presented in this section. The first is based on ray-tracing which is a limiting case of a finite-length conductor with only backscattering and no intrinsic scattering. The second is another type of limiting case where the NW is infinite in length, modeled using periodic boundary conditions, but both effects of intrinsic and extrinsic scattering effects are included. The third set of results examines interior phonon flow and how readily phonons turn the offset corner in the smooth and rough infinite NWs. The fourth set studies an experimentally achievable NW of finite length where applied temperature conditions are applied to the ends of the NW.

5.3.1 Backscatter in smooth NW: limiting case 1

Five sets of simulations are performed with offsets of $H = \{W/5, 2W/5, 3W/5, 4W/5\}$ and N_c ranging from 2 to 40. Shown in Figure 5.3 is the flux reduction, f^{red} , against $1/N_c$. The case where $H/W = 0$ corresponds to a straight NW without any offset. In this case, and as a consequence of ray-like behavior where all surface scattering is specular, there exists no resistance to the rays and $f^{red} = 1$. For $N_c = 2$, the single offset leads to a bottlenecking effect which backscatters a fraction of the phonons equal to H/W . Only those phonons that successfully traverse the

constriction contribute to the flux, while those that backscatter do not. However, for $N_c > 2$ the effect of the chamber-offset geometry grows more complicated. Phonons may experience multiple backscattering events, reversing the x-component of their momentum each time. Increasing the number of chambers always decreases the overall flux.

With increasing offset size, the likelihood of a phonon becoming trapped increases, leading to a reduction in flux. Inspecting fig. 5.3 reveals that f^{red} is highly correlated to the inverse of N_c , i.e. the relationship is close to linear. Increasing the number of chambers decreases the overall flux. Also plotted in Figure 5.3 the flux reduction f^{red} , which we determine to be

$$f^{red} \left(\frac{H}{W}, N_c \right) = 0.33 + \frac{1.38}{N_c} - 0.36 \frac{H}{W} - 1.35 \frac{H}{W} \frac{1}{N_c} \quad (5.5)$$

The rate of convergence to the infinite wire behavior is larger when H is larger. The $N_c \rightarrow \infty$ limits, obtained from the intercepts on the vertical axis, are shown in Table 5.1. These indicate that, in the limit of an infinitely long NW, the phonon backscattering effect is capable of reducing phonon flux by 75% to 96% for offset height ranging from $W/5$ to $4W/5$. Furthermore, as shown in Table 5.1, the average distance a phonon travels along the x-axis between phonon backscattering events is reduced from infinitely long for the straight NW to 58 nm for $H/W = 4/5$. In addition, as the offset height increases the number of backscattering events a phonon undergoes within a single chamber increases from 0.6 - 11.8. This indicates the strong degree of phonon trapping leading to a crossover from propagating to non-propagating phonon modes. The results suggest that simple designs that exploit

surface scattering and backscattering mechanisms at the length scale of the carrier MFP offer the ability to significantly decrease heat flux.

H/W	0/5	1/5	2/5	3/5	4/5
Phonon flux reduction	1.00	0.25	0.18	0.11	0.04
Avg. MFP along x -direction [nm]	∞	292	135	84	58
Avg. # of backscattering events per chamber	0.0	0.6	1.9	4.2	11.8

Table 5.1: Ray-tracing statistics for phonon flux reduction, MFP and, backscattering in infinite chamber-offset NW.

5.3.2 Backscatter in smooth and rough NW: limiting case 2

When device dimensions are at submicron scales, scattering from material surfaces may be more diffuse than specular. Here, we solve the FBZ-BTE using periodic boundary conditions to model the case of a NW of infinite length accounting for both specular and nonspecular scattering as well as intrinsic scattering. The latter is modeled using the relaxation time approximation with parameters from [159]. Periodicity, as described earlier, is in the deviation of phonon energy from the equilibrium value at the inlet and outlet. Thus, for a given N_c , a thermal gradient is imposed by specifying temperatures at the inlet and outlet. This simulates the phonon behavior in an infinite system while eliminating any edge effects due to the finite length of the NW simulation. The temperature values used here are

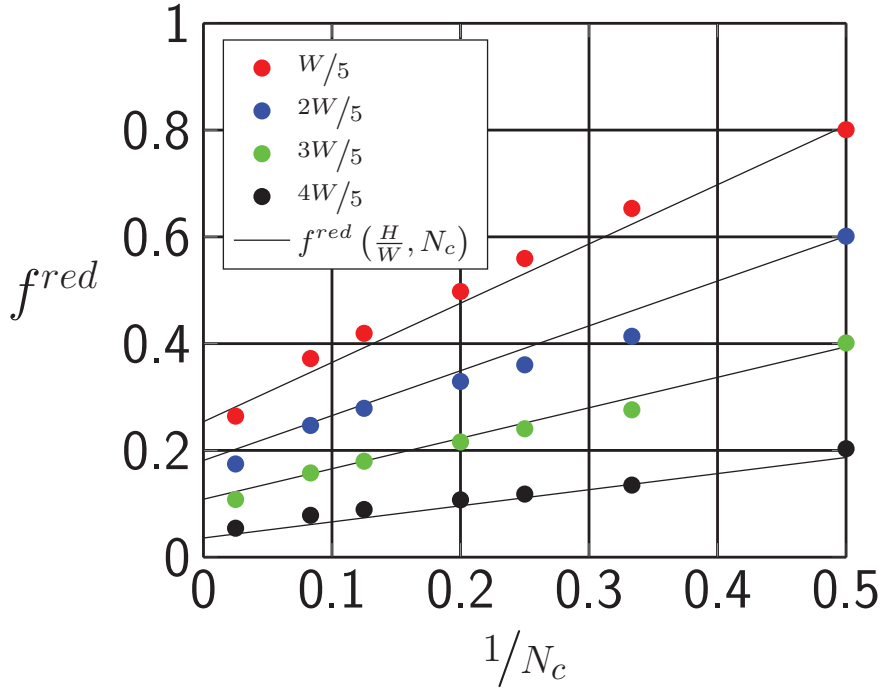


Figure 5.3: Relative reduction of flux through chamber-offset wire vs the inverse of the number of chambers for a range of offset heights. The linear model equation is given in Eq. 5.5

$T(\mathbf{r}_0) = 304\text{K}$ and $T(\mathbf{r}_L) = 306\text{K}$, respectively. The effectiveness of the chamber-offset geometry in reduced thermal transport may be quantified as the ratio of conductances using the conductance for $H = 0$ as the reference. Note that the use of periodic boundary conditions imply an infinitely long NW conductor. Furthermore, according to eq. 5.3 the effective thermal conductivity is $\kappa = fL/\Delta T$. Therefore it would seem that the conductivity will go to zero in the $L = \infty$ limit or at the very least the conductivity is dependent on the size of the simulation domain. It is perhaps better to think of the conductivity as the ratio of flux to temperature gradient, ∇T , which we approximate as $\Delta T/L$. The flux is linearly related to the

temperature gradient, i.e. the temperature gradient is the "driver" and the resulting flux responds linearly. Thus the thermal conductivity is a constant value regardless the choice of ΔT and L , making the quantity unambiguous. The conductance, however, is an extrinsic quantity inversely proportional to system length as given by eq. 5.4, $G = \kappa A/L$. However, when taking the ratio of two conductance values the length, the effect of NW length as a common factor is removed. Therefore, while we report absolute thermal conductance values as it is a readily experimentally measurable quantity, the extrinsic nature should be noted.

The results in Figure 5.4 show the relative reduction of conductance with respect to the offset height. In the specular case the only resistive mechanisms to heat flow are phonon backscattering and the intrinsic phonon-phonon scattering, and we find the relative reduction in thermal conductance ranges from 89-99% for $H \in [W/5, 4W/5]$. Note that while the BTE simulations predict an 89% reduction in thermal conductance for $H=W/5$, the earlier ray-tracing algorithm predicts a 75% reduction in the infinite wire limit. The difference of 14% is due to the increased role of intrinsic phonon-phonon scattering. Although phonon-phonon scattering is present in the reference case, G_0 , it has a larger effect for $H > 0$ where phonons traversing between chambers, on average, travel a farther distance than when $H = 0$ due to multiple backscattering events (see Table 5.1). The longer effective path length of phonons means the material appears more *acoustically thick*, leading to more intrinsic scattering events and a reduction in thermal transport. For wires with diffuse sidewall scattering we observe a 65-95% relative reduction in the thermal conductance for $H \in [W/5, 4W/5]$. This reduction is smaller than the specular

case because the thermal resistance due to diffuse scattering is independent of offset height H . Therefore the relative contribution of phonon-phonon scattering and phonon backscattering to the total thermal resistance is reduced in the diffuse case. The downward trend of $G(H)/G(0)$ as additional resistive mechanisms are introduced into the system is consistent with the observed phonon transport behavior in S-shaped chicane structures [163]. In that case, the characteristic length scale of the structure was in micrometers, placing the transport well into the diffusive regime. Bourgeois et al. observed that the difference in measured conductivity between serpentine and straight wires is small, as the smaller Knudsen number allows the phonons to turn corners readily. Therefore, the striking reduction in thermal conductance is in large part due to the ballistic nature of phonon transport within the chamber-offset NWs. Previous attempts to increase thermal resistance through geometric modifications of a NW have achieved a wide range of conductivity reductions with respect to a uniform NW. At room temperature, and for similar NW dimensions considered in this work, the largest reduction achieved was 60-70% [148], which is less than the reduction in the chamber-offset NW for $H \geq 2W/5$.

Thermal conductance and conductivity for both diffuse and specular reflecting walls are shown in Figure 5.5. In the limiting case of $H = 0$, the predicted thermal conductivity, $\sim 22 \frac{\text{W}}{\text{m}\cdot\text{K}}$, compares well with experimental results of NWs with similar cross-section area, $\sim 25 \frac{\text{W}}{\text{m}\cdot\text{K}}$ [146] and $\sim 17.5 \frac{\text{W}}{\text{m}\cdot\text{K}}$ [148]. Whereas conductivity is an intrinsic property, the conductance is an extrinsic property. But to provide an estimate of the transport that factors in the extrinsic effects due to the smaller effective NW area, we estimate its value in the context of a NW of infinite

length by substituting the definition of conductivity based on Fourier's Law. The definitions for the conductivity and conductance are given in Eqs 5.3 and 5.4 respectively. Figure 5.5.b also shows the comparison between the estimated conductivity and the Casimir limits predicted for straight diffuse nanowires whose rectangular cross-section has areas equivalent to the reduced area associated with the bottlenecking dimension, $W - H$. The Casimir limit represents the diffuse boundary

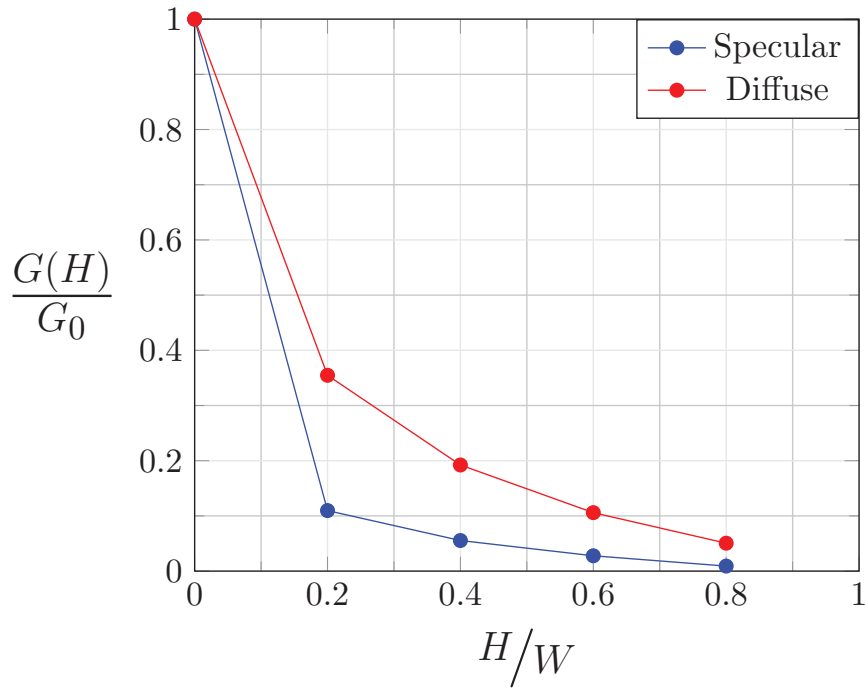


Figure 5.4: Relative reduction of thermal conductance of chamber-offset NW versus offset height. Both a NW with specular (blue) and diffuse sidewalls (red) are considered.

scattering limit in which phonon MFPs are limited by the NW dimensions, i.e. for a square cross section NW, $\Lambda_{\phi}^{casimir} = 1.12W$ [131]. This theoretical limit assumes all phonon mode MFPs are the same and does not account for the direction of prop-

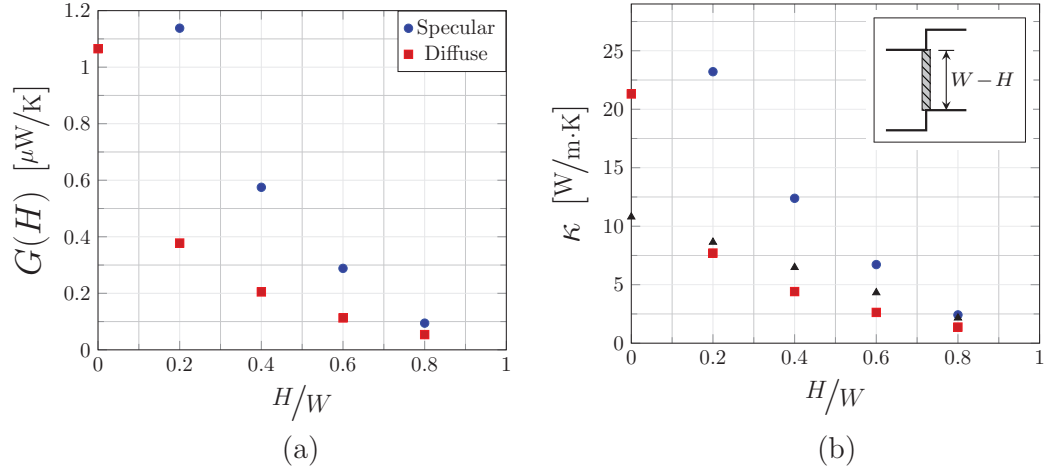


Figure 5.5: (a) Thermal conductance of chamber-offset NW versus offset height. Both a NW with both specular (blue) and diffuse sidewalls (red) are considered. (b) The thermal conductivity values for the chamber-offset NW vs. offset height. The grey triangles represent the Casimir limit prediction for the thermal conductivity for a straight NW with square cross section of width $W - H$. The specular case for $H = 0$ is neglected as this corresponds to the bulk Si value.

agation, branch, or dispersion. Thus it should serve as a reasonable lower bound to the thermal conductivity when the NW is straight (i.e., $H = 0$). This is the cause for the difference between the BTE prediction and Casimir values when $H = 0$ in Figure 5.5b. For $H > 0$, the conductivity of the diffuse wire estimates are smaller than the Casimir limit while the specular wire is larger. This observation holds despite using the smaller area associated with the bottlenecking dimension, $W - H$, in the Casimir limit calculation. Therefore, not only does the chamber-offset result in a lower κ than the equivalent area straight NW, it has lower κ than straight

NWs with dimensions equal to the height at the bottleneck $W = H$. This indicates that introducing features that promote backscatter and trapping is more effective at disrupting thermal transport than reducing the straight NW cross-section.

In order to investigate how backscattering affects the mobility of individual modes, Figure 5.6 shows the thermal conductance accumulation function $G^{accum}(\Lambda^*)$.

The thermal conductance accumulation is defined as

$$\bar{f}_\phi = \frac{1}{V} \int_{\Omega} f_\phi dV ; G^{accum}(\Lambda^*) = \frac{1}{G} \frac{A}{\Delta T} \sum_{\Lambda_\phi \leq \Lambda^*} \bar{f}_\phi . \quad (5.6)$$

A significant change in $G^{accum}(\Lambda^*)$ occurs going from $H = 0$ to any $H \neq 0$. This is

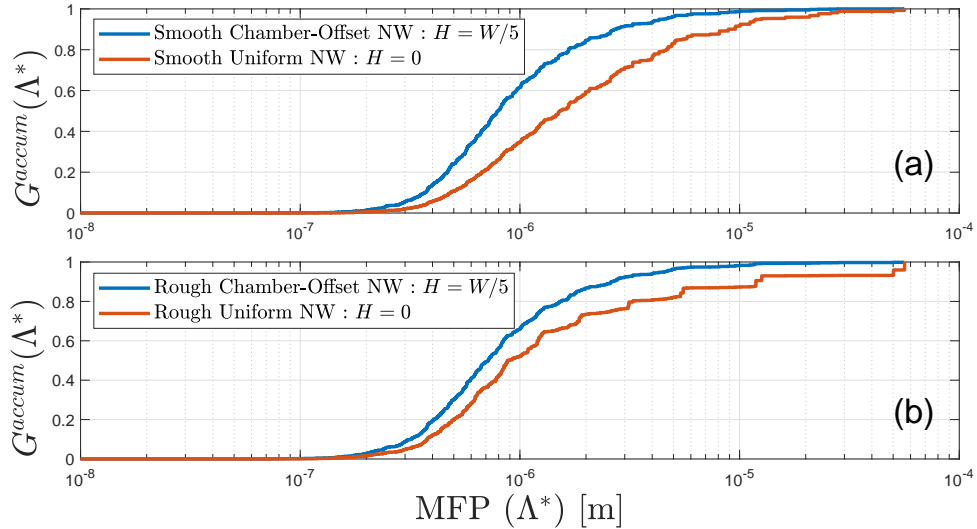


Figure 5.6: Thermal conductance accumulation for (a) smooth and (b) rough NWs.

because the phonon modes with smaller MFP contribute relatively more to thermal transport when H is finite than when $H = 0$. In fact, phonons with a MFP less than $1 \mu\text{m}$ carry $\sim 83\%$ more energy in the smooth NW, $G^{accum}(1\mu\text{m}) = 0.64$, than in the bulk where $G^{accum}(1\mu\text{m}) = 0.35$. This significant increase is due to

the resistive effect of backscattering on long MFP phonons. When $H = 0$, the only resistive effect present is from phonon-phonon intrinsic scattering. Unlike the phonons in the uniform NW geometry that do not backscatter, the phonons in the chamber-offset NW can travel no farther than 250 nm (for $H = W/5$) along the x-axis before backscattering. Note that G^{accum} is on a normalized scale and therefore the conductance when $H = 0$ is still larger than when H is finite, as shown in Figure 5.5. For the rough NW case, shown in Figure 5.6b, the difference between the uniform NW and the chamber-offset NW is less pronounced, relative to that observed in smooth NWs, due to the presence of diffuse boundary scattering in each. The diffuse boundary scattering is a resistive mechanism which more strongly affects long MFP phonons. However, there remains a significant difference in G^{accum} due to the presence of phonon backscattering in the chamber-offset NW. Notably, phonons with a MFP less than 1 μm carry $\sim 23\%$ more energy in the chamber-offset NW, $G^{accum}(1\mu\text{m})=0.70$, than in the uniform NW where $G^{accum}(1\mu\text{m}) = 0.57$. A similar shift of the thermal conductivity accumulation curve was observed in silicon NW "labyrinths" studied in [154]. The shift to smaller phonon MFPs was less pronounced in that work as larger NW dimensions led to a greater amount of diffusive phonon transport. The chamber dimension introduces an additional physical length scale when $H > 0$ that limits carriers with longer path lengths. This manifests as the chamber-offset NW behaving as a high-pass filter. A high-pass filter is a device which attenuates the portion of a signal corresponding to low frequencies while allowing high frequency signal to pass. As phonon frequency is highly correlated with small MFPs, the chamber-offset NW can also be viewed as a

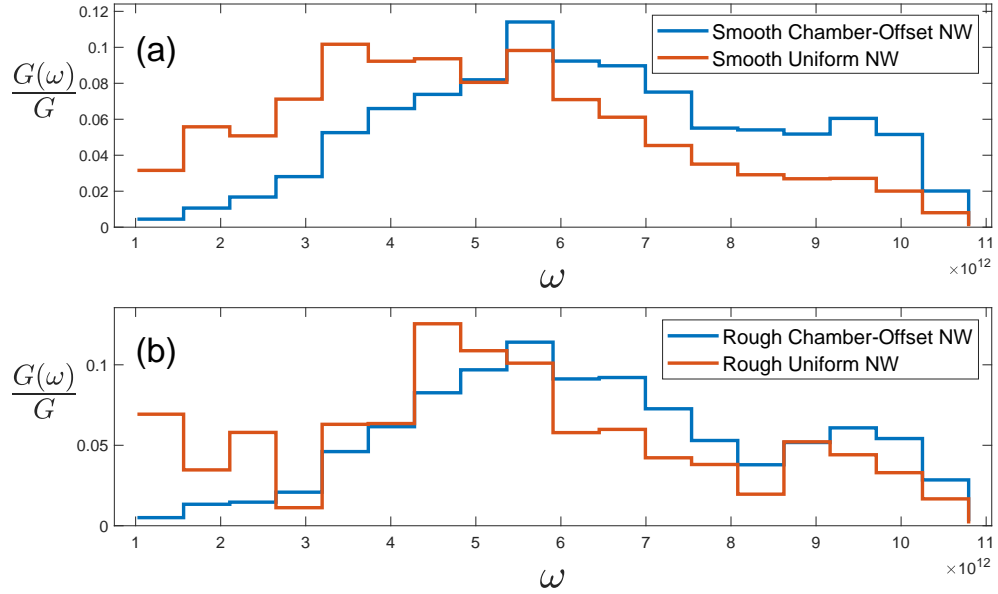


Figure 5.7: Relative contribution to thermal transport from discrete regions of frequency spectrum in (a) smooth and (b) rough NWs.

low-pass filter on phonon MFPs. The normalized contribution to thermal transport as a function of frequency is depicted as a histogram in Fig. 5.7. In the ordinate axis, the frequency-dependent conductance is calculated for each point in the Brillouin zone. Then modes within a defined frequency interval are placed in the same bin and the final bin populations are plotted, i.e.

$$\frac{G(\omega)}{G} = \frac{1}{G} \sum_{\{\phi: \omega_\phi \in [\omega - \Delta\omega, \omega + \Delta\omega]\}} \frac{f_\phi A}{\Delta T}. \quad (5.7)$$

The bin sizes, $[\omega - \Delta\omega, \omega + \Delta\omega]$, are chosen to reduce the noise stemming from discrete Brillouin zone sampling.

The filter reduces thermal transport due to lower frequency phonon modes which results in a larger proportion of the thermal energy being carried by the higher frequency modes. This is seen by the overall rightward shift of the histograms in

Fig. 5.7. The dips in $G(\omega)/G$ in Fig 5.7b at 3 and 8 THz correspond to situations where, for a given frequency interval, a greater proportion of phonons are traveling in directions not aligned with the macroscopic temperature gradient.

5.3.3 Smooth vs. rough NW: flux misalignment

The ray-tracing and BTE simulation results demonstrate that the chamber-offset NW resists thermal transport by backscattering phonons. The phonon backscattering effect creates a non-zero angle between the local heat flux, \mathbf{f} , and the global temperature gradient, $\nabla T = \Delta T(W\hat{\mathbf{x}}+H\hat{\mathbf{y}})/L^2$. It has been shown that an increase in this angle coincides with a reduction in thermal conductivity [135, 137]. The misalignment effect is most noticeable in the ballistic transport regime where absence of intrinsic scattering prevents phonons from easily turning corners created by the offset. Therefore, we consider the degree of misalignment between the local flux and global temperature gradient, comparing the ease with which phonons turn the offset corner in diffuse and specular NWs. The flux-weighted angle measures the degree to which local heat flux is oriented along the direction of ∇T and is effectively an indicator of the ability of the phonons to realign along ∇T ,

$$\theta_{fw}(\mathbf{r}) = \frac{f(\mathbf{r})}{f_{tot}}\theta(\mathbf{r}) . \quad (5.8)$$

Where $\theta(\mathbf{r})$ is the angle between \mathbf{f} and ∇T , $f(\mathbf{r})$ is the local flux magnitude, and $f_{tot} = \int_{\Omega} f(\mathbf{r})dV$ is the total NW flux magnitude. We use the flux weighted angle, rather than the local angle itself, as we deem it a better measure of resistance to thermal transport. This is because while the local angle may be large, say in the

chamber corner, the local flux contribution is negligible. Therefore, we require both the local flux *and* the local angle to be large in order to say that thermal transport has been disrupted by the chamber-offset geometry.

To quantify how the phonon flux orientation varies with respect to the offset location consider the flux misalignment.

$$\theta'(x) = \int_{\Gamma_x} \theta_{fw}(\mathbf{r}) dA . \quad (5.9)$$

The flux misalignment represents the integrated flux weighted angle within the $\hat{y}\hat{z}$ plane located at x , Γ_x , shown in figure 5.8.e. A larger value of θ' indicates a greater number of phonons are traveling in a direction different from that of the global temperature gradient at a given location x . Plots of θ' for specular, θ'_s , and diffuse, θ'_d , NWs and $r > 0$, where $r = H/W$, are shown in Figure 5.8.

From Figures 5.8a-c, when $r \leq 3/5$ we see that $\theta'_d < \theta'_s$, but the behavior is reversed when $r > 3/5$. In the former regime, the dominant resistive mechanism is backscattering, while in the latter, the dominant mechanism is trapping. The competing effects of backscattering and trapping can be seen in Figure 5.9 where for small values of r , θ_{fw} is at a maximum directly in front of and behind the offset, while when $r \rightarrow 1$ the maximum value occurs in the constriction. The transition between the backscattering and trapping mechanisms can be understood, in part, as a result of increasing the effect of the constriction such that the critical dimension, i.e. $W - H$, is small enough to capture the majority of carriers, even those with smaller MFPs. Diffuse boundary scattering takes the energy of an incoming phonon and redistributes that energy to all outgoing modes. In the rough NW, at smaller

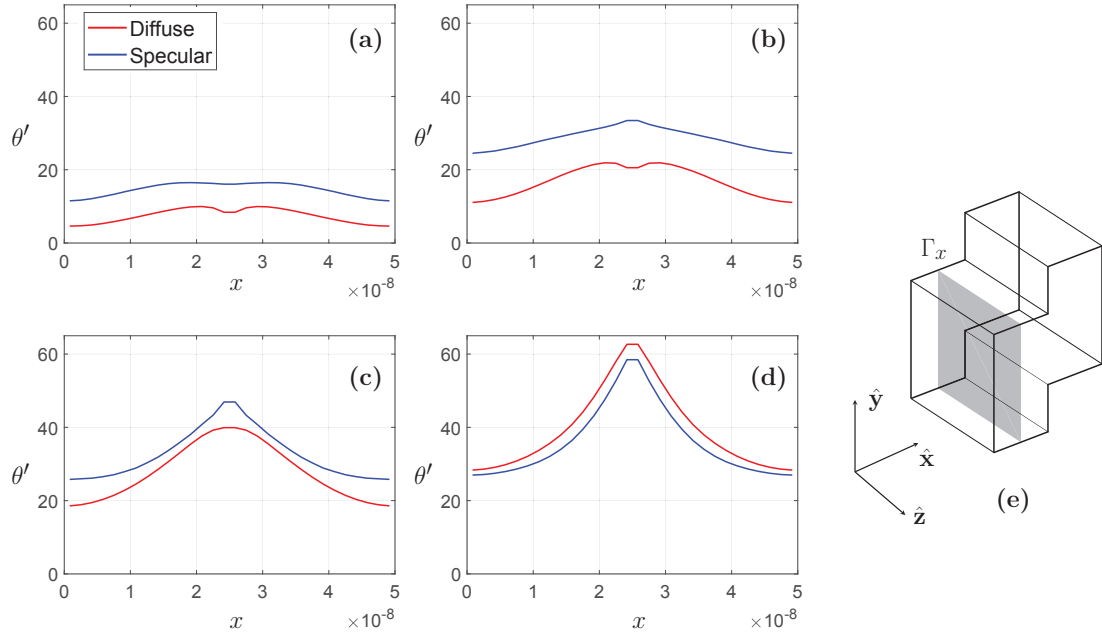


Figure 5.8: Plots of the flux misalignment, θ' , for r values (a) $r = 1/5$, (b) $r = 2/5$, (c) $r = 3/5$, and (d) $r = 4/5$. The plane Γ_x is shown as the shaded area in (e).

r , there is relatively less of an effect of the constriction and the phonons can more readily flow around the corner due to the diffuse boundary scattering. Specifically, energy in phonon modes misaligned with respect to ∇T is redistributed into modes more closely aligned with ∇T via the thermalization that occurs at diffuse boundary surfaces. But when the constriction is small enough, even the redistribution effect is overshadowed by the bottleneck that occurs between chambers. In this regime, phonons spend the majority of time propagating within a single individual chamber with a small fraction of phonons occasionally leaking into adjacent chambers. Regardless of whether the system is in the trapping or backscattering regime, the flux misalignment is largest at the corner and decreases to a minimum at the center of the chamber.

Figures 5.8a and 5.8b also show small depressions in θ'_d near the midpoint of the rough NW. This is indicative of a regime in which phonon backscattering is the dominant resistive mechanism. In this regime θ_{fw} is at a maximum in front of and behind the offset and therefore the maximum flux misalignment is slightly displaced from the center of the constriction. Conversely, in the phonon trapping regime θ_{fw} is largest in the constriction. The phonon backscattering regime can be seen in Figure 5.9a and Figure 5.9b while the trapping regime is evident in Figure 5.9c and Figure 5.9d. The transition from the backscattering to trapping regime occurs more quickly in the specular NW where the formation of a band of larger θ_{fw} can already be seen forming in the constriction of the NW in Figure 5.9b. The slower transition in the rough NW is at least partly due to the corner-turning effect which reduces phonon trapping to some degree. Thus, the chamber-offset geometry allows the study of the two competing mechanisms, backscattering and trapping, using a single parameter r . The magnitude and location of the largest flux misalignment varies due to the competing resistive effects of the two regimes.

5.3.4 Finite length nanodevice

To study finite length effects, we consider two geometries composed of 9 chambers. The two geometries are shown in Figure 5.10. Both variants are inspired by, but distinctly different from, the chamber-offset infinite NW. The difference lies primarily in the number of characteristic lengths in each geometry. The first variant (v1) contains three length scales - the total device length, the chamber size, and the

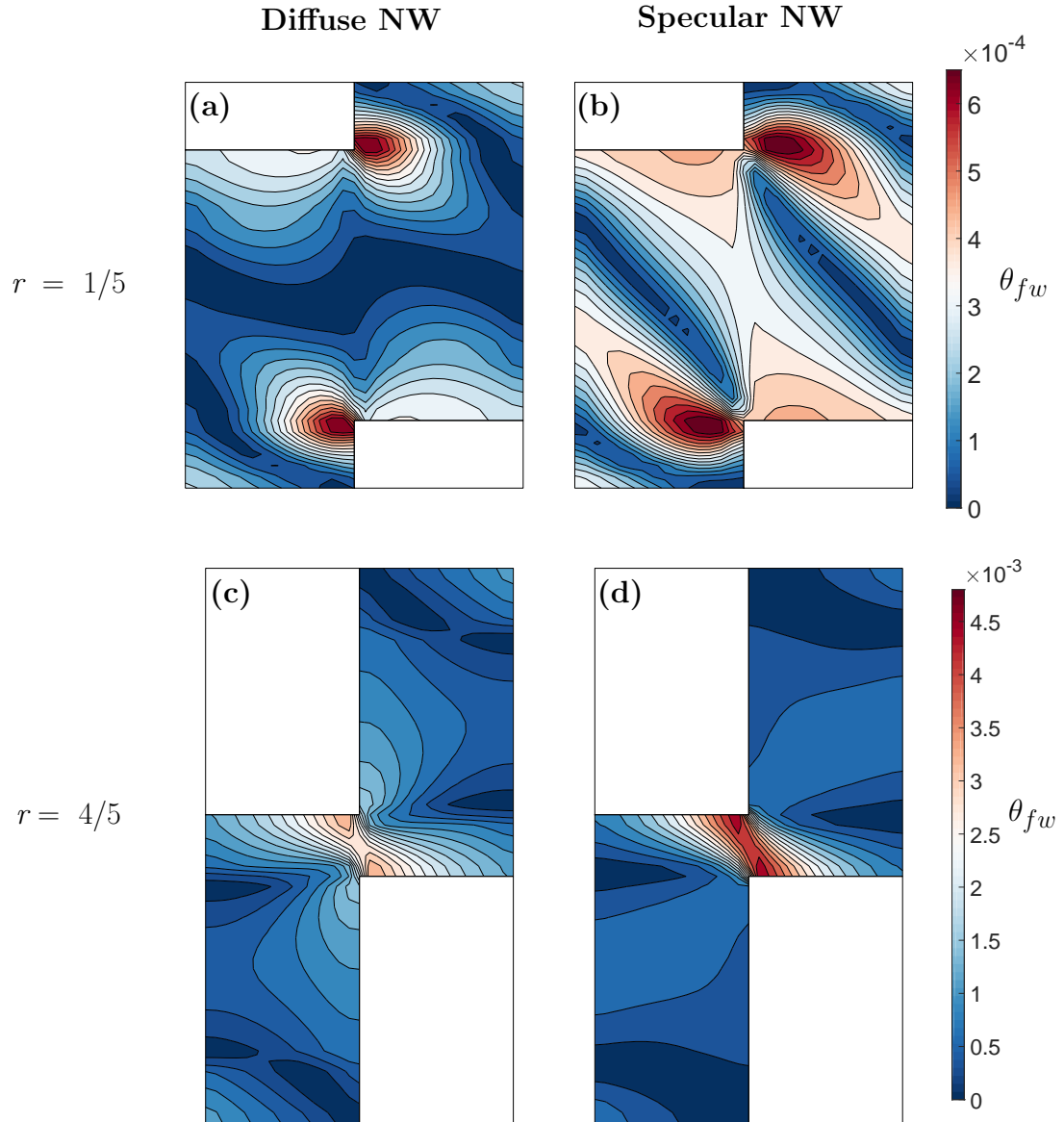


Figure 5.9: Flux weighted angle, θ_{fw} , contours for both the specular (b, d) and diffuse (a, c) NWs with r values (a, b) $r = 1/5$ and (c, d) $r = 4/5$. The cross-sections correspond to the NW centerline $\hat{x}\hat{y}$ plane located at $z = W/2$.

distance to the "bend" in the NW (see Fig. 5.10). The bend notably removes the direct line of sight between the inlet and outlet. The second (v2) alternates the direction of the offset thus maintaining a direct line of sight, retaining only two length

parameters, total length and chamber size. The heat baths are set to $T(\mathbf{r}_0) = 300\text{K}$ and $T(\mathbf{r}_L) = 310\text{K}$ at the inlet and outlet, respectively. The relative reduction, as

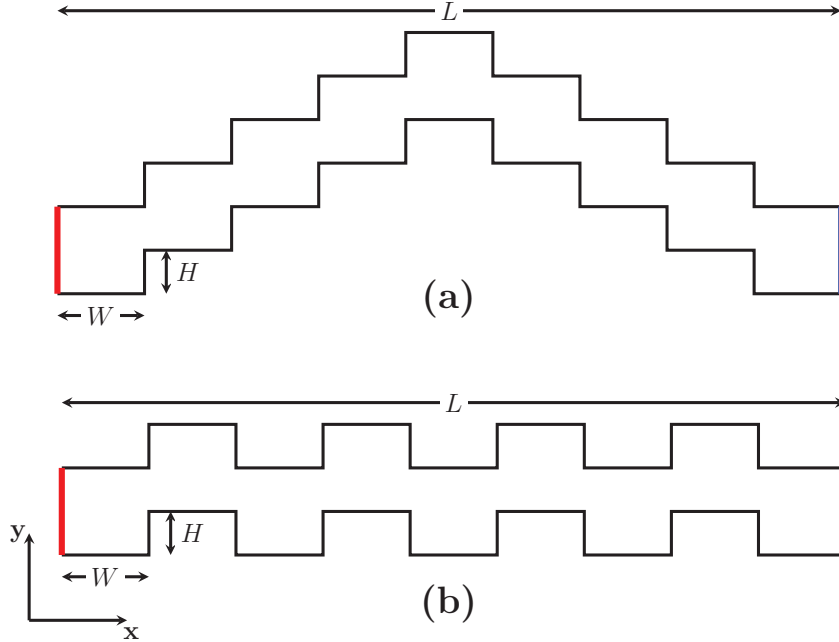


Figure 5.10: Two nanodevice geometries (a) v1 and (b) v2.

well as the absolute value, of the thermal conductances within geometries v1 and v2 are plotted in Figure 5.11, note that in the case of the finite length NW thermal conductance is well-defined and unambiguous. For the same offset height, v1 has substantially lower thermal conductance than v2, with a maximum relative difference of 41.5% for $H = 2W/5$. This result is due to the difference in the arrangement of offsets relative to the chamber, as well as the presence of the bend in v1. Note that the relative reduction in conductance is linear for v2 while nonlinear for v1. This is primarily because related to the line of sight(LOS) between inlet and outlet. The lack of a direct LOS in v1 causes all phonons to undergo backscattering,

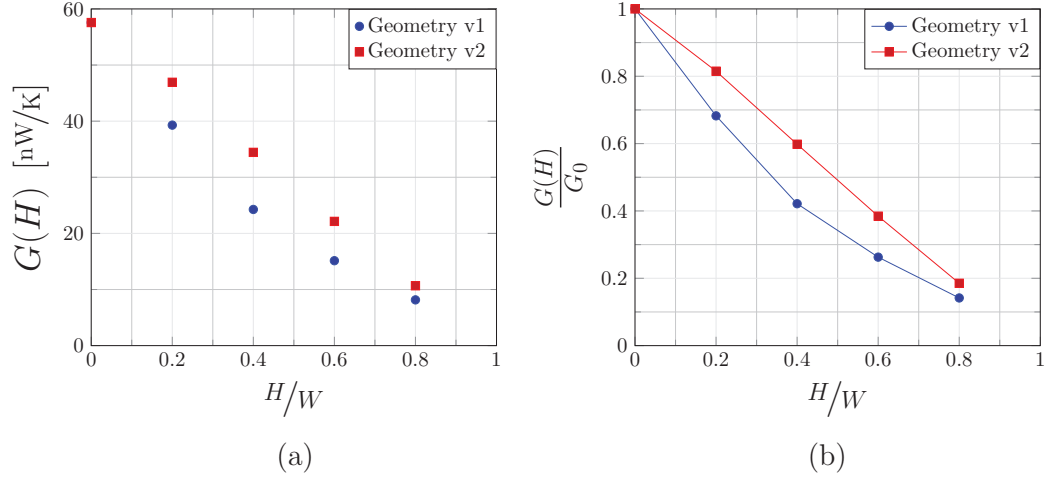


Figure 5.11: Plots of the relative conductance reduction (a) and absolute conductance values (b) for geometries v1 (blue) and v2 (red).

while a direct LOS in v2 allows a portion of the carriers to transport ballistically through the wire, leading to a larger conductance. Furthermore, v1 causes more phonon trapping due to a smaller view factor between adjacent chambers than in geometry v2. Thus it is clear from these results that a geometry which imposes greater backscattering and stronger phonon trapping, such as v1, is more effective at reducing phonon transport.

Comparison between uniform NWs of finite and infinite extent reveals a length dependent thermal conductivity. The conductivity of the finite length uniform NW is approximately 10.4 W/m K whereas the infinite uniform NW has a conductivity of 21.3 W/m K . This implies our thermal conductivity scales as $\kappa \propto L^\alpha$ where $\alpha \leq 1/3$ which is a smaller range of values for the scaling exponent than in previous studies of NWs [164, 165]. The difference is likely explained by the larger NWs we

are considering. At these larger length scales the interplay and competition between intrinsic and extrinsic mechanisms will lead to significantly different behaviors.

5.3.5 Verification of NW Simulations

There exist certain sources in the literature that are relevant for comparison and verification of our results. Specifically, we wish to ensure that we are accurately capturing the physics of interior phonon flow through the wire by verifying a number of key insights. In the limiting case of $H = 0$, the rough infinite NW has a thermal conductivity of $\sim 22 \frac{\text{W}}{\text{m}\cdot\text{K}}$. As we noted in sec. 5.3.2, experimental results from Li et al. and Poborchii et al. found that Si NWs of similar cross-section area had a thermal conductivity of $\sim 25 \frac{\text{W}}{\text{m}\cdot\text{K}}$ [146] and $\sim 17.5 \frac{\text{W}}{\text{m}\cdot\text{K}}$ [148] respectively. The close agreement is indicative that our methodology incorporates the resistive scattering effects present within a rough wire with dimensions far less than the phonon MFPs. Furthermore, BTE simulation results of Si NW "labyrinths" observed a reduction in the conductivity contribution of long MFP phonons with respect to a uniform NW [154]. This reduction is qualitatively similar to what was observed in fig. 5.6, although, as we noted in sec. 5.3.2, the effect is stronger in this work due to the smaller NW dimensions that lead to an increase in phonons traveling ballistically. These comparisons indicate that we are appropriately accounting for boundary scattering physics as well as the resistive effect of interior corners on the free flight of phonons.

5.4 Conclusion

To conclude, we find that low thermal conductivity nanostructures are those that maximize phonon backscattering and locally reverse the direction of phonon propagation. The chamber-offset geometry currently proposed causes more phonon backscattering events than alternative geometries presently in the literature as evidenced by thermal conductivity reductions of $>90\%$. The offset also causes a misalignment between the local phonon flux and the global temperature gradient. The degree of misalignment is smaller in the rough NW than in the smooth NW as diffuse boundary scattering facilitates the redistribution of energy within the phonon spectrum allowing phonons to more readily turn corners. Furthermore, for large offset heights, the nanostructure effectively traps phonons within individual chambers, inhibiting propagation through the wire and therefore reducing thermal transport by roughly 95% . We have demonstrated that the thermal conductivity of the chamber-offset NW falls below the Casimir limit for a uniform NW with cross-sectional area equivalent to the bottleneck. Additionally, we found that the chamber-offset NW causes a significant shift, with respect to the uniform NW, in the thermal energy distribution within the MFP spectrum, leading to a relative increase in heat carried by short MFP phonons. This shift invites potential use in combination with approaches such as impurity scattering, grain boundary scattering, and superlattices that are more suited for targeting small MFP carriers. The offset causes smaller MFP, higher frequency phonons to carry a larger proportion of the thermal energy which can then be better targeted by these other approaches. Ultimately, these

findings could be used to enable broadband control of phonon transport.

Chapter 6: A Phonon Boltzmann Study of Microscale Thermal Transport in α -RDX Cook-Off ⁵

In this chapter we apply the phonon BTE methodology, detailed in chapter 3, to the molecular crystal α RDX. Study of this energetic material marks a departure from the small unit-cell material based phonon systems studied chapters 4 and 5 which contained 1-2 atoms per unit cell. In contrast, α RDX contains 168 atoms in the unit cell which leads to unique thermal transport behaviors, and corresponding modeling challenges. Phonon modeling in energetic crystals is of particular interest as the microscale thermal transport properties of α RDX are believed to be major factors in the initiation process. We present a thorough examination of phonon properties which dominate energy storage and transport in α RDX. The phonon lifetimes are determined for all phonon branches, revealing the characteristic time scale of energy transfer amongst phonon modes. The phonon parameters also serve as inputs to a full Brillouin zone three dimensional phonon transport simulation in the presence of a hotspot. In addition to identifying the phonon mode contributions to

⁵Portions of this chapter appeared in the publication: *F. G. VanGessel, Gaurav Kumar, Daniel C. Elton and P. W. Chung, A Phonon Boltzmann Study of Microscale Thermal Transport in α -RDX Cook-Off. Proceedings of the 16th International Detonation Symposium arXiv:1808.08295[cond-mat.mtrl-sci] [48]*

thermal transport, and as N-N bond breaking is integral to disassociation, we identify phonon modes corresponding to large N-N bond stretch analyzing the manner in which these modes store and transfer energy.

6.1 Phonons in Energetic Materials

Phonons play an important role in initiating the chemical decomposition that can lead to detonation in secondary explosives such as α RDX [21, 28, 166]. However, open questions remain as to the exact nature of phonon-mediated energy transfer into the key intramolecular vibrational modes that result in chemical events. Dlott and coworkers have theorized that this process occurs in an indirect manner through multiphonon up-pumping [21]. Multiphonon up-pumping refers to a process in which energy is initially deposited in long-wavelength low frequency vibrational modes via shock or heating. This energy is subsequently transferred, via so-called "doorway modes", into intramolecular vibrational modes that correspond to key bond-stretching motions. However, Kraczek and Chung speculated that the energy transfer process may occur through a direct route without intermediate energy transfer [22]. Thus, further investigation is needed to elucidate the manner in which phonons store, transport, and transfer energy.

Among the candidate approaches for investigating phonon behavior in general materials are phonon Boltzmann and molecular dynamics (MD) methods. Though MD still remains a widely used method, and despite the many developments that enable the study of larger material domains, the fundamentally atomistic nature

restricts the application of MD to smaller length scales. Phonon Boltzmann is inherently better suited to microscale thermal transport simulations as it forgoes some of the atomistic information, i.e. vibrational phases, in favor of reaching length scales more commonly seen in real materials. To date, however, phonon Boltzmann studies have been limited mainly to crystals with a relatively few number of atoms in the unit cell, likely due in part to the computational complexity associated with modeling phonons in materials whose unit cells contain large numbers of atoms. For instance, α RDX is a complex molecular crystal containing 168 atoms in its unit cell, resulting in 504 phonon branches in the first Brillouin zone (BZ). In the continuum limit, each branch is a continuous curve representing the infinite number of carriers that may participate in the storage or transport of energy. Development of MD and BTE approaches for energetics could reveal much about the thermal behavior. Molecular dynamics calculations hold promise for determining the characteristic timescales associated with energy transfer amongst phonon bands. Furthermore, BTE simulations may give important insight into behavior of thermal and vibrational energy as it flows and scatters within a highly heterogeneous microstructural mixture. Such developments have not been attempted, as far as we are aware.

In this chapter, we present recent results in our attempts to investigate the possible mechanisms by which energy is transferred from low-frequency phonons into the molecular vibrations of α RDX. We begin by determining the phonon thermal properties based on a full Brillouin zone representation of every phonon vibrational mode. We identify phonon modes associated with large N-N bond stretch, as scission of the N-N bonds is understood to be of particular importance to the disassociation of

the RDX molecule [167]. In contrast to previous investigations detailed in this work, we determine phonon lifetimes by applying normal mode decomposition techniques to determine accurate phonon mode lifetimes. These lifetimes reveal important information regarding the time scales at which phonon modes scatter, a crucial parameter for understanding initiation. Finally, the phonon properties are then used as inputs to a phonon Boltzmann simulation of localized heating, i.e. a hotspot, in an α RDX grain to study out-of-equilibrium thermal transport. In addition, individual modal contributions to heat storage and transfer are calculated and the participation of large N-N stretching modes is quantified.

6.2 Methods

In order to form a more complete understanding of microscale energy transport in α RDX we use a variety of methods. These methods are used to a) perform a full BZ analysis of the phonon vibrational modes present in α RDX, focusing on the thermal transport properties of the phonons as well as a normal mode analysis, b) calculate the full-band highly accurate phonon lifetime data within the relaxation time approximation for all 504 branches in RDX, c) identify phonon modes which cause large relative displacements between bonded Nitrogen atoms, and d) perform phonon Boltzmann transport equation (BTE) simulation of a localized heating to investigate non-equilibrium energy transport in the presence of a hot spot.

6.2.1 α RDX Thermal Properties

A study of phonon-mediated thermal flow in α RDX requires a number of phonon properties, each of which may span several orders of magnitude in value. These properties include frequency, ω_ϕ , specific heat, C_ϕ , group velocity, \mathbf{v}_ϕ , and relaxation time, τ_ϕ . With the exception of phonon relaxation time, calculation of these properties may be accomplished via LD using the approach outlined in section 3.3.4. The intra- and inter- molecular interactions are parameterized by the Smith and Bharadwaj potential [168]. The LD approach allows for the determination not only of the phonon properties but also the phonon mode shapes, i.e. the eigenvectors, \mathbf{U} calculated from the eigensystem formed by the dynamical matrix, $\mathbf{D}\mathbf{U} = \omega^2\mathbf{U}$ [169]. Within the phonon gas model framework the thermal conductivity (TC) of a material can be expressed as [170]

$$\kappa_{ij} = \sum_{\phi} C_{\phi} v_{\phi i} v_{\phi j} \tau_{\phi} \quad (6.1)$$

where $i, j \in (1, 2, 3)$ are spatial indices. For the initial BZ analysis, we employ a gray approximation for the phonon relaxation times assuming $\tau_{\phi} = 217$ ps for all phonon modes. This number is chosen to ensure that the average TC predicted by eq. 6.1 agrees with the average TC published in [171], $\bar{\kappa} = 0.355$ J/mK.s

In addition to the absolute TC we also consider the thermal conductivity accumulation (TCA) with respect to frequency,

$$\kappa_{ii}^{accum}(\omega) = \frac{1}{\kappa_{ii}} \sum_{\{\phi: \omega_{\phi} \leq \omega\}} C_{\phi} v_{\phi i}^2 \tau_{\phi} \quad (6.2)$$

The TCA quantifies the relative contributions of different regions of the frequency

spectrum to thermal transport.

6.2.2 Full Band Phonon Relaxation Times

Despite the importance of phonons in initiation mechanisms of energetics, surprisingly little is known about their fundamental anharmonic phonon properties such as relaxation times. Relaxation times, or lifetimes, imply an important time-scale with across which phonon modes exchange energy. Knowledge of these lifetimes are especially important in energetics as it determines the rate at which energy is "up-pumped" into the intramolecular vibrational modes that play a key role in initiation. Attempts to calculate the phonon energy transfer rates in energetic materials involved theoretical calculations for estimating the anharmonic coupling in molecular crystals [26]. Ye and Koshi subsequently extended this theoretical approach by using the entire material frequency spectrum for several energetics. They found, among the energetic materials they considered, energy transfer rates exhibited a monotonically decreasing behavior with respect to frequency [29]. However, the theoretical approaches detailed in these works resorted to a number of simplifications due to the complexity of the unit cells comprising energetic materials. The three main assumptions were that i) the anharmonic coupling was constant between all modes, ii) optical modes had zero bandwidth, and iii) all phonons were in equilibrium [26].

In contrast, studies of phonon lifetimes in atomic crystals, i.e. simple unit-celled crystals, have been relatively more numerous. The most commonly used

approach for the determination of phonon lifetimes in atomic crystals has been the iterative procedure for solving the full-scattering BTE, this approach was detailed in sec. 2.2.2.3. However, the full-scattering approach requires an extensive search over all modes in the Brillouin zone to determine all three phonon interactions satisfying the energy conservation and pseudo-momentum rules (see eq. 2.13). Due to this search, the computing expense of performing these simulations scales with the fourth power of the number of atoms in the unit cell. Thus, the large number of branches in RDX currently precludes the use of the iterative method.

We believe that normal mode decomposition approaches, in conjunction with advances in computing architecture, now offer a path to the determination of phonon lifetimes. These MD approaches allow us to circumvent many of the assumptions that were previously necessary for the determination of phonon lifetimes in complex unit-celled crystals. Therefore, we choose to use a MD based approach which determines the characteristic decay time of fluctuations in the energy of individual phonon modes. We remark that this part of the effort extends, for the first time, existing techniques previously only applied to atomic crystals to obtain accurate phonon relaxation times for *every* phonon branch in α RDX.

We use a normal mode decomposition(NMD) approach to determine the phonon lifetimes. The important steps calculating the phonon lifetimes are outlined here, for a complete description of the method the reader is referred to [172]. The NMD technique has been previously used to calculate phonon lifetimes in solid argon, amorphous silicon, and crystalline silicon. As a first step in extending this approach to complex unit celled crystals we consider a relatively small system composed of

2x2x2 = 8 unit cells. The supercell is first energy minimized at constant pressure using the atomic potential described in [168]. The supercell eigenvectors, $U_{\phi\alpha\beta}$ are extracted for all allowed phonon modes, where $\alpha \in (1, 2, 3)$ is the spatial index and β indexes the atoms in the unit cell. Separately, a MD simulation is performed using LAMMPS [173] with 1 fs time-step. The system is initially equilibrated for 1000 ps at 300K under NPT conditions. A subsequent production step is then performed using NVE conditions, during which displacement and velocity data for all atoms in the system were gathered every 4 fs for 2000 ps. Using the supercell eigenvectors we decompose the atomic displacements in order to calculate the so called phonon coordinate. The phonon mode coordinate, $q_\phi(t)$, is defined

$$q_\phi(t) = \sum_{\alpha\beta l}^{3nN} \sqrt{\frac{m_\beta}{N}} u_{\alpha\beta l}(t) U_{\phi\alpha\beta}^* \exp(i\mathbf{k} \cdot r_{0l}) , \quad (6.3)$$

where m_β is the mass of atom β , n is the number of atoms in the unit cell, N is the number of unit cells in the supercell, $u_{\alpha\beta l}$ is the α^{th} component of displacement of the β^{th} atom of the l^{th} unit cell, \mathbf{k} is the wavevector corresponding to mode ϕ , and r_{0l} is the spatial location of the l^{th} unit cell. The phonon coordinate velocity, $\dot{q}_\phi(t)$, is determined by replacing $u_{\alpha\beta l}$ with the atomic velocities, $\dot{u}_{\alpha\beta l}$, in eq. 6.3. From the phonon coordinates and velocities, we calculate the mode projected SED, $\Phi(\mathbf{k}, \omega)$, defined as

$$\Phi(\mathbf{k}, \omega) = \left| \frac{1}{\sqrt{2\pi}} \int_{-\infty}^{\infty} \dot{q}_\phi \exp(-i\omega t) dt \right|^2 \quad (6.4)$$

The SED represents the kinetic energy density response of each mode with respect frequencies within the material frequency spectrum. The phonon SED is strongly

peaked at the phonon mode’s natural frequency. Within a frequency window centered on the natural frequency the SED is fit using a Lorentzian function:

$$\Phi(\mathbf{k}, \omega) = \frac{\sqrt{P_3} \left[P_1 \frac{P_2 + P_3}{4\pi} \right]}{[(P_2 - \omega)^2 + P_3]} \quad (6.5)$$

The Lorentzian half width at half maximum linewidth is related to the fitting parameters through the equation $\Gamma_\phi = \sqrt{P_3}$. Finally, we calculate the phonon lifetime to be $\tau_\phi = 1/2\Gamma_\phi$.

6.2.3 Phonon Boltzmann Transport Modeling in α RDX

A hotspot in an energetic represents a localized region in which the energy density is larger than the surrounding material. The hotspot corresponds to the location at which chemistry is likely to begin and therefore plays a fundamental role in initiation processes [21]. In order to model phonon behavior under non-equilibrium conditions, such as phonons in a hotspot, we use the full BZ three dimensional phonon BTE solution method detailed in chapter 3. For simplicity, we initially consider the steady state problem and hold the hot spot in a fixed location. The phonon BTE method yields the spatial variation of the modal energy values, $e_\phi(\mathbf{r})$, as well as the modal fluxes, $\mathbf{f}_\phi(\mathbf{r}) = \mathbf{v}_\phi e_\phi(\mathbf{r})$. The total energy and total flux values are calculated as a sum over the sampled phonon modes, i.e. $e(\mathbf{r}) = \sum_\phi e_\phi(\mathbf{r})$ and $f(\mathbf{r}) = \sum_\phi \mathbf{f}_\phi(\mathbf{r})$. The phonon properties used here are the same as those obtained for analysis of the phonon thermal properties where a sampling of 172,368 phonon modes was used. Different, however, are the phonon relaxation times, τ_ϕ , which are obtained now using the NMD procedure detailed in sec. 6.2.2. Due

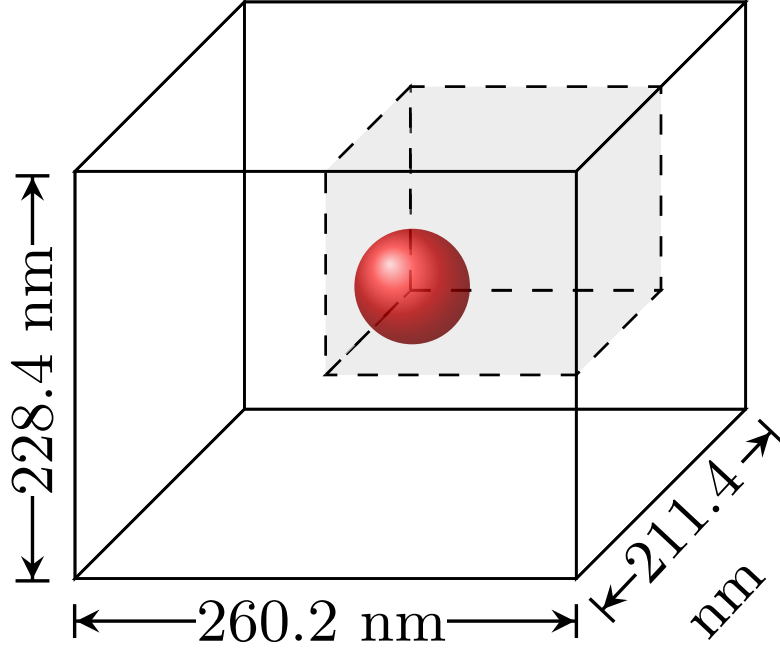


Figure 6.1: Physical domain representing a hotspot in RDX. The sphere indicates the hotspot region. Due to the symmetry, the simulation domain reduces to the shaded octant.

to the large computational requirements associated with obtaining τ_ϕ throughout the BZ we use the relaxation times obtained at the BZ center and assume that τ_ϕ is constant within each phonon branch. This therefore assumes that *scattering* is isotropic presently but distinct for each polarization. The simulation domain corresponds to 200x200x200 unit cell tiles along the three principal direction, i.e. [100], [010], and [001]. The domain is discretized using 10,400 control volumes. A spherical hotspot with 30 nm radius is placed at the center of the domain. Within the hotspot region, 1×10^{-10} J of energy is sourced into the acoustic modes. We choose to source energy into the acoustic modes in order to mimic the scenario in which energy is deposited into low-frequency modes by shock or heat and is subsequently

up-pumped to intramolecular vibrational modes. The physical domain is pictured in Figure 6.1, due to symmetry we simulate only an octant of this domain (i.e. the shaded region in Fig. 6.1). Symmetry planes are modeled as specular boundaries while the other boundaries correspond to applied temperature conditions with $T = 300\text{K}$.

6.2.4 N-N Bond Stretch Metric

The stretching of N-N bonds is believed to play a fundamental role in the disassociation of the RDX molecule [167,174]. Therefore, we wish to identify phonon modes that correspond to large N-N bond stretch as these modes may be a key factor in initiation. The phonon mode ϕ displaces atom i to the spatial location, $\mathbf{r}_{\phi i} = \mathbf{x}_i + \mathbf{u}_{\phi i}$. Here \mathbf{x}_i is the equilibrium atomic location while the displacement due to the phonon is given by the vector $\mathbf{u}_{\phi i} = A_{\phi i} \mathbf{U}_{\phi i}$, where $\mathbf{U}_{\phi i}$ represents the components of the mode shape eigenvector $\mathbf{U}_{\phi i}$ corresponding to atom i , and $A_{\phi i} = \sqrt{e_{\phi}/m_i \omega_{\phi}^2}$ is the phonon mode amplitude [169]. Therefore, given the energy in a phonon mode, the resulting spatial location of all atoms can be calculated. Then, the b^{th} N-N bond connecting atoms b_1 and b_2 is stretched to the length $\|\mathbf{r}_{\phi b_1} - \mathbf{r}_{\phi b_2}\|$. The bond stretch metric for mode ϕ is the maximum bond stretch length over all bonds,

$$\Delta_{\phi} = \max_b \|\mathbf{r}_{\phi b_1} - \mathbf{r}_{\phi b_2}\| \quad (6.6)$$

In order to complete the calculation of the bond stretch we require values for the phonon energy of each individual mode. Here we consider two limiting cases. The first case assumes thermal equilibrium in which energy, and therefore amplitude,

is determined by Bose statistics at temperature T . The second case corresponds to a non-equilibrium situation in which the modal amplitudes are uniformly constant. The second case allow us to consider modes that may not typically contain a large amount of energy, when in equilibrium, but whose displacements correspond to large N-N stretch. In the equilibrium case $A_{\phi i} = \sqrt{e_{\phi}^0/m_i\omega_{\phi}^2}$ while in the uniform case $A_{\phi i} = A_0$. Thus we introduce the modal N-N stretch metric, written Δ_{ϕ}^{eq} and Δ_{ϕ}^{uni} respectively, for the equilibrium (EQ) and uniform (UNI) cases respectively.

6.3 Results

6.3.1 Full Brillouin Zone Analysis of RDX

The phonon frequency surfaces for a quadrant in the $k_z = 0$ plane of the RDX BZ is shown in Fig. 6.2, for clarity only the first 14 of the 504 total branches are shown. For each branch, we use a uniform sampling of 342 wavevectors throughout the BZ which results in 172,368 phonon modes. Figures 6.3 and 6.4 show the contribution of discrete frequency intervals to the group velocity component magnitudes and specific heat respectively. The contribution from discrete frequency intervals to a thermal property is calculated using the equation

$$a(\omega) = \sum_{\{\phi : \omega_{\phi} \in [\omega, \omega + \Delta\omega]\}} a_{\phi} \quad (6.7)$$

where a is any phonon mode property. The specific heat represents the phonon modes ability to store energy, while the group velocity is a measure of the speed with which a phonon mode transports energy. The total specific heat is calculated

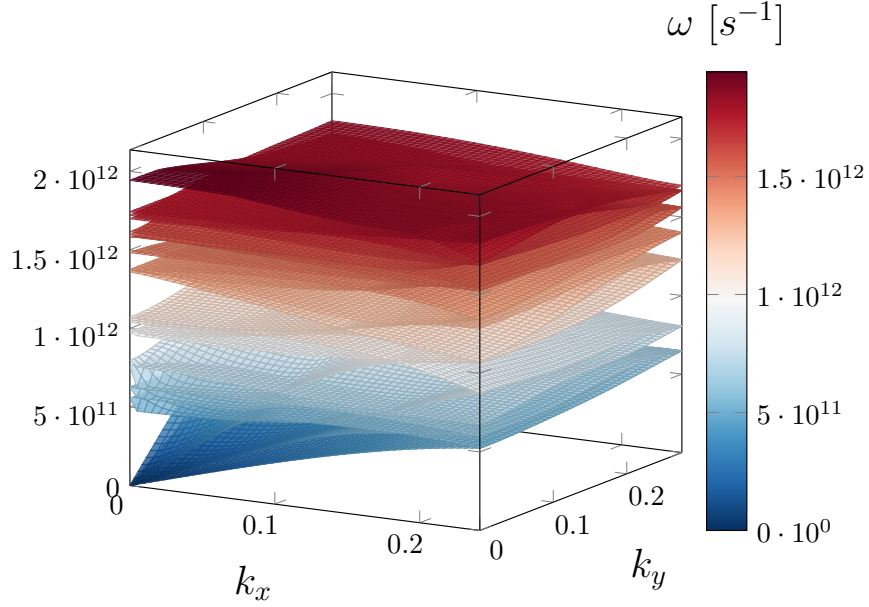


Figure 6.2: Frequency surfaces of first 14 branches in the quadrant of the $k_z = 0$ plane of the BZ.

to be $C_v = 4.11 \times 10^3 \text{ kJ/m}^3\text{K}$ which is within roughly a factor of two of the experimental value $1.96 \times 10^3 \text{ kJ/m}^3\text{K}$ [175]. The discrepancy between our calculated value and the reported experimental value is due to the implicit assumption of 0K in LD. The inclusion of temperature would cause an overall reduction in the frequency values, reducing the specific heat value. Furthermore, the calculated group velocity magnitudes agree with those reported in [22], which is to be expected since the same atomic potential is presently used. Figure 6.4 indicates that the phonon frequency spectrum of RDX contains large band gaps punctuated by narrow bands. Additionally, in Fig. 6.3 we can see that phonon modes with the largest group velocities are located at low frequencies, but a few bands at higher frequencies do possess non-negligible group velocities. The group velocity plots are qualitatively similar to

those produced in [22], indicating the correctness of the calculated phonon group velocities. Therefore as noted in [22], we expect the optical modes to contribute significantly to thermal transport in RDX.

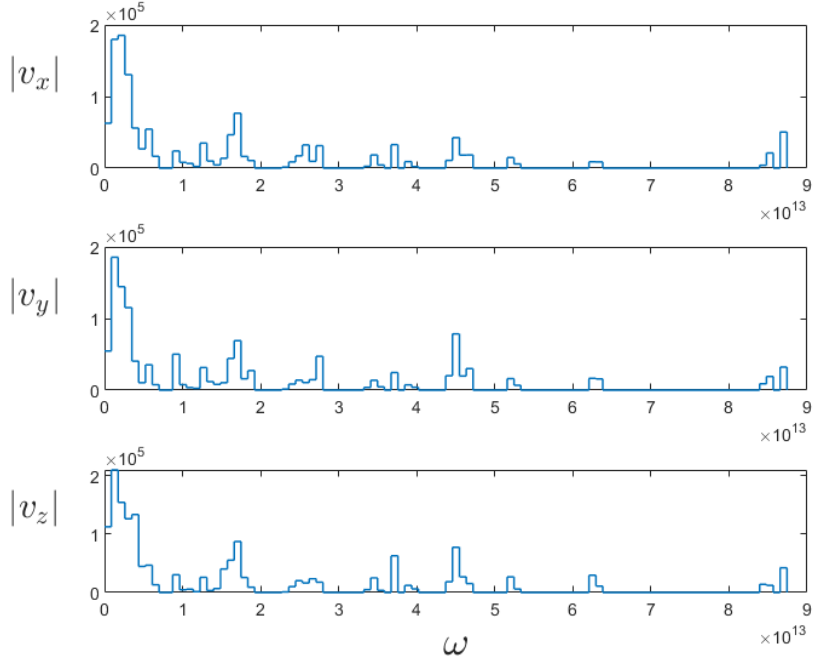


Figure 6.3: Stair plot of the group velocity component magnitudes vs. frequency.

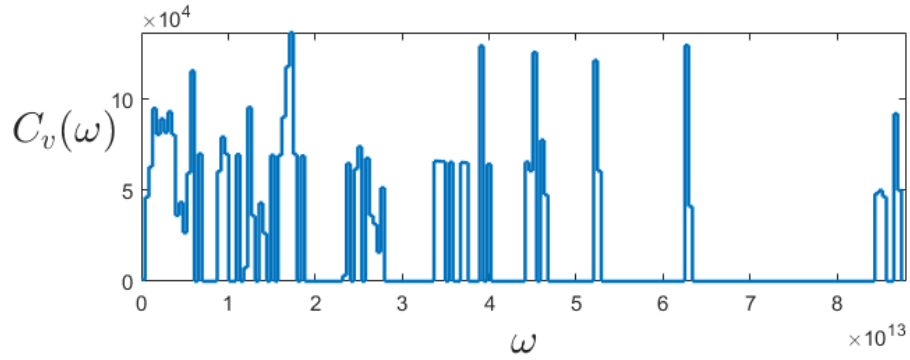


Figure 6.4: Stair plot of specific heat vs. frequency.

Calculating the TC tensor via Eq. 6.1 yields

$$\kappa_{11} = 0.33 \text{ J/mK} , \kappa_{22} = 0.28 \text{ J/mK} , \kappa_{33} = 0.45 \text{ J/mK} \quad (6.8)$$

while all other components are negligible. Note that there exists a high degree of anisotropy in the thermal transport in α RDX with TC along the z direction 1.6 times larger than along the y direction. While the average TC calculated here matches with the published values in [171], our TC possesses higher anisotropy due to the gray phonon approximation. The calculation enables the consideration of anisotropy by sampling the phonons from the full three-dimensional BZ. The anisotropy in the present system is due to the non-radially symmetric BZ dispersion surfaces, i.e. microscale anisotropy, as well as the non-cubic nature of the unit cell, i.e. macroscopic anisotropy. The TCA is shown in Fig. 6.5 where we see that the phonons in the low frequency regime, $\omega < 1$ THz, contribute to a larger percentage of the thermal transport along the y and z directions, 20% and 25% respectively, than to thermal transport along the x direction 15%. However, phonons within the frequency interval $2 \text{ THz} < \omega < 3 \text{ THz}$ contribute roughly 24% of the total TC along the x -direction, causing κ_{xx} to overtake κ_{yy} and κ_{zz} in this interval. Finally, note that phonons with frequencies > 3 THz contribute approximately 25% of the TC along the y direction versus roughly 17.5% to conductivity along the x or z directions. We suspect that because phonon modes with frequencies > 10 THz contribute $< 20\%$ of the thermal conductivity, once energy is introduced into those modes, heat transfer will be mitigated, possibly leading to thermal runaway and ultimately cookoff. The final portion of this BZ analysis focuses on the phonon modes that correspond to large stretch of N-N bonds. The bond stretch metric for the EQ, and UNI cases was detailed in section 6.2.4. Histograms of the mode stretches for the EQ and UNI cases are shown in Fig. 6.6. Both distributions are heavily weighted toward zero

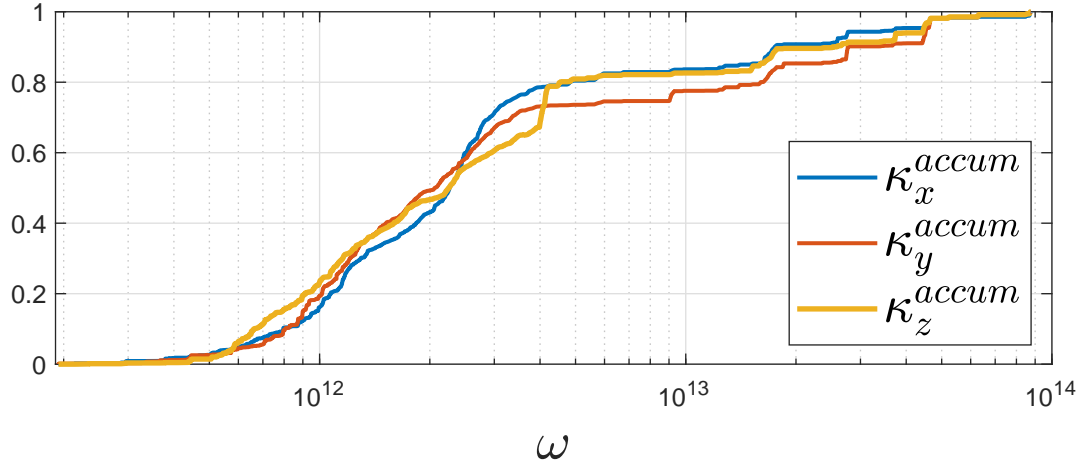


Figure 6.5: TCA vs. frequency for all three principle directions.

indicating the vast majority of modes contribute negligibly to N-N bond stretching. The contributions of phonons within discrete frequency intervals to the EQ and UNI mode stretch is calculated using Eq. 6.7 with $a_\phi = \Delta_\phi^{eq}, \Delta_\phi^{uni}$ and is visualized in Fig. 6.7. We note that low frequencies, < 10 THz, intervals correspond to the largest EQ N-N bond stretching, but negligible bond stretching for the UNI case. However, above 10 THz the locations, and also the shape, of the peaks for Δ^{eq} and Δ^{uni} are quite similar. The locations of these peaks occur around roughly 17.5, 27.5, and 37.5 THz. The similarity observed at higher frequencies is due to the commonality of U_ϕ in both stretching metrics. Above 10 THz, the largest peak in the bond stretch occurs at 52.5 THz for both the EQ and UNI metrics. Presence of this peak in both measures of bond stretch indicates the frequency interval around 52.5 THz may play a major role in facilitating N-N bond scission. Thus using our bond stretch metric we have identified the region of the frequency spectrum most likely to be involved in initiation. Note that our prediction of 52.5 THz compares

well with other work which predicted the important N-N bond stretching mode to be in the 30-60 THz range [21, 166].

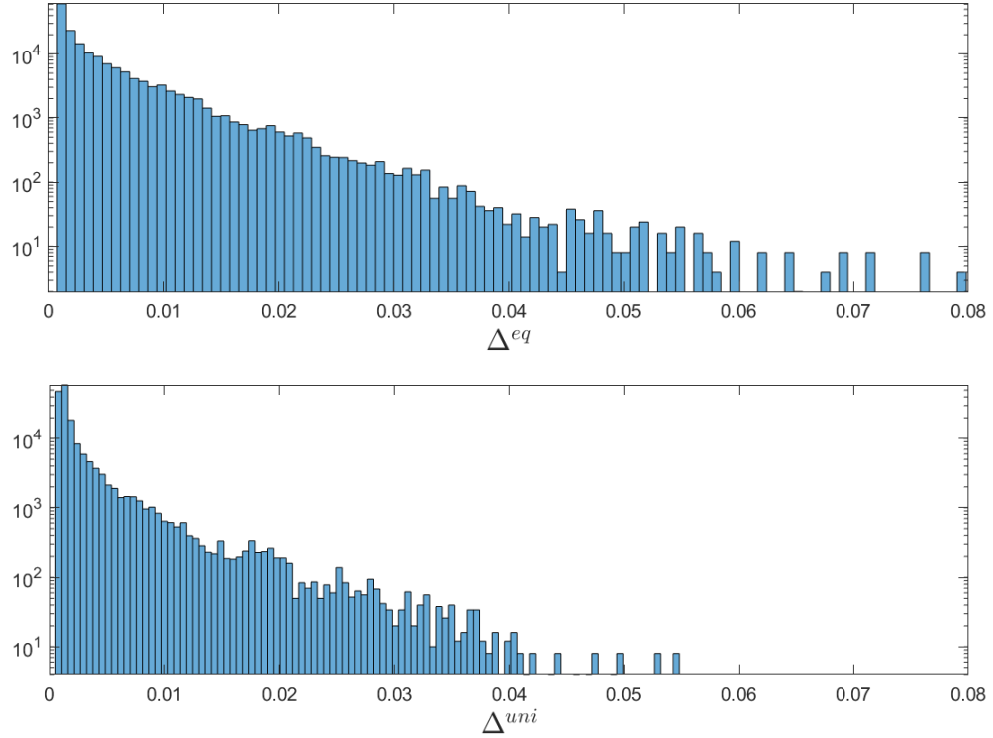


Figure 6.6: Histogram of phonon mode stretches for the EQ (top) and UNI (bottom) case. The abscissa is expressed in units of fraction of the average N-N bond length.

6.3.2 Full-Band Relaxation Times of RDX ⁶

Shown in Fig. 6.8 is the Lorentzian fitting result for a single phonon mode SED. The following metric was used to quantify the root-mean-square error, E_ϕ , of

⁶The author gratefully acknowledges the work of Gaurav Kumar and Daniel C. Elton. G.K. performed the MD simulation as well as the fitting and analysis of the full-band RDX relaxation times. D.E. wrote the NMD FORTRAN code and provided valuable insights into the fitting procedure.

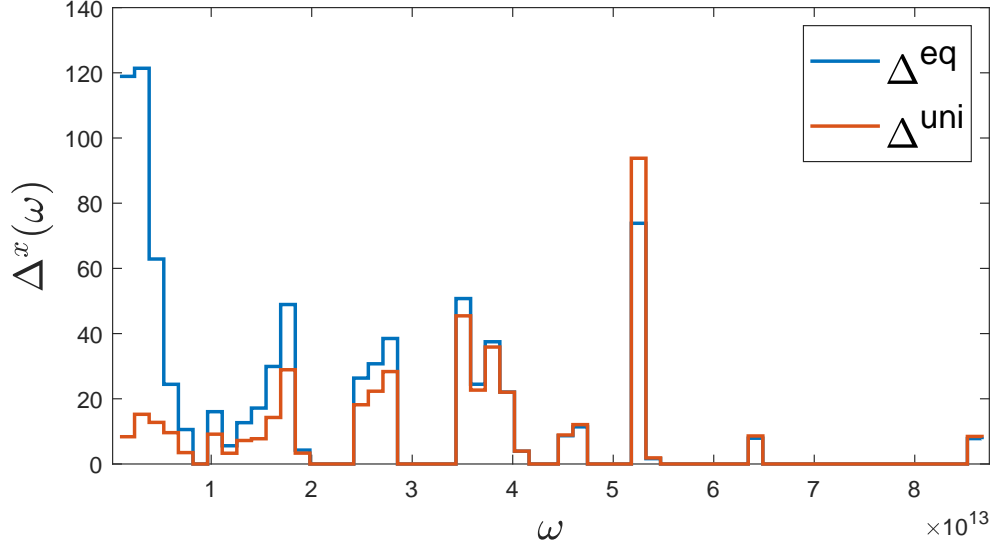


Figure 6.7: Plot of N-N bond stretch contribution from discrete intervals in the frequency spectrum. The bond stretch has units of angstroms.

the Lorentzian fitting for the SED of phonon mode ϕ

$$E_\phi = \sqrt{\frac{\sum_{l=1}^{n_d} (\Phi_{\phi l} - \Phi_{\phi l}^{fit})^2}{n_d}}, \quad (6.9)$$

where n_d is the number of data points extracted for each SED, and $\Phi_{\phi l} - \Phi_{\phi l}^{fit}$ is the difference in the raw SED data and the fitted Lorentzian curve at data point l . The percent error for the fitting of *all* phonon modes is defined as

$$PE_\phi = 100 \frac{\sqrt{\frac{\sum_{\phi=1}^{n_m} E_\phi^2}{n_m}}}{\sqrt{\frac{\sum_{\phi=1}^{n_m} \sum_{l=1}^{n_d} \Phi_{\phi l}^2}{n_m \times n_d}}}, \quad (6.10)$$

where n_m is the total number of phonon modes. Using the above metric we get 2.61% error in fitting the SED for all modes in a 2x2x2 RDX supercell. The standard deviation of E_ϕ values over all modes is calculated as

$$\sigma_{fit} = \frac{\sqrt{\sum_{\phi}^{n_m} \left(E_\phi - \frac{\sum_{\phi}^{n_m} E_\phi}{n_m} \right)^2}}{\frac{\sum_{\phi}^{n_m} E_\phi}{n_m}}. \quad (6.11)$$

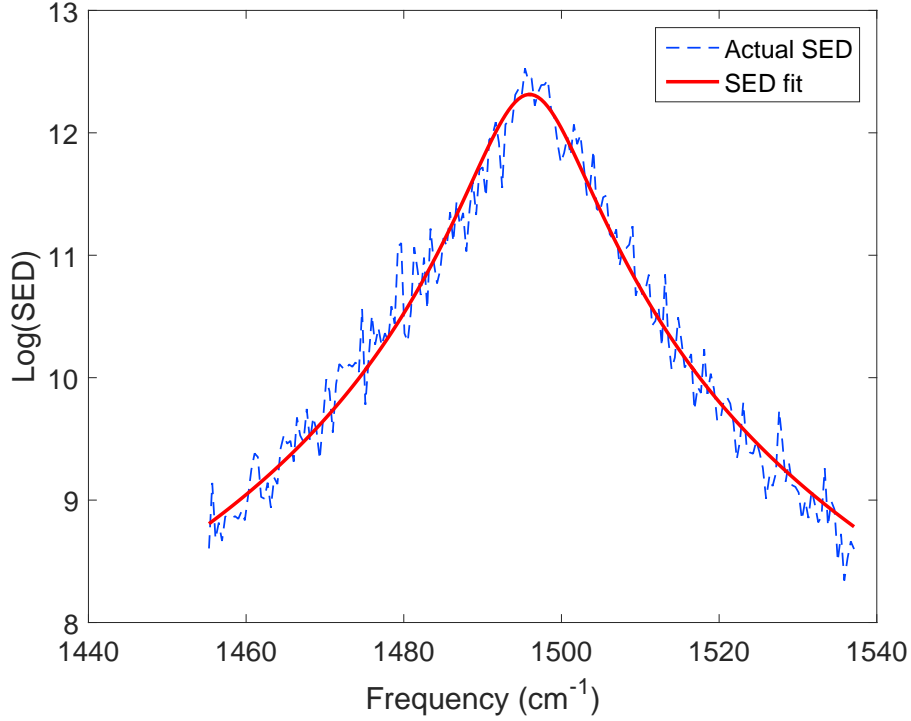


Figure 6.8: SED vs Frequency for an optical branch of 2x2x2 supercell.

σ_{fit} was found to be 6.6×10^{-3} suggesting a consistently good fit for all phonon modes.

Figure 6.9 indicates that the phonon lifetime values for a 2x2x2 supercell of RDX fall in the range of 0.9 ps to 34.2 ps. Similar results were obtained for a 1x1x1 supercell of RDX. These results are in good agreement with RDX lifetime values reported in [29], which were found to fall in the range of 2.5 ps to 11 ps. We note, that our results display an upturn in phonon lifetimes at large frequencies, this behavior runs counter to that reported by Ye and Koshi [29]. The cause of these differences will be the focus of future work. A histogram of the phonon mode lifetimes is plotted in Fig. 6.10. The majority of phonon modes have lifetimes of less than 10 ps.

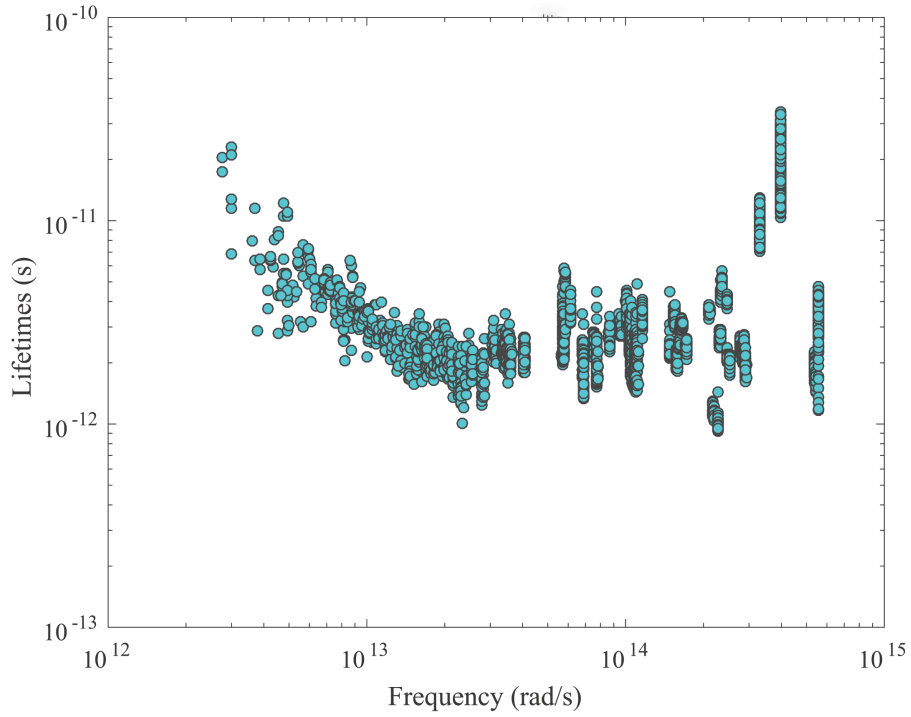


Figure 6.9: Phonon Lifetimes vs Frequency for RDX 2x2x2 supercell.

We note that the BZ sampling used presently for the phonon lifetimes has a number of drawbacks. By only using a 1x1x1 supercell, we are only sampling phonons modes which fall at the Γ point, i.e. $\mathbf{k} = \mathbf{0}$. The acoustic mode lifetimes at the Γ point are zero, however the acoustic branch modes should contribute significantly to thermal transport. Therefore, a finer sampling of wavevectors throughout the Brillouin zone is required to compute more accurate predictions of TC values. Computation of phonon properties with a larger supercell for better sampling of the BZ is currently underway.

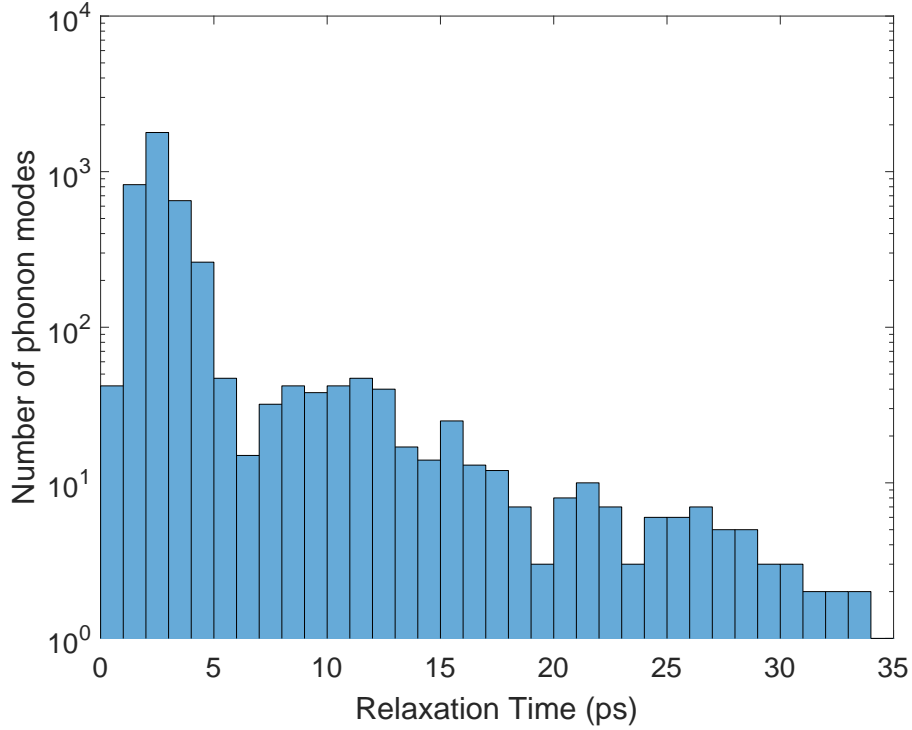


Figure 6.10: : Number of phonon modes vs phonon relaxation time for RDX 2x2x2.

6.3.3 Phonon BTE Simulation of RDX Hotspot

In this section we present the results of a full BZ three-dimensional phonon BTE simulation of localized heating, i.e. hotspot, in α RDX. It is believed that hotspot formations play an integral role in exciting the intramolecular vibrations associated with N-N bond breaking, i.e. the large Δ_ϕ modes [22, 166]. Previous studies have generally assumed that phonons within the hotspot are in equilibrium at the hotspot temperature [21]. Inclusion of non-equilibrium thermal effects is often performed in an ad hoc manner, such as assuming the hotspot energy is distributed only among low frequency vibrational modes [21, 22]. Here, we seek a quantitative approach for determining the actual distribution of out-of-equilibrium phonon mode

occupations throughout a three-dimensional domain. This will provide a more complete picture of how energy is distributed among phonon modes, which modes are responsible for the transport of thermal energy away from the hotspot, and what role modes corresponding to large Δ_ϕ play.

We analyze the spatial variation of the phonon energy along the x , y , and z axes emanating from the center of the hotspot (the x , y , z axes are aligned with the [100], [010], and [001] crystallographic directions respectively). The absolute phonon energy along each direction is plotted in Fig. 6.11. The total energy rapidly decreases away from the hotspot center, reaching $<1\%$ of the maximum energy value when $r > 0.75 \mu\text{m}$. In αRDX the thermal carriers are unable to efficiently remove heat from the hotspot region. In addition, the discrepancy of the energy values along the x , y , and z direction for the same r values is indicative of the effect of macroscopic, and microscale, phonon anisotropy on the TC.

To better understand the importance that modes with large N-N bond stretch might have, let us consider the 1,724 modes that have the largest N-N bond stretches. This represents 1% of the 172,368 total modes in the system, i.e. the 1% of all modes with the largest N-N bond stretch. We define two different sets corresponding to the EQ and UNI conditions, δ^{eq} and δ^{uni} respectively. The fractional energy residing in δ^{eq} (and similarly for δ^{uni}) calculated as $1/e_{tot} \times \sum_{\phi \in \delta^{eq}} e_\phi$ where $e_{tot} = \sum_{\phi} e_\phi$ is reported in Table 6.3.3. Incidentally, we note that the intersection of δ^{eq} and δ^{uni} is empty and the energy in each set is roughly equal to 1%. The percentage of energy in δ^{eq} is slightly larger than in δ^{uni} likely because modes in δ^{uni} have higher frequencies, which are generally less populated than lower frequency modes.

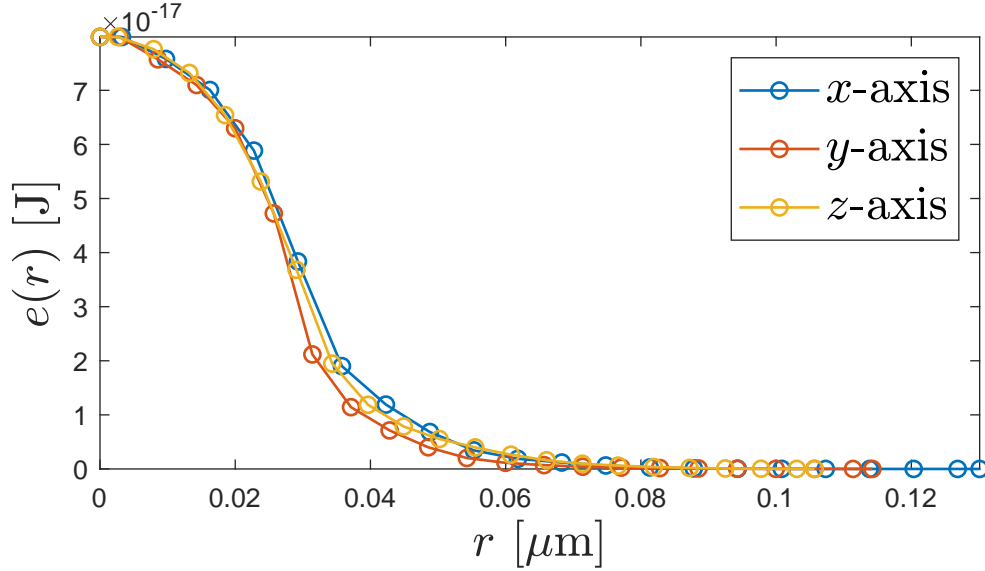


Figure 6.11: : Total energy along three Cartesian directions emanating out from the hotspot center.

δ^{eq}	1.08%
δ^{uni}	0.94%

Table 6.1: Percent of energy residing in large stretching modes, δ

Finally, we analyze the modal thermal flux behavior in the presence of a hotspot. The spatial variation in flux magnitude in the three Cartesian directions is plotted in Fig. 6.12, the flux reaches a maximum at the hot spot boundary regardless of direction. This indicates relatively more energy resides in modes with large group velocities in that spatial region. Furthermore, we note the significantly larger flux along the z -direction, as our BZ analysis predicted. Kraczek and Chung predicted that optical modes will carry a significant portion of the flux in α RDX [22]. We find this to be the case with the exact percentages reported in table 6.3.3. Table 6.3.3 indicates a significant departure in the manner in which energy transfer occurs

	Acoustic	Optical
f_x along x -axis	26%	74%
f_y along y -axis	22%	78%
f_z along z -axis	37%	63%

Table 6.2: Percentage of flux transported by acoustic and optical modes along principal directions.

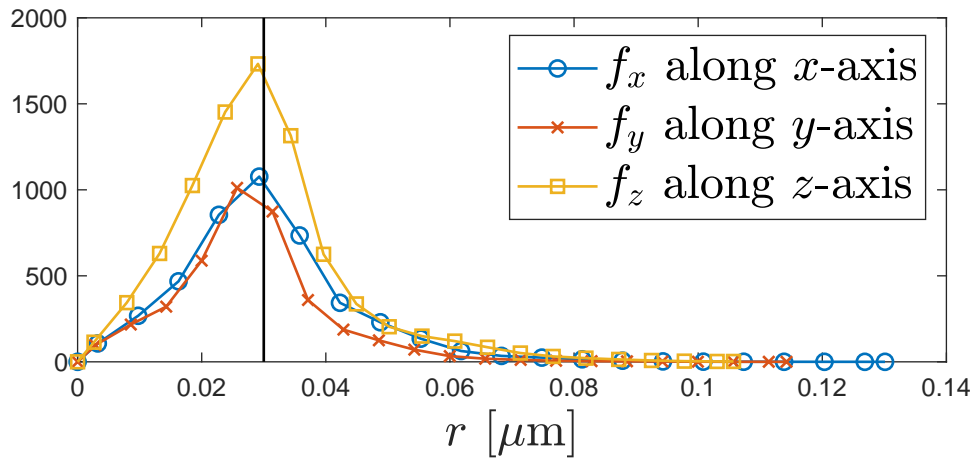


Figure 6.12: Flux components along the Cartesian directions emanating from hotspot center. The vertical black line indicates the hotspot boundary.

in α RDX compared to simple atomic crystals. Whereas optical mode contribution is minimal in atomic crystals ($\sim 5\%$ in bulk Si [159]), these modes are dominant contributors to the thermal flux in α RDX.

Finally, we analyze the flux contribution from the δ^{eq} and δ^{uni} stretching modes. The flux contribution from these modes is calculated for δ^{eq} (and similarly for δ^{uni}) using the equation $1/f_i \times \sum_{\phi \in \delta^{eq}} f_{\phi i}$ where $f_i = \sum_{\phi} f_{\phi i}$ and $i = x, y, z$. The contribution to the thermal flux from both the δ^{eq} and δ^{uni} stretching modes

along the three principal directions is plotted in Figs. 6.13. We observe that thermal flux contributions are anisotropic for the EQ class but isotropic for the UNI class. The EQ class transports energy preferentially along the z -direction, and to a lesser degree along the y -axis. In fact the thermal flux along the y -axis exceeds that along the x -axis, this behavior is the reverse of the TC tensor in Eq. 6.8 where $\kappa_{xx} > \kappa_{yy}$. Note that δ^{eq} contributes negative flux near the hotspot center due to significant energy residing in δ^{eq} phonon modes which travel in the $-x$ direction, however the total flux, f_x , remains positive at this location. In addition, the overall magnitude of the flux contribution from δ^{eq} is a factor of 2-10 times larger than the δ^{uni} contribution as a result of the relatively larger group velocities of the phonon modes constituting δ^{eq} . Furthermore, while the ratio of energy residing in δ^{eq} was nearly equal to the mode number fraction, δ^{eq} carries a larger proportion of the thermal flux with respect to the mode number fraction. While δ^{eq} corresponds to only 1% of the total number of modes it contributes 9-20% of the flux. In contrast, δ^{uni} contributes $\sim 0.1\%$ of the total thermal flux outside the hotspot region. Thus, we surmise that the modes corresponding to large N-N bond stretch, in both the EQ and UNI classes, are capable of storing thermal energy. However, only the EQ class modes corresponding to δ^{eq} play a significant role in transporting energy from the hotspot. In contrast the modes constituting δ^{uni} are inefficient carriers of heat, therefore energy residing within these modes will remain localized to the hotspot region.

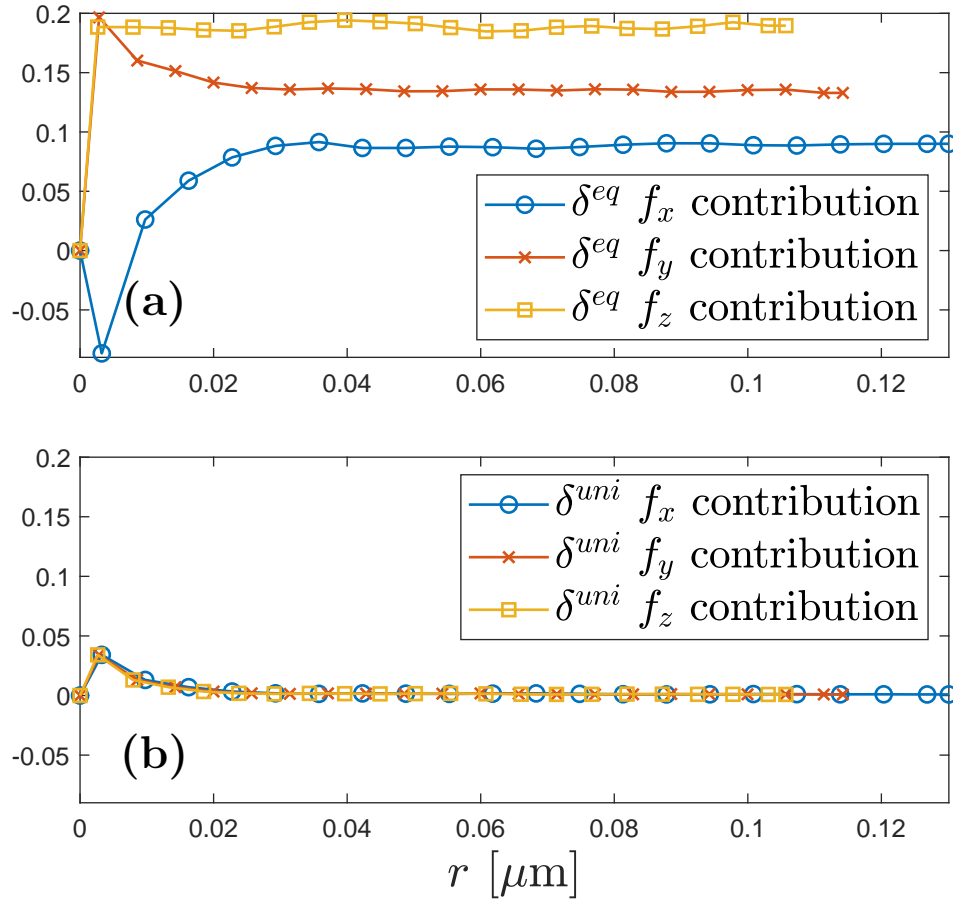


Figure 6.13: Contributions of (a) large EQ stretching modes and (b) large UNI stretching modes to the thermal flux along all three principal directions.

6.3.4 Verification of Hotspot Simulation

By demonstrating, for the first time, the viability of phonon Boltzmann modeling to simulate microscale thermal transport, these simulations represent a key advancement in the modeling of thermal processes of energetic molecular crystals. Therefore, while these simulation results demonstrate the feasibility of applying the phonon BTE to such materials, it is difficult to directly compare our results against

existing sources. However, we noted in sec. 6.3, that a number of important phonon properties, used as inputs to the phonon BTE simulation, compare well with previously reported values. Specifically, the specific heat is within a factor of two of the experimental value reported in [175], $4.11 \times 10^3 \text{kJ/m}^3\text{K}$ vs $1.96 \times 10^3 \text{kJ/m}^3\text{K}$, the group velocity versus frequency plots in fig. 6.3 are qualitatively similar to those in [22], and the thermal conductivity values match those reported in [171]. Therefore, we are reasonably certain that the phonon transport results accurately represent phonon flow in RDX.

6.4 Conclusion

The phonon parameters of α RDX have been determined throughout the entire BZ and their contributions to thermal transport analyzed. Significant anisotropy in the TC is reported with contributions both from microscale, as well as lattice, anisotropy. The TCA indicates contribution to the TC from phonon modes vary depending on the phonon frequency as well as direction of heat transport. We also present two metrics for determining the N-N bond stretch due to a certain phonon mode. These two metrics are based on whether the system is in equilibrium or non-equilibrium. The vast majority of modes contribute negligibly to N-N bonds stretch. We presented our initial findings for phonon lifetimes for all branches both at the BZ center as well as the BZ boundary. The phonon lifetimes are found to lie in the range of 1-40 ps. Finally we simulated microscale heat transport in the presence of a hotspot. We found that the optical modes contributed up to 75% of the total ther-

mal flux. Furthermore, the energy stored in phonon modes that correspond to large N-N bond stretch was nearly equal to the number fraction of such modes. Additionally, we found that phonon modes with large N-N bond stretch under equilibrium conditions contribute significantly, 8-20%, to thermal transport, while stretching modes determined from the non-equilibrium assumption contributed negligibly to thermal flux. This work represents our first steps to applying accurate atomic and microscale thermal simulation techniques to more accurately model the phonon processes involved in initiation of α RDX.

Chapter 7: Conclusion

Innovation and demand will continue to accelerate the proliferation of nano- and micro- scale phonon systems, notably in the form of solid-state devices. The associated thermal challenges, inherent at such submicron length scales, make accurate thermal modeling essential for engineering the next generation of devices. Among the various simulation approaches, the phonon BTE is uniquely equipped to capture the important physical processes relevant to phonon transport at the length scales of interest. However, prevailing BTE solution methodologies make a variety of simplifications and assumptions, creating need for improved thermal modeling methodologies. This dissertation introduced a finite volume-based methodology for the solution of the three-dimensional phonon Boltzmann transport equation accounting for full Brillouin zone phonon properties. This method enables accurate submicron length scale simulation of phonon transport in three dimensional domains while accounting for lattice, microscale, and macroscopic source of anisotropy. This methodology was applied to three important phonon systems i) studying the effect of disparate sources of anisotropy on the temperature field of a FinFET transistor, ii) investigating the competition between extrinsic and intrinsic scattering effects in the context of achieving sub-Casimir thermal flow in Si NWs, and iii) simulating

thermal transport in the vicinity of a hotspot in crystalline α RDX. We now review the contents of this dissertation, highlighting the main findings and contributions.

7.1 Summary and Contributions

Chapter 1 motivated the problem of microscale thermal transport modeling by highlighting a number of important materials, devices, and systems whose thermal behaviors are determined by phonon mechanisms. The prevailing computational approaches for modeling heat transport were discussed before singling out the phonon BTE as being best suited to the length scales of interest in this dissertation.

In Chapter 2 we began our discussion of phonon mediated thermal transport modeling by considering a simple one-dimensional crystalline system. Through this example we discussed the concept of a phonon as a carrier of thermal energy as well as highlighted the phonon parameters critical to thermal transport. In addition, intuition was developed regarding the degree to which phonons throughout the Brillouin zone participate in heat transfer. Practical approaches, utilizing freely available software, for determining phonon parameters and mode shapes in real crystalline systems were presented. Finally, we described the landscape of numerical solution techniques for the phonon BTE. Solution techniques may be roughly categorized by the thermal transport components they emphasize. We noted that due to the computational complexity associated with solving the phonon BTE, existing solution methods adopted a number of simplifications and/or assumptions in order to emphasize a certain component, or components. This led to varying degrees

of model fidelity.

In Chapter 3 we presented our recently developed finite volume-based methodology for the solution of the full Brillouin zone three-dimensional phonon BTE. Our approach allows for independent discretization of both the real *and* reciprocal space. Furthermore, the reciprocal space sampling approach directly incorporates Born von-Karman boundary conditions, while the phonon parameters that serve as inputs to the phonon BTE are determined throughout the full Brillouin zone (FBZ). Sampling the discrete allowed phonon modes arising due to Born von-Karman boundary condition, in conjunction with the calculation of FBZ phonon properties, allows our methodology to capture three disparate sources of anisotropy - lattice, microscale, and macroscopic.

This chapter included the following novel addition to the literature

- A comprehensive computational methodology for a finite volume-based solution of the three dimensional FBZ phonon BTE accounting for finite lattice effects. By incorporating finite lattice effects the methodology captures lattice, microscale, and macroscopic phonon flow anisotropy within three-dimensional submicron domains.

Chapter 4 applied our BTE solution methodology to a parameter study of a FinFET device. The temperature fields were calculated as the applied voltage and device dimensions were varied. We determined that use of a gray isotropic model underestimated the peak temperatures by roughly 10%, while using isotropic relaxation times *overestimated* the peak temperature by roughly 30%. These differences

highlighted the importance of using a full Brillouin zone representation to capture anisotropic flows in nanoscale devices.

This chapter contained the following novel additions to the literature

- A rigorous comparison of three different thermal models each capturing, to varying degrees, sources of phonon anisotropy. The comparisons were quantified by contrasting the three dimensional FinFET temperature fields predicted by each model.
- The cumulative effects of anisotropy captured in our FBZ model led to to $\sim 10\%$ difference in peak temperatures compared to a fully isotropic model.
- The cumulative effects of anisotropy captured in our FBZ model led to to $\sim 30\%$ difference in peak temperatures compared to an anisotropic model with gray relaxation times.

In Chapter 5 we investigated SiNWs of finite and infinite lengths possessing a simple periodic offset geometry. A number of recent studies have indicated that modifications to the SiNW boundaries are capable of creating significant thermal resistance, improving the utility of SiNWs as a thermoelectric component [107,139,140,148,154]. By increasing phonon backscattering our chamber-offset geometry was capable of reducing thermal conductivity by over 90% compared to a uniform cross-sectional SiNW of the same dimensions. In finite length NWs, the designs which maximize backscattering were also found to be the best candidate for improving the efficiency of thermoelectric systems. Finally, we found that the chamber-offset NW behaves as a high-pass phonon filter, attenuating low frequency phonons and, as a

result, forcing phonons with large frequencies to participate to a greater degree in thermal transport.

This chapter contained the following novel additions to the literature

- The chamber-offset NW geometry is capable of reducing thermal conductivity by $> 90\%$ compared to a uniform NW of identical cross-section. This exceeds the previous maximum reduction that was theoretically predicted in studies of Si NWs with a modified boundary geometry.
- The thermal conductivity accumulation in the infinite chamber-offset NW was calculated. It was found that small MFP ($< 1\mu m$) phonons carry 83% and 23% more energy in the smooth and rough chamber-offset NW, respectively, compared to their uniform counterparts.
- We demonstrated the potential utility of SiNWs as a phonon filter. The filtering effect is induced by the physical length scale imparted by the offset. The offset attenuates the thermal transport contribution from low frequency phonons, forcing phonons with large frequencies to participate to a greater degree in thermal transport.

Chapter 6 contains a study of phonon transport in the complex molecular crystal α RDX. It is well known that phonons play an integral role in initiation mechanisms of energetic materials [21, 22], however the complexity of the atomic structure in these systems has previously precluded study via the phonon BTE. For the first time we applied phonon Boltzmann modeling to the study of phonon transport in α RDX. Specifically, we simulated thermal transport in the vicinity of a hotspot,

a localized region of higher energy density where chemistry initiates. The phonon BTE modeling used full-band phonon lifetimes calculated using a normal mode decomposition approach [176]. Calculation of the full-band phonon lifetimes marks the first time the NMD approach was applied to α RDX. We parsed the contribution of individual modes to thermal transport, finding that optical modes transported the majority, 63%-78%, of thermal energy. Phonon modes that correspond to large N-N bond stretch, i.e. modes closely linked with initiation, were found to contribute differently to thermal transport depending on if the system was in equilibrium or out of equilibrium.

This chapter contained the following novel additions to the literature

- The FBZ phonon BTE simulation was applied to an energetic crystalline system composed of a complex (>100 atoms) unit cell to study phonon processes important to initiation. This marks the first application of phonon BTE modeling to study thermal transport in materials composed of unit cells with over 100 atoms.
- The thermal transport participation of phonon modes corresponding to large N-N bond stretch depends on the state of the system. In equilibrium, phonon modes contributing to significant N-N bond stretch carry $\sim 20\%$ of thermal energy. In the out of equilibrium case corresponding to uniform mode amplitudes, phonon modes contributing to significant N-N bond stretch carry $< 1\%$ of the thermal energy.

7.2 Future Research Directions

This work represents a first step toward accurate modeling of anisotropic three-dimensional phonon flows in nanostructures and complex materials. As such it invites the possibility of several future research directions.

a) Time Dependency of FBZ-3DBTE

Accurate measurement of submicron thermal transport phenomena has proved difficult using traditional experimental techniques due to the inherent time and length scales associated with phonons [43]. Over the past decade, pump-probe experiments, such as FDTR, TDTR, and TTG, have been used to calculate the material thermal conductivity accumulation function. These approaches use a laser pulse to create a nano- to micro- scale heating pattern that is on the same length scale of the phonon MFPs of a material. A subsequent probe laser is then used to measure the material thermal response, extracting information regarding how phonons of different MFPs contribute to thermal transport [80]. Extracting the MFP accumulation requires an intervening model in order to determine the phonon suppression function. Specifically, one needs to know to what degree modal contribution to thermal transport is suppressed due to the sub-micrometer length scale associated with the heating region. In general this suppression is assumed to be a function of the phonon mode MFP. The BTE is an excellent candidate for calculation of this suppression function. Due to the inherent time-scales associated with the pump and probe laser pulses, simulation via the BTE requires consideration of

the time dependent nature of phonon transport. Only a small number of studies have attempted to apply the phonon BTE to this problem [43, 177]. Notably these approaches have assumed the material thermal conductivity is isotropic. Thus, a time dependent FBZ-BTE solution could be applied to calculation of the suppression function in a more general class of anisotropic materials, allowing for accurate TDTR predictions of the thermal conductivity accumulation in anisotropic systems.

b) Experimental Observation of Phonon Filter

The simulation results of Chapter 5 indicate that the chamber-offset NW functions as a high-pass phonon filter. A phonon filter selectively restricts the mechanical waves which can pass through a material based on the waves frequency. However, phonon filters have yet to be demonstrated experimentally. The principles challenge associated with the physical realization of a phonon filter is quantifying the filtering effect. Essentially, one needs to experimentally demonstrate that the chamber offset NW attenuates low frequency phonons while leaving the larger frequencies relatively unaffected. A natural measure of the relative contribution of phonons throughout the frequency spectrum is the thermal conductivity accumulation function. Candidate experimental techniques include TDTR, FDTR, and TTG. However, these approaches have been primarily used to measure normal and lateral thermal transport in simple thin films. Therefore, work remains to successfully adapt these experimental approaches to experimentally demonstrate phonon filtering in a chamber-offset NW.

c) Improvements to Phonon Modeling in Large-Unit Cell Systems

Compared to simple atomic crystals, crystalline materials with large unit cells, such as many energetic materials, have been the subject of relatively few phonon BTE studies. A primary obstacle to the study of these systems was the large number of phonon branches that are present when the unit cell is large. In this work we explicitly modeled the contribution of all 504 branches in RDX. However, an important issue when modeling large unit-celled crystals is the question of disorder. Despite the fact that these systems are crystalline, the disorder *within* the unit cell may cause a prevalence of non-propagating phonon modes. Such phonon modes are not well described by the phonon BTE, which assumes that all modes have a defined group velocity and MFP [178, 179]. Thus modifications to the existing BTE methodology may be required for systems with a large number of so-called diffuson and locon vibrational modes [180]. These modification may include the definition of an effective group velocity and MFP for non-propagating vibrational modes. Alternatively, a hybrid approach may be applied where the propagating modes are treated used a phonon BTE formulation, while non-propagating modes are handled in a different manner, for example using the theory developed by Allen and Feldman for thermal transport in disordered materials [179–181]. Regardless of the specific approach, the first step is to classify the vibrational modes of the system of interest in order to determine whether special care is required. Recent work by Seyf and Asugen proposed a general classification system for determining the propagons, diffusons, and locons of any weakly disordered periodic system [182].

These future research directions will enable more efficient solid-state devices and improve fundamental knowledge of phonon transport processes.

Bibliography

- [1] M Asen-Palmer, K Bartkowski, E Gmelin, M Cardona, AP Zhernov, AV Inyushkin, A Taldenkov, VI Ozhogin, Kohei M Itoh, and EE Haller. Thermal conductivity of germanium crystals with different isotopic compositions. *Physical review B*, 56(15):9431, 1997.
- [2] Andrew R Brown, Nicolas Daval, Konstantin K Bourdelle, B-Y Nguyen, and Asen Asenov. Comparative simulation analysis of process-induced variability in nanoscale soi and bulk trigate finfets. *IEEE Transactions on Electron Devices*, 60(11):3611–3617, 2013.
- [3] David G Cahill, Wayne K Ford, Kenneth E Goodson, Gerald D Mahan, Arun Majumdar, Humphrey J Maris, Roberto Merlin, and Simon R Phillpot. Nanoscale thermal transport. *Journal of Applied Physics*, 93(2):793–818, 2003.
- [4] David G. Cahill, Paul V. Braun, Gang Chen, David R. Clarke, Shanhui Fan, Kenneth E. Goodson, Pawel Koblinski, William P. King, Gerald D. Mahan, Arun Majumdar, Humphrey J. Maris, Simon R. Phillpot, Eric Pop, and Li Shi. Nanoscale thermal transport. II. 2003-2012. *Applied Physics Reviews*, 1(1):011305, mar 2014.
- [5] Yang-Kyu Choi, Daewon Ha, Eric Snow, Jeffrey Bokor, and Tsu-Jae King. Reliability study of cmos finfets. In *Electron Devices Meeting, 2003. IEDM'03 Technical Digest. IEEE International*, pages 7–6. IEEE, 2003.
- [6] Mayank Shrivastava, Manish Agrawal, Sunny Mahajan, Harald Gossner, Thomas Schulz, Dinesh Kumar Sharma, and V Ramgopal Rao. Physical insight toward heat transport and an improved electrothermal modeling framework for finfet architectures. *Electron Devices, IEEE Transactions on*, 59(5):1353–1363, 2012.
- [7] M. Asheghi, Y. K. Leung, S. S. Wong, and K. E. Goodson. Phonon-boundary scattering in thin silicon layers. *Applied Physics Letters*, 71(13):1798–1800, sep 1997.

- [8] PG Sverdrup, S Sinha, M Asheghi, S Uma, and KE Goodson. Measurement of ballistic phonon conduction near hotspots in silicon. *Applied Physics Letters*, 78(21):3331–3333, 2001.
- [9] Jeremy Rowlette, Eric Pop, Sanjiv Sinha, Mathew Panzer, and Kenneth Goodson. Thermal phenomena in deeply scaled mosfets. *IEDM Tech. Dig*, 2005:984–987, 2005.
- [10] Jeremy A. Rowlette and Kenneth E. Goodson. Fully coupled nonequilibrium electron-phonon transport in nanometer-scale silicon FETs. *IEEE Transactions on Electron Devices*, 55(1):220–232, jan 2008.
- [11] Adam Christensen and Samuel Graham. Multiscale lattice boltzmann modeling of phonon transport in crystalline semiconductor materials. *Numerical Heat Transfer, Part B: Fundamentals*, 57(2):89–109, 2010.
- [12] Sreekant V Narumanchi, Jayathi Y Murthy, and Cristina H Amon. Comparison of different phonon transport models for predicting heat conduction in silicon-on-insulator transistors. *Journal of Heat Transfer*, 127(7):713–723, 2005.
- [13] Allon I. Hochbaum and Peidong Yang. Semiconductor nanowires for energy conversion. *Chemical Reviews*, 110(1):527–546, jan 2010.
- [14] Zhiting Tian, Sangyeop Lee, and Gang Chen. COMPREHENSIVE REVIEW OF HEAT TRANSFER IN THERMOELECTRIC MATERIALS AND DEVICES. *Annual Review of Heat Transfer*, 17(N/A):425–483, 2014.
- [15] S.-M. Lee, David G. Cahill, and Rama Venkatasubramanian. Thermal conductivity of si-ge superlattices. *Applied Physics Letters*, 70(22):2957–2959, jun 1997.
- [16] G. Chen, A. Narayanaswamy, and C. Dames. Engineering nanoscale phonon and photon transport for direct energy conversion. *Superlattices and Microstructures*, 35(3-6):161–172, mar 2004.
- [17] A. J. Minnich, H. Lee, X. W. Wang, G. Joshi, M. S. Dresselhaus, Z. F. Ren, G. Chen, and D. Vashaee. Modeling study of thermoelectric SiGe nanocomposites. *Physical Review B*, 80(15), oct 2009.
- [18] B. Poudel, Q. Hao, Y. Ma, Y. Lan, A. Minnich, B. Yu, X. Yan, D. Wang, A. Muto, D. Vashaee, X. Chen, J. Liu, M. S. Dresselhaus, G. Chen, and Z. Ren. High-thermoelectric performance of nanostructured bismuth antimony telluride bulk alloys. *Science*, 320(5876):634–638, may 2008.
- [19] Allon I. Hochbaum, Renkun Chen, Raul Diaz Delgado, Wenjie Liang, Erik C. Garnett, Mark Najarian, Arun Majumdar, and Peidong Yang. Enhanced thermoelectric performance of rough silicon nanowires. *Nature*, 451(7175):163–167, jan 2008.

- [20] Kedar Hippalgaonkar, Baoling Huang, Renkun Chen, Karma Sawyer, Peter Ercius, and Arun Majumdar. Fabrication of microdevices with integrated nanowires for investigating low-dimensional phonon transport. *Nano Letters*, 10(11):4341–4348, nov 2010.
- [21] Dana D. Dlott and Michael D. Fayer. Shocked molecular solids: Vibrational up pumping, defect hot spot formation, and the onset of chemistry. *The Journal of Chemical Physics*, 92(6):3798–3812, mar 1990.
- [22] B. Kraczek and P. W. Chung. Investigation of direct and indirect phonon-mediated bond excitation in ardx. *The Journal of Chemical Physics*, 138(7):074505, feb 2013.
- [23] Dana D. Dlott. MULTI-PHONON UP-PUMPING IN ENERGETIC MATERIALS. In *Overviews of Recent Research on Energetic Materials*, pages 303–333. WORLD SCIENTIFIC, aug 2005.
- [24] Andrey Pereverzev, Thomas D. Sewell, and Donald L. Thompson. Molecular dynamics study of the pressure-dependent terahertz infrared absorption spectrum of α - and γ -RDX. *The Journal of Chemical Physics*, 139(4):044108, jul 2013.
- [25] Kaushik Joshi, Martin Losada, and Santanu Chaudhuri. Intermolecular energy transfer dynamics at a hot-spot interface in RDX crystals. *The Journal of Physical Chemistry A*, 120(4):477–489, jan 2016.
- [26] Laurence E. Fried and Anthony J. Ruggiero. Energy transfer rates in primary, secondary, and insensitive explosives. *The Journal of Physical Chemistry*, 98(39):9786–9791, sep 1994.
- [27] K. L. McNesby and C. S. Coffey. Spectroscopic determination of impact sensitivities of explosives. *The Journal of Physical Chemistry B*, 101(16):3097–3104, apr 1997.
- [28] Shuji Ye, Kenichi Tonokura, and Mitsuo Koshi. Vibron dynamics in rdx, hmx and tetryl crystals. *Chemical Physics*, 293(1):1–8, aug 2003.
- [29] Ye and Mitsuo Koshi. Theoretical studies of energy transfer rates of secondary explosives. *The Journal of Physical Chemistry B*, 110(37):18515–18520, sep 2006.
- [30] Francis G. VanGessel and Peter W. Chung. An anisotropic full brillouin zone model for the three dimensional phonon boltzmann transport equation. *Computer Methods in Applied Mechanics and Engineering*, 317:1012–1036, apr 2017.
- [31] R. PEIERLS. On the kinetic theory of thermal conduction in crystals. In *Selected Scientific Papers of Sir Rudolf Peierls*, pages 15–48. CO-PUBLISHED

BY IMPERIAL COLLEGE PRESS AND WORLD SCIENTIFIC PUBLISHING CO., apr 1997.

- [32] Tom Klitsner, J. E. VanCleve, Henry E. Fischer, and R. O. Pohl. Phonon radiative heat transfer and surface scattering. *Physical Review B*, 38(11):7576–7594, oct 1988.
- [33] ASME Majumdar. Microscale heat conduction in dielectric thin films. *Journal of Heat Transfer*, 115(1):7–16, 1993.
- [34] Chunjian Ni and Jayathi Y Murthy. Phonon transport modeling using boltzmann transport equation with anisotropic relaxation times. *Journal of Heat Transfer*, 134(8):082401, 2012.
- [35] Sreekant VJ Narumanchi, Jayathi Y Murthy, and Cristina H Amon. Boltzmann transport equation-based thermal modeling approaches for hotspots in microelectronics. *Heat and mass transfer*, 42(6):478–491, 2006.
- [36] Jean-Philippe M Péraud and Nicolas G Hadjiconstantinou. Efficient simulation of multidimensional phonon transport using energy-based variance-reduced monte carlo formulations. *Physical Review B*, 84(20):205331, 2011.
- [37] Jean-Philippe M. Péraud and Nicolas G. Hadjiconstantinou. An alternative approach to efficient simulation of micro/nanoscale phonon transport. *Applied Physics Letters*, 101(15):153114, oct 2012.
- [38] Syed Ashraf Ali, Gautham Kollu, Sandip Mazumder, P Sadayappan, and Arpit Mittal. Large-scale parallel computation of the phonon boltzmann transport equation. *International Journal of Thermal Sciences*, 86:341–351, 2014.
- [39] Syed Ashraf Ali and Sandip Mazumder. Phonon heat conduction in multidimensional heterostructures: predictions using the boltzmann transport equation. *Journal of Heat Transfer*, 137(10):102401, 2015.
- [40] JY Murthy and SR Mathur. An improved computational procedure for sub-micron heat conduction. In *ASME 2002 International Mechanical Engineering Congress and Exposition*, pages 75–84. American Society of Mechanical Engineers, 2002.
- [41] Per G Sverdrup, Y Sungtaek Ju, and Kenneth E Goodson. Sub-continuum simulations of heat conduction in silicon-on-insulator transistors. *Journal of Heat Transfer*, 123(1):130–137, 2001.
- [42] Sandip Mazumder and Arunava Majumdar. Monte carlo study of phonon transport in solid thin films including dispersion and polarization. *Journal of Heat Transfer*, 123(4):749, 2001.

- [43] Syed Ashraf Ali and Sandip Mazumder. Phonon boltzmann transport equation based modeling of time domain thermo-reflectance experiments. *International Journal of Heat and Mass Transfer*, 107:607–621, apr 2017.
- [44] Pareekshith Allu and Sandip Mazumder. Hybrid ballistic-diffusive solution to the frequency-dependent phonon boltzmann transport equation. *International Journal of Heat and Mass Transfer*, 100:165–177, sep 2016.
- [45] Daniel P Sellan, JE Turney, Alan JH McGaughey, and Cristina H Amon. Cross-plane phonon transport in thin films. *Journal of Applied Physics*, 108(11):113524, 2010.
- [46] Francis G. VanGessel and Peter W. Chung. Phonon backscatter, trapping, and misalignment effects on microscale thermal conductance below the casimir limit. *International Journal of Heat and Mass Transfer*, 128:807–816, jan 2019.
- [47] Francis VanGessel, Jie Peng, and Peter W. Chung. A review of computational phononics: the bulk, interfaces, and surfaces. *Journal of Materials Science*, 53(8):5641–5683, oct 2017.
- [48] Francis G VanGessel, Gaurav Kumar, Daniel C Elton, and Peter W Chung. A phonon boltzmann study of microscale thermal transport in ardx cook-off. *arXiv preprint arXiv:1808.08295*, 2018.
- [49] PG Klemens. The thermal conductivity of dielectric solids at low temperatures (theoretical). In *Proceedings of the Royal Society of London A: Mathematical, Physical and Engineering Sciences*, volume 208, pages 108–133. The Royal Society, 1951.
- [50] G.P. Srivastava. *The Physics of Phonons*. Taylor and Francis Group, 270 Madison Avenue New York, NY 10016, 1990.
- [51] V. L. Gurevich. *Transport in Phonon Systems*. North-Holland Physics Publishing, 1000 AC Amsterdam, Netherlands, 1986.
- [52] Martin T Dove and Martin T Dove. *Introduction to lattice dynamics*, volume 4. Cambridge university press, 1993.
- [53] D. A. Broido, M. Malorny, G. Birner, Natalio Mingo, and D. A. Stewart. Intrinsic lattice thermal conductivity of semiconductors from first principles. *Applied Physics Letters*, 91(23):231922, dec 2007.
- [54] D. A. Broido and T. L. Reinecke. Lattice thermal conductivity of superlattice structures. *Physical Review B*, 70(8), aug 2004.
- [55] M Omini and A Sparavigna. An iterative approach to the phonon boltzmann equation in the theory of thermal conductivity. *Physica B: Condensed Matter*, 212(2):101–112, jul 1995.

- [56] Aleksandr Chernatynskiy and Simon R Phillpot. Evaluation of computational techniques for solving the boltzmann transport equation for lattice thermal conductivity calculations. *Physical Review B*, 82(13):134301, 2010.
- [57] Colin D. Landon and Nicolas G. Hadjiconstantinou. Deviational simulation of phonon transport in graphene ribbons with ab initio scattering. *Journal of Applied Physics*, 116(16):163502, oct 2014.
- [58] Rodrigo A. Escobar and Cristina H. Amon. Thin film phonon heat conduction by the dispersion lattice boltzmann method. *Journal of Heat Transfer*, 130(9):092402, 2008.
- [59] Gang Chen. Nanoscale energy transport and conversion. 2005.
- [60] N. W. Ashcroft and N. D Mermin. *Solid State Physics*. Saunders College Publishers, 1976.
- [61] Joseph E Turney, Alan JH McGaughey, and Cristina H Amon. In-plane phonon transport in thin films. *Journal of Applied Physics*, 107(2):024317, 2010.
- [62] Nazli Donmez and Samuel Graham. A multiscale thermal modeling approach for ballistic and diffusive heat transport in two dimensional domains. *International Journal of Thermal Sciences*, 76:235–244, feb 2014.
- [63] K. T. Regner, A. J. H. McGaughey, and J. A. Malen. Analytical interpretation of nondiffusive phonon transport in thermoreflectance thermal conductivity measurements. *Physical Review B*, 90(6), aug 2014.
- [64] Jeremy A. Johnson, A. A. Maznev, John Cuffe, Jeffrey K. Eliason, Austin J. Minnich, Timothy Kehoe, Clivia M. Sotomayor Torres, Gang Chen, and Keith A. Nelson. Direct measurement of room-temperature nondiffusive thermal transport over micron distances in a silicon membrane. *Physical Review Letters*, 110(2), jan 2013.
- [65] Fan Yang and Chris Dames. Mean free path spectra as a tool to understand thermal conductivity in bulk and nanostructures. *Physical Review B*, 87(3), jan 2013.
- [66] Aydin Nabovati, Daniel P Sellan, and Cristina H Amon. On the lattice boltzmann method for phonon transport. *Journal of Computational Physics*, 230(15):5864–5876, 2011.
- [67] Michael F Modest. *Radiative heat transfer*. Academic press, 2013.
- [68] Rodrigo A. Escobar and Cristina H. Amon. Influence of phonon dispersion on transient thermal response of silicon-on-insulator transistors under self-heating conditions. *Journal of Heat Transfer*, 129(7):790, 2007.

- [69] Pekka Heino. Lattice-boltzmann finite-difference model with optical phonons for nanoscale thermal conduction. *Computers & Mathematics with Applications*, 59(7):2351–2359, apr 2010.
- [70] Zhaoli Guo and Kun Xu. Discrete unified gas kinetic scheme for multiscale heat transfer based on the phonon boltzmann transport equation. *International Journal of Heat and Mass Transfer*, 102:944–958, nov 2016.
- [71] J. Y. Murthy and S. R. Mathur. Computation of sub-micron thermal transport using an unstructured finite volume method. *Journal of Heat Transfer*, 124(6):1176, 2002.
- [72] Chunjian Ni and Jayathi Y Murthy. Parallel computation of the phonon boltzmann transport equation. *Numerical Heat Transfer, Part B: Fundamentals*, 55(6):435–456, 2009.
- [73] Sreekant VJ Narumanchi, Jayathi Y Murthy, and Cristina H Amon. Sub-micron heat transport model in silicon accounting for phonon dispersion and polarization. *Journal of Heat Transfer*, 126(6):946–955, 2004.
- [74] Arpit Mittal and Sandip Mazumder. Monte carlo study of phonon heat conduction in silicon thin films including contributions of optical phonons. *Journal of Heat Transfer*, 132(5):052402, 2010.
- [75] Zahra Shomali, Behrad Pedar, Jafar Ghazanfarian, and Abbas Abbasi. Monte-carlo parallel simulation of phonon transport for 3d silicon nano-devices. *International Journal of Thermal Sciences*, 114:139–154, apr 2017.
- [76] Lina Yang and Austin J. Minnich. Thermal transport in nanocrystalline si and SiGe by ab initio based monte carlo simulation. *Scientific Reports*, 7(1), mar 2017.
- [77] David Lacroix, Karl Joulain, and Denis Lemonnier. Monte carlo transient phonon transport in silicon and germanium at nanoscales. *Physical Review B*, 72(6):064305, 2005.
- [78] Eric Pop, Robert W Dutton, and Kenneth E Goodson. Analytic band monte carlo model for electron transport in si including acoustic and optical phonon dispersion. *Journal of Applied Physics*, 96(9):4998–5005, 2004.
- [79] G. Chen. Nonlocal and nonequilibrium heat conduction in the vicinity of nanoparticles. *Journal of Heat Transfer*, 118(3):539, 1996.
- [80] Keith T. Regner, Justin P. Freedman, and Jonathan A. Malen. Advances in studying phonon mean free path dependent contributions to thermal conductivity. *Nanoscale and Microscale Thermophysical Engineering*, 19(3):183–205, may 2015.

- [81] John Cuffe, Jeffrey K. Eliason, A. A. Maznev, Kimberlee C. Collins, Jeremy A. Johnson, Andrey Shchepetov, Mika Prunnila, Jouni Ahopelto, Clivia M. Sotomayor Torres, Gang Chen, and Keith A. Nelson. Reconstructing phonon mean-free-path contributions to thermal conductivity using nanoscale membranes. *Physical Review B*, 91(24), jun 2015.
- [82] A J Minnich. Advances in the measurement and computation of thermal phonon transport properties. *Journal of Physics: Condensed Matter*, 27(5):053202, jan 2015.
- [83] Joseph Callaway. Model for lattice thermal conductivity at low temperatures. *Physical Review*, 113(4):1046, 1959.
- [84] Subhash L Shindé and Gyaneshwar P Srivastava. *Length-scale dependent phonon interactions*, volume 10. Springer, 2014.
- [85] M Omini and A Sparavigna. Beyond the isotropic-model approximation in the theory of thermal conductivity. *Physical Review B*, 53(14):9064, 1996.
- [86] M Omini and A Sparavigna. Heat transport in dielectric solids with diamond structure. *NUOVO CIMENTO-SOCIETA ITALIANA DI FISICA SEZIONE D*, 19:1537–1564, 1997.
- [87] A Sparavigna. Role of nonpairwise interactions on phonon thermal transport. *Physical Review B*, 67(14):144305, 2003.
- [88] DA Broido, A Ward, and N Mingo. Lattice thermal conductivity of silicon from empirical interatomic potentials. *Physical Review B*, 72(1):014308, 2005.
- [89] L. Lindsay, D. A. Broido, and T. L. Reinecke. Ab initio thermal transport in compound semiconductors. *Physical Review B*, 87(16), apr 2013.
- [90] Alistair Ward, DA Broido, Derek A Stewart, and Gernot Deinzer. Ab initio theory of the lattice thermal conductivity in diamond. *Physical Review B*, 80(12):125203, 2009.
- [91] L. Lindsay, D. A. Broido, and Natalio Mingo. Flexural phonons and thermal transport in graphene. *Physical Review B*, 82(11), sep 2010.
- [92] Zhiting Tian, Jivtesh Garg, Keivan Esfarjani, Takuma Shiga, Junichiro Shiomi, and Gang Chen. Phonon conduction in PbSe, PbTe, and PbTe_{1-x}Sex from first-principles calculations. *Physical Review B*, 85(18), may 2012.
- [93] Matthew P. Kroonblawd and Thomas D. Sewell. Anisotropic relaxation of idealized hot spots in crystalline 1, 3, 5-triamino-2, 4, 6-trinitrobenzene (TATB). *The Journal of Physical Chemistry C*, 120(31):17214–17223, jul 2016.

- [94] Edward F. C. Byrd, Gustavo E. Scuseria, and Cary F. Chabalowski. An ab initio study of solid nitromethane, HMX, RDX, and CL20: successes and failures of DFT. *The Journal of Physical Chemistry B*, 108(35):13100–13106, sep 2004.
- [95] Yao Long and Jun Chen. Theoretical study of the phonon-phonon scattering mechanism and the thermal conductive coefficients for energetic material. *Philosophical Magazine*, 97(28):2575–2595, jul 2017.
- [96] YS Ju and KE Goodson. Phonon scattering in silicon films with thickness of order 100 nm. *Applied Physics Letters*, 74(20):3005–3007, 1999.
- [97] I.T.R.S., International Technology Roadmap for Semiconductors, 2014.
- [98] John M Ziman. *Electrons and phonons: the theory of transport phenomena in solids*. Oxford University Press, 1960.
- [99] Hossein Karamitaheri, Neophytos Neophytou, and Hans Kosina. Ballistic phonon transport in ultra-thin silicon layers: Effects of confinement and orientation. *Journal of Applied Physics*, 113(20):204305, may 2013.
- [100] Z Aksamija and I Knezevic. Anisotropy and boundary scattering in the lattice thermal conductivity of silicon nanomembranes. *Physical Review B*, 82(4):045319, 2010.
- [101] Xinjiang Wang and Baoling Huang. Computational study of in-plane phonon transport in si thin films. *Scientific Reports*, 4(1), sep 2014.
- [102] D. P. Sellan, J. E. Turney, A. J. H. McGaughey, and C. H. Amon. Cross-plane phonon transport in thin films. *Journal of Applied Physics*, 108(11):113524, dec 2010.
- [103] A. J. Minnich. Thermal phonon boundary scattering in anisotropic thin films. *Applied Physics Letters*, 107(18):183106, nov 2015.
- [104] Ruikang Wu, Run Hu, and Xiaobing Luo. First-principle-based full-dispersion monte carlo simulation of the anisotropic phonon transport in the wurtzite GaN thin film. *Journal of Applied Physics*, 119(14):145706, apr 2016.
- [105] Z. Chen, Z. Wei, Y. Chen, and C. Dames. Anisotropic debye model for the thermal boundary conductance. *Physical Review B*, 87(12), mar 2013.
- [106] Isabelle Ferain, Cynthia A Colinge, and Jean-Pierre Colinge. Multigate transistors as the future of classical metal-oxide-semiconductor field-effect transistors. *Nature*, 479(7373):310–316, 2011.
- [107] Jeremie Maire, Roman Anufriev, Takuma Hori, Junichiro Shiomi, Sebastian Volz, and Masahiro Nomura. Thermal conductivity reduction in silicon fishbone nanowires. *Scientific Reports*, 8(1), mar 2018.

- [108] Woosung Park, Dongsuk D. Shin, Soo Jin Kim, Joseph S. Katz, Joonsuk Park, Chae Hyuck Ahn, Takashi Kodama, Mehdi Asheghi, Thomas W. Kenny, and Kenneth E. Goodson. Phonon conduction in silicon nanobeams. *Applied Physics Letters*, 110(21):213102, may 2017.
- [109] Roman Anufriev, Aymeric Ramiere, Jeremie Maire, and Masahiro Nomura. Heat guiding and focusing using ballistic phonon transport in phononic nanostructures. *Nature Communications*, 8:15505, may 2017.
- [110] Arden L. Moore, Sanjoy K. Saha, Ravi S. Prasher, and Li Shi. Phonon backscattering and thermal conductivity suppression in sawtooth nanowires. *Applied Physics Letters*, 93(8):083112, aug 2008.
- [111] Navaneetha K. Ravichandran and Austin J. Minnich. Coherent and incoherent thermal transport in nanomeshes. *Physical Review B*, 89(20), may 2014.
- [112] Jaeho Lee, Woochul Lee, Geoff Wehmeyer, Scott Dhuey, Deirdre L. Olynick, Stefano Cabrini, Chris Dames, Jeffrey J. Urban, and Peidong Yang. Investigation of phonon coherence and backscattering using silicon nanomeshes. *Nature Communications*, 8:14054, jan 2017.
- [113] Joseph Callaway. *Quantum theory of the solid state*. Academic Press, 2013.
- [114] Jintai Chung and GM Hulbert. A time integration algorithm for structural dynamics with improved numerical dissipation: the generalized- α method. *Journal of applied mechanics*, 60(2):371–375, 1993.
- [115] Robert E. Peierls. *Quantum Theory of Solids*. Oxford University Press, Amen House, London E.C.4, 1 edition, 1955.
- [116] Suhas Patankar. *Numerical heat transfer and fluid flow*. CRC press, 1980.
- [117] Arpit Mittal and Sandip Mazumder. Hybrid discrete ordinatesspherical harmonics solution to the boltzmann transport equation for phonons for non-equilibrium heat conduction. *Journal of Computational Physics*, 230(18):6977–7001, 2011.
- [118] Navaneetha K. Ravichandran and Austin J. Minnich. Role of thermalizing and nonthermalizing walls in phonon heat conduction along thin films. *Physical Review B*, 93(3), jan 2016.
- [119] Max Born and Kun Huang. *Dynamical theory of crystal lattices*. Clarendon Press, 1954.
- [120] Julian D Gale and Andrew L Rohl. The general utility lattice program (gulp). *Molecular Simulation*, 29(5):291–341, 2003.
- [121] C. Kittel. *Introduction to Solid State Physics*. John Wiley & Sons, Inc., New York, 1996.

- [122] MG Holland. Analysis of lattice thermal conductivity. *Physical Review*, 132(6):2461, 1963.
- [123] A Ward and DA Broido. Intrinsic phonon relaxation times from first-principles studies of the thermal conductivities of si and ge. *Physical Review B*, 81(8):085205, 2010.
- [124] Max A Heaslet and Robert F Warming. Radiative transport and wall temperature slip in an absorbing planar medium. *International Journal of Heat and Mass Transfer*, 8(7):979–994, 1965.
- [125] M Necati Özışık. *Radiative transfer and interactions with conduction and convection*. Werbel & Peck, 1973.
- [126] Henk Kaarle Versteeg and Weeratunge Malalasekera. *An introduction to computational fluid dynamics: the finite volume method*. Pearson Education, 2007.
- [127] Eric Pop, Robert W Dutton, and Kenneth E Goodson. Monte carlo simulation of joule heating in bulk and strained silicon. *Applied Physics Letters*, 86(8):082101, 2005.
- [128] Junichiro Shiomi. Research update: Phonon engineering of nanocrystalline silicon thermoelectrics. *APL Materials*, 4(10):104504, sep 2016.
- [129] Zhi-Gang Chen, Guang Han, Lei Yang, Lina Cheng, and Jin Zou. Nanostructured thermoelectric materials: Current research and future challenge. *Progress in Natural Science: Materials International*, 22(6):535–549, dec 2012.
- [130] Amy M. Marconnet, Mehdi Asheghi, and Kenneth E. Goodson. From the casimir limit to phononic crystals: 20 years of phonon transport studies using silicon-on-insulator technology. *Journal of Heat Transfer*, 135(6):061601, may 2013.
- [131] H.B.G. Casimir. Note on the conduction of heat in crystals. *Physica*, 5(6):495–500, jun 1938.
- [132] E. H. Sondheimer. The mean free path of electrons in metals. *Advances in Physics*, 50(6):499–537, sep 2001.
- [133] Hossein Honarvar and Mahmoud I. Hussein. Spectral energy analysis of locally resonant nanophononic metamaterials by molecular simulations. *Physical Review B*, 93(8), feb 2016.
- [134] R. Anufriev, R. Yanagisawa, and M. Nomura. Aluminium nanopillars reduce thermal conductivity of silicon nanobeams. *Nanoscale*, 9(39):15083–15088, 2017.

- [135] Masahiro Nomura, Junki Nakagawa, Yuta Kage, Jeremie Maire, Dominik Moser, and Oliver Paul. Thermal phonon transport in silicon nanowires and two-dimensional phononic crystal nanostructures. *Applied Physics Letters*, 106(14):143102, apr 2015.
- [136] Giuseppe Romano and Alexie M. Kolpak. Thermal anisotropy enhanced by phonon size effects in nanoporous materials. *Applied Physics Letters*, 110(9):093104, feb 2017.
- [137] B. Fu, G. H. Tang, and C. Bi. Thermal conductivity in nanostructured materials and analysis of local angle between heat fluxes. *Journal of Applied Physics*, 116(12):124310, sep 2014.
- [138] Giuseppe Romano and Jeffrey C. Grossman. Toward phonon-boundary engineering in nanoporous materials. *Applied Physics Letters*, 105(3):033116, jul 2014.
- [139] A. I. Cocemasov, D. L. Nika, V. M. Fomin, D. Grimm, and O. G. Schmidt. Phonon-engineered thermal transport in si wires with constant and periodically modulated cross-sections: A crossover between nano- and microscale regimes. *Applied Physics Letters*, 107(1):011904, jul 2015.
- [140] Christophe Blanc, Ali Rajabpour, Sebastian Volz, Thierry Fournier, and Olivier Bourgeois. Phonon heat conduction in corrugated silicon nanowires below the casimir limit. *Applied Physics Letters*, 103(4):043109, jul 2013.
- [141] Zhiyong Wei, Geoff Wehmeyer, Chris Dames, and Yunfei Chen. Geometric tuning of thermal conductivity in three-dimensional anisotropic phononic crystals. *Nanoscale*, 8(37):16612–16620, 2016.
- [142] Xiao Wang Zhou, Reese E. Jones, Christopher James Kimmer, John C. Duda, and Patrick E. Hopkins. Relationship of thermal boundary conductance to structure from an analytical model plus molecular dynamics simulations. *Physical Review B*, 87(9), mar 2013.
- [143] Jinlong Ma, XinJiang Wang, Baoling Huang, and Xiaobing Luo. Effects of point defects and dislocations on spectral phonon transport properties of wurtzite GaN. *Journal of Applied Physics*, 114(7):074311, aug 2013.
- [144] Samuel C. Huberman, Jason M. Larkin, Alan J. H. McGaughey, and Cristina H. Amon. Disruption of superlattice phonons by interfacial mixing. *Physical Review B*, 88(15), oct 2013.
- [145] Jongwoo Lim, Kedar Hippalgaonkar, Sean C. Andrews, Arun Majumdar, and Peidong Yang. Quantifying surface roughness effects on phonon transport in silicon nanowires. *Nano Letters*, 12(5):2475–2482, apr 2012.

- [146] Deyu Li, Yiying Wu, Philip Kim, Li Shi, Peidong Yang, and Arun Majumdar. Thermal conductivity of individual silicon nanowires. *Applied Physics Letters*, 83(14):2934–2936, oct 2003.
- [147] C. J. Glassbrenner and Glen A. Slack. Thermal conductivity of silicon and germanium from 3k to the melting point. *Physical Review*, 134(4A):A1058–A1069, may 1964.
- [148] Vladimir Poborchii, Yukinori Morita, Junichi Hattori, Tetsuya Tada, and Pavel I. Geshev. Corrugated si nanowires with reduced thermal conductivity for wide-temperature-range thermoelectricity. *Journal of Applied Physics*, 120(15):154304, oct 2016.
- [149] X. Zianni and P. Chantrenne. Thermal conductivity of diameter-modulated silicon nanowires within a frequency-dependent model for phonon boundary scattering. *Journal of Electronic Materials*, 42(7):1509–1513, oct 2012.
- [150] Xanthippi Zianni. Diameter-modulated nanowires as candidates for high thermoelectric energy conversion efficiency. *Applied Physics Letters*, 97(23):233106, dec 2010.
- [151] Xanthippi Zianni. The effect of the modulation shape in the ballistic thermal conductance of modulated nanowires. *Journal of Solid State Chemistry*, 193:53–57, sep 2012.
- [152] Xanthippi Zianni, Valentin Jean, Konstantinos Termentzidis, and David Lacroix. Scaling behavior of the thermal conductivity of width-modulated nanowires and nanofilms for heat transfer control at the nanoscale. *Nanotechnology*, 25(46):465402, oct 2014.
- [153] Maxime Verdier, David Lacroix, and Konstantinos Termentzidis. Heat transport in phononic-like membranes: Modeling and comparison with modulated nano-wires. *International Journal of Heat and Mass Transfer*, 114:550–558, nov 2017.
- [154] Woosung Park, Giuseppe Romano, Ethan C. Ahn, Takashi Kodama, Joonsuk Park, Michael T. Barako, Joon Sohn, Soo Jin Kim, Jungwan Cho, Amy M. Marconnet, Mehdi Asheghi, Alexie M. Kolpak, and Kenneth E. Goodson. Phonon conduction in silicon nanobeam labyrinths. *Scientific Reports*, 7(1), jul 2017.
- [155] Jean-Savin Heron, Chandan Bera, Thierry Fournier, Natalio Mingo, and Olivier Bourgeois. Blocking phonons via nanoscale geometrical design. *Physical Review B*, 82(15), oct 2010.
- [156] Akram I. Boukai, Yuri Bunimovich, Jamil Tahir-Kheli, Jen-Kan Yu, William A. Goddard III, and James R. Heath. Silicon nanowires as efficient thermoelectric materials. *Nature*, 451(7175):168–171, jan 2008.

- [157] Amy M. Marconnet, Takashi Kodama, Mehdi Asheghi, and Kenneth E. Goodson. Phonon conduction in periodically porous silicon nanobridges. *Nanoscale and Microscale Thermophysical Engineering*, 16(4):199–219, dec 2012.
- [158] Renkun Chen, Allon I. Hochbaum, Pdraig Murphy, Joel Moore, Peidong Yang, and Arun Majumdar. Thermal conductance of thin silicon nanowires. *Physical Review Letters*, 101(10), sep 2008.
- [159] A. Ward and D. A. Broido. Intrinsic phonon relaxation times from first-principles studies of the thermal conductivities of si and ge. *Physical Review B*, 81(8), feb 2010.
- [160] Giuseppe Romano, Keivan Esfarjani, David A. Strubbe, David Broido, and Alexie M. Kolpak. Temperature-dependent thermal conductivity in silicon nanostructured materials studied by the boltzmann transport equation. *Physical Review B*, 93(3), jan 2016.
- [161] Zhiting Tian, Keivan Esfarjani, Junichiro Shiomi, Asegun S. Henry, and Gang Chen. On the importance of optical phonons to thermal conductivity in nanostructures. *Applied Physics Letters*, 99(5):053122, aug 2011.
- [162] Yongjin Lee and Gyeong S. Hwang. Force-matching-based parameterization of the stillinger-weber potential for thermal conduction in silicon. *Physical Review B*, 85(12), mar 2012.
- [163] Olivier Bourgeois, Dimitri Tainoff, Adib Tavakoli, Yanqing Liu, Christophe Blanc, Mustapha Boukhari, André Barski, and Emmanuel Hadji. Reduction of phonon mean free path: From low-temperature physics to room temperature applications in thermoelectricity. *Comptes Rendus Physique*, 17(10):1154–1160, dec 2016.
- [164] Onuttom Narayan and Sriram Ramaswamy. Anomalous heat conduction in one-dimensional momentum-conserving systems. *Physical Review Letters*, 89(20), oct 2002.
- [165] Nuo Yang, Gang Zhang, and Baowen Li. Violation of fourier’s law and anomalous heat diffusion in silicon nanowires. *Nano Today*, 5(2):85–90, apr 2010.
- [166] A. Tokmakoff, M. D. Fayer, and Dana D. Dlott. Chemical reaction initiation and hot-spot formation in shocked energetic molecular materials. *The Journal of Physical Chemistry*, 97(9):1901–1913, mar 1993.
- [167] Igor V. Schweigert. Ab initio molecular dynamics of high-temperature unimolecular dissociation of gas-phase RDX and its dissociation products. *The Journal of Physical Chemistry A*, 119(12):2747–2759, mar 2015.
- [168] Grant D. Smith and Rishikesh K. Bharadwaj. Quantum chemistry based force field for simulations of HMX. *The Journal of Physical Chemistry B*, 103(18):3570–3575, may 1999.

- [169] Bertram Terence Martin Willis and Arthur William Pryor. *Thermal vibrations in crystallography*, volume 1. Cambridge University Press Cambridge, 1975.
- [170] P.G. Klemens. Thermal conductivity and lattice vibrational modes. In *Solid State Physics*, pages 1–98. Elsevier, 1958.
- [171] Sergei Izvekov, Peter W. Chung, and Betsy M. Rice. Non-equilibrium molecular dynamics simulation study of heat transport in hexahydro-1, 3, 5-trinitro-triazine (RDX). *International Journal of Heat and Mass Transfer*, 54(25-26):5623–5632, dec 2011.
- [172] Alan J. H. McGaughey and Jason M. Larkin. PREDICTING PHONON PROPERTIES FROM EQUILIBRIUM MOLECULAR DYNAMICS SIMULATIONS. *Annual Review of Heat Transfer*, 17(N/A):49–87, 2014.
- [173] Steve Plimpton. Fast parallel algorithms for short-range molecular dynamics. *Journal of Computational Physics*, 117(1):1–19, mar 1995.
- [174] James E. Patterson, Zbigniew A. Dreger, Maosheng Miao, and Yogendra M. Gupta. Shock wave induced decomposition of RDX: Time-resolved spectroscopy. *The Journal of Physical Chemistry A*, 112(32):7374–7382, aug 2008.
- [175] Donna M. Hanson-Parr and Timothy P. Parr. Thermal properties measurements of solid rocket propellant oxidizers and binder materials as a function of temperature. *Journal of Energetic Materials*, 17(1):1–48, mar 1999.
- [176] Jason M. Larkin and Alan J. H. McGaughey. Predicting alloy vibrational mode properties using lattice dynamics calculations, molecular dynamics simulations, and the virtual crystal approximation. *Journal of Applied Physics*, 114(2):023507, jul 2013.
- [177] D. Ding, X. Chen, and A. J. Minnich. Radial quasiballistic transport in time-domain thermoreflectance studied using monte carlo simulations. *Applied Physics Letters*, 104(14):143104, apr 2014.
- [178] Vadim L’vovich Gurevich. Transport in phonon systems. 1986.
- [179] Philip B. Allen and Joseph L. Feldman. Thermal conductivity of disordered harmonic solids. *Physical Review B*, 48(17):12581–12588, nov 1993.
- [180] Philip B. Allen, Joseph L. Feldman, Jaroslav Fabian, and Frederick Wooten. Diffusons, locons and propagons: Character of atomic vibrations in amorphous si. *Philosophical Magazine B*, 79(11-12):1715–1731, nov 1999.
- [181] Joseph L. Feldman, Mark D. Kluge, Philip B. Allen, and Frederick Wooten. Thermal conductivity and localization in glasses: Numerical study of a model of amorphous silicon. *Physical Review B*, 48(17):12589–12602, nov 1993.

- [182] Hamid Reza Seyf and Asegun Henry. A method for distinguishing between propagons, diffusions, and locons. *Journal of Applied Physics*, 120(2):025101, jul 2016.